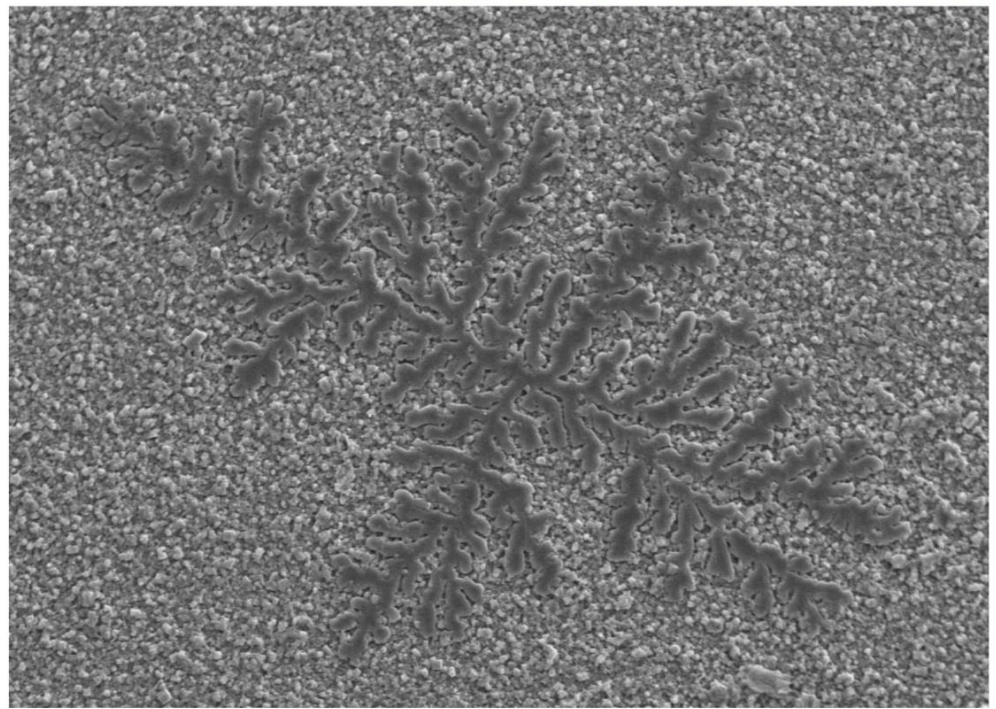


Processing and properties of advanced ceramics

workshop



Book of extended abstracts

November 23-25, 2016
Ružin, Slovak Republic

ISBN 978-80-971648-5-0

ORGANIZING INSTITUTION



Slovak Academy of Sciences



Slovak Silicate Scientific-Technological Society



Institute of Inorganic Chemistry SAS

SCIENTIFIC BOARD

prof. Pavol Šajgalík, RNDr., DrSc.
prof. Ján Dusza, RNDr., DrSc.
prof. Dušan Galusek, DrSc.
doc. RNDr. František Lofaj, DrSc.
prof. RNDr. Karel Maca, Dr.

ORGANIZING COMMITTEE

doc. Miroslav Hnatko, PhD.
Ing. Jaroslav Sedláček, PhD.
Anna Jurová - SSiVTS

Košická Belá - Ružín, November 23-25, 2016

PREFACE

Advanced ceramics are the class of materials which steadily occupy a larger portion of industrial applications. The reason for this positive development is that advanced ceramics have found applications which are not only mechanical. Newly developed advanced ceramic materials move from pure engineering applications requiring “only” the mechanical performance of the material to more sophisticated applications, where the mechanical performance is combined with some other functionality.

The orientation of research to nano-composites, ultrahigh temperature ceramics and multifunctional materials was supported not only by the interest from academia, but also by demands from industry and showed that multifunctional ceramic materials have the potential to be applied in industry, mainly in the automotive and engineering sectors. Applications as extremely low friction ceramics for high pressure pumps for engines and wind turbine ball bearings, ceramic substrates for high power devices, ceramic implants, etc. are examples of ceramic devices which make new technologies possible. The achievements of the science of ceramics are remarkable and as it was described above, they are targeted towards new technologies which in a positive sense affect everyday life.

The present workshop on Processing and Properties of Advanced Ceramics (PPAC) is a consequence of this development. 20 contributions collected in the present book of abstracts cover whole variety of research performed in Slovakia and Czech Republic with a great potential for the application. Teams dealing with the ceramics unified under the umbrella of the Slovak Silicate Society, together with the research groups from the Czech Republic regularly meet each other on PPAC workshops to interact and exchange the experiences with the newest development in this exciting research area. Three days discussion usually results in the co-ordination of the ceramic research in Slovakia, co-operation with the Czech Republic as well as in planning of new perspective projects on the national/European level.

prof. RNDr. Pavol Šajgalík, DrSc.

CONTENTS

PREFACE	2
CONTENTS	3
O. Hanzel , R. Sedlák, J. Sedláček, P. Šajgalík: Anisotropy of functional properties of SiC/GNPs and SiC/GO composites	4
V. Prajzler , D. Salamon, K. Maca: Rapid sintering of advanced oxide ceramics by conventional heating	10
Z. Kováčová , Ľ. Bača, E. Neubauer, M. Kitzmantel: Syntéza YB ₄ v tuhej fáze.	18
M. Parchovianský , I. Petříková, G. Barroso, P. Švančárek, G. Motz, D. Galusek: Oxidation behavior of stainless steel and polymer derived ceramic coatings	23
A. Prnová , K. Haladejová, R. Klement, D. Galusek: Er a Nd dopovane hlinitanové sklá	27
R. Bystrický , J. Sedláček, M. Fides, P. Šajgalík: Elektricky vodivé kompozity na báze SiC s prídavkom Ti a NbC	32
P. Švančárek , R. Klement, D. Galusek: Príprava a luminiscenčné vlastnosti Mn ²⁺ dopovanej MgAl ₂ O ₄ keramiky	38
P. Veteška , A. Prnová, D. Galusek: Sol-gel synthesis of Ce/Mn co-doped silicate phosphors and their luminescence properties	43
M. Mikula , T. Roch, D. Plašienka, M. Truchlý, M. Čaplovičová, P. Kúš: Age hardening and toughness enhancement in hard coatings	47
K. Haladejová , R. Klement, A. Prnová, D. Galusek: Nové sklené a sklo-keramické materiály na báze hlinitanov vzácnych zemín pre aplikácie v pc-WLED	52
M. Majerová , A. Prnová, M. Škrátek, A. Dvurečenskij, J. Kraxner, M. Parchovianský, A. Cigáň, J. Maňka, D. Galusek: Magnetické vlastnosti hlinitanových sklených mikrogulôčok s gelenitovou matricou	57
J. Kraxner , J. Chovanec, K. Haladejová, A. Černá, I. Petříková, D. Galusek: Hollow amorphous and polycrystalline YAG microspheres by flame spraying method	64
M. Truchlý , T. Plecenik, M. Gregor, M. Zahoran, G. Plesch, S.A.M. Tofail, A. Plecenik: Electrically modified surfaces of hydroxyapatite at microscale	69
S. Mikušínc , D. Galusková, A. Nowicka, D. Galusek: Korózia a nízokoteplotná degradácia dentálnej keramiky na báze ZrO ₂	72
M. Janek , T. Zacher, V. Hronský, M. Naftaly, M. Čaplovičová, K. Emmerich: Delaminácia kaolinitu a jeho transformácia na hallioyzyt v prostredí iónovej kvapaliny	76
P. Balážová , M. Čierniková, A. Plško, P. Exnar, J. Pagáčová, I. Papučová: The dependence of the properties of SiO ₂ sols and xerogels on the composition	83
M. Čierniková , P. Balážová, A. Plško, P. Exnar, J. Pagáčová, I. Papučová: The effect of the composition of inorganic-organic sols on the properties of the inorganic-organic layers.....	86
Ľ. Bača , Z. Hajdúchová: Sol-gel foams stabilized by silica particles	89
R. Klement , K. Haladejová, A. Prnová, D. Galusek: Mn ²⁺ /Mn ⁴⁺ doped rare-earth aluminate glass and glass-ceramics materials: the effect of charge compensation on luminescence properties	93
Z. Lenčes , A. Czímerová, M. Vyležíková, P. Šajgalík, Z. Jonšta: Influence of Eu and Ce additives on the luminescent properties of MgSiN ₂	98
AUTHOR INDEX	103

Anizotropia funkčných vlastností SiC/GNPs a SiC/GO kompozitov

Anisotropy of functional properties of SiC/GNPs and SiC/GO composites

O. Hanzel¹, R. Sedlák², J. Sedláček¹, P. Šajgalík¹

1 Institute of Inorganic Chemistry, Slovak Academy of Sciences, Dúbravská cesta 9, 845 36 Bratislava, Slovakia

2 Institute of Materials Research, Slovak Academy of Sciences, Watsonova 47, 040 01 Košice, Slovakia

ABSTRACT

Dense silicon carbide/graphene nanoplatelets (GNPs) and silicon carbide/graphene oxide (GO) with yttrium oxide and aluminium oxide as a sintering additives were prepared by rapid hot pressing (RHP). The electrical conductivity and thermal diffusivity were measured in direction parallel and perpendicular to pressing axis. Electrical conductivity of SiC/GNPs and SiC/GO increased significantly, especially with addition of GO up to 1775 S/m (for 5 wt. % of GO). Significant anisotropy of electrical conductivity of SiC/GNP and SiC/GO composites was observed due to the preferential orientation of graphene during RHP. Anisotropy of thermal diffusivity was observed in case of composites SiC/GNPs; degree of anisotropy increased with increasing amount of GNPs. On the other hand SiC/GO composites exhibit with increasing amount of GO very similar values of thermal diffusivity in both direction.

Keywords: Graphene nanoplatelets, graphene oxide, silicon carbide, composites, functional properties anisotropy

INTRODUCTION

Tailoring of electrical and thermal conductivity of structural ceramics is important for many applications, for example, static charge dissipation devices, manufacturing components by electro-discharge machining, heat exchangers and electronic substrates. From this point of view incorporation of graphene into ceramic matrix is very promising due to its extraordinary electrical and thermal conductivity [1-4]. In this work we studied the influence of addition of GNPs and GO on electrical conductivity and thermal diffusivity of SiC composites prepared by RHP in direction parallel and perpendicular to pressing axis.

EXPERIMENTAL

For preparation of input powders we used either commercially available GNPs (thickness < 4 nm, Cheap Tubes Inc., USA) or we synthesized GO. For synthesis of GO we used method very similar to Marcano et al. [5]. Such prepared GO was characterized by XRD and FTIR.

SiC/GNPs composite powders with different content of graphene nanoplatelets from 1 to 5 wt. % were prepared. First, appropriate amount of GNPs were mixed in isopropanol and ultrasonicated 100 min by strong ultrasound probe (Sonopuls HD 3200, Bandelin electronic GmbH, Germany). After that SiC (Superior Graphite, USA, β -SiC, d_{50} = 0.6 μ m), Y₂O₃ (HC Starck, purity > 99,99 %) and Al₂O₃ (Taimei Chemicals Ltd., α - Al₂O₃, purity > 99,99 %, particle size 100 nm) in proportions of 93:5:2 wt. % were added into suspension and ball milled with SiC balls for 24 h. Isopropanol was removed from suspension by vacuum rotary evaporator. Resulting composite powders were dried at 80°C over night and then sieved through 71 μ m microscreen.

SiC/GO composite powders with different content of graphene oxide from 1 to 5 wt. % were prepared. First, appropriate amount of GO were mixed in distilled water and ultrasonicated

100 minutes by strong ultrasound probe. After that SiC, Y₂O₃ and Al₂O₃ in proportions of 93:5:2 wt. % were added into suspension and ball milled with SiC balls for 24 h. Suspension was then sprayed into the liquid nitrogen and subsequently frozen powder was placed in freeze dryer in order to remove water by sublimation. Resulting composite powders were dried at 80°C over night and then sieved through a 71 µm microscreen.

In case of reference powder SiC:Y₂O₃:Al₂O₃ (93:5:2 wt. %) without any addition of graphene, all components were ball milled together in isopropanol with SiC balls for 24 h. Isopropanol was removed from suspension by vacuum rotary evaporator. Resulting reference powder were dried at 80°C over night and then sieved through 71 µm microscreen.

Composite and reference powders were placed in graphite die and surrounded by graphite paper (foil) in order to prevent direct contact between powder compact and graphite die and sintered in rapid hot press (DSP 507, Dr. Fritsch GmbH., Germany) at 1800°C with holding time of 5 min, uniaxial pressure 50 MPa under vacuum atmosphere and with heating rate 100°C/min. In detail sintering regime is described below (Fig. 1). Final dimensions of prepared samples were 20 mm in diameter and thickness approximately 3-4 mm.

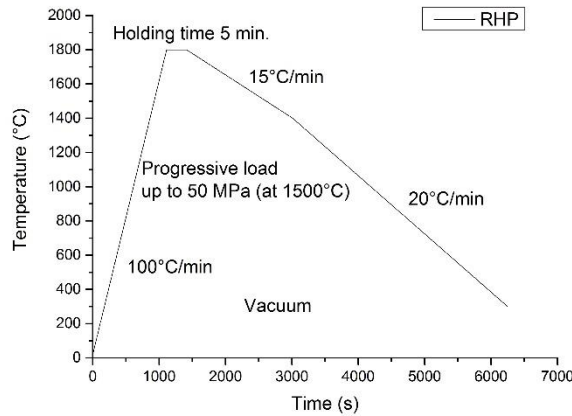


Fig. 1: Schema of sintering regime for rapid hot pressing

Densities of prepared composites were measured by Archimedes method using mercury as the immersion medium. GNPs and GO were analyzed using X-ray diffraction (Panalytical Empyrean CuK diffractometer). The infrared spectra were obtained on a Nicolet 6700 Fourier Transform Infrared spectrometer (Thermo Scientific).

Thermal diffusivity measurements were done using Laser flash analyser Linseis LFA 1000 in direction parallel and perpendicular to pressing axis. To evaluate thermal diffusivity sample 10 x 10 mm and thickness approximately 2 - 3 mm were cut and plane parallel grinded. Data were averaged for each measuring temperature over at least three measurements.

Electrical conductivity was measured by four point probe method in direction parallel and perpendicular to pressing axis.

RESULTS

After oxidation of GNPs in mixture of concentrated acids and strong oxidizing agent [5], GO has hydrophilic nature and moreover it is far more easier to exfoliate GO in comparison to graphite or GNPs, because van der Waals forces between graphene layers in GO are weaker than in GNPs due to the different distance between graphene layers. It is important to check whether the graphene nanoplatelets have been fully oxidized after above mentioned treatment. For this purpose, X-ray diffraction (XRD) is very useful. XRD spectra of graphite and graphene nanoplatelets exhibit strong sharp peak at $2\theta = 26.5^\circ$, indicating highly order structure. After oxidation this peak disappears while a new one arise at $2\theta = 11.5^\circ$ (Fig. 2).

Distance between graphene sheets in natural graphite and also in graphene nanoplatelets is 0.34 nm, but in case of graphene oxide distance between graphene sheets is 0.77 nm. These results indicate that interplanar distance increase during the oxidation of GNPs to GO due to the introducing a large number of functional groups. This was confirmed by FTIR-ATR spectra (Fig. 3).

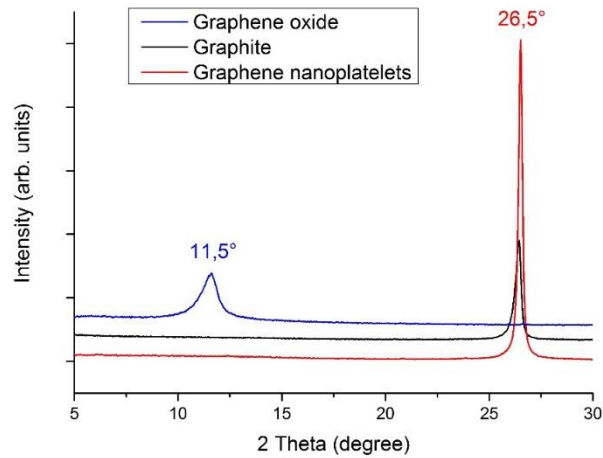


Fig. 2: XRD spectra of graphite, graphene nanoplatelets and graphene oxide

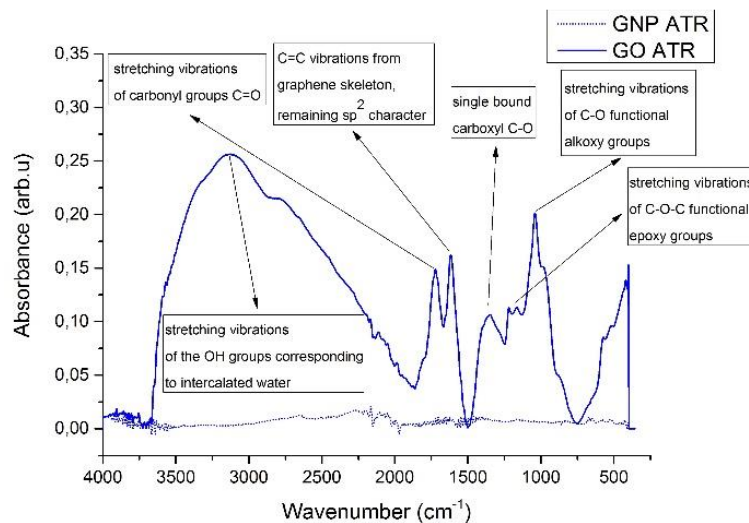


Fig. 3. FTIR-ATR spectra GNPs and GO

The relative densities of SiC/GNPs and SiC/GO composites and also reference samples are given in Tab. 1. Theoretical densities of composites with GO is difficult to calculate, for that reason the values of theoretical densities were only estimated. All prepared materials were fully dense, relative densities were higher than 99 %, except sample with 5 wt. % of graphene nanoplatelets which has slightly lower relative density (98.85 %).

Tab. 1: Relative densities of prepared composites

Sample	Content of GNPs or GO (wt. %)	Theoretical density (g.cm ⁻³)	Relative density (%)
SiC ref. RHP	0	3.24	99.54
SiC-GNP	1	3.23	99.18
SiC-3GNP	3	3.20	99.21
SiC-5GNP	5	3.17	98.85
SiC-GO	1	3.23	100
SiC-3GO	3	3.20	99.62
SiC-5GO	5	3.17	100

Room temperature electrical conductivity of SiC-GNPs and SiC-GO composites with different content of GNPs (GO) measured in direction perpendicular and parallel to RHP pressing axis is given in Fig. 4. Electrical conductivity increases with increasing amount of GNPs namely in perpendicular direction reaching maximum of electrical conductivity 700 S/m (for material with 5 wt. %). Electrical conductivity of samples in direction perpendicular to RHP pressing axis is higher than in parallel direction probably due to the preferential orientation of graphene nanoplatelets during sintering. In case of SiC-GO composites electrical conductivity increase significantly in both directions. This fact also confirmed that GO was thermally converted (reduced) to graphene layers during sintering because GO is insulator [6]. If we compare SiC-GNP and SiC-GO we can see that material with 1 wt. % GO has higher electrical conductivity than sample with 5 wt. % of GNPs. Addition of GO into the SiC matrix seems to be more effective in improvement of electrical conductivity of composites probably due to the better delamination during preparation process as a consequence of higher interplanar distance between graphene layers in GO.

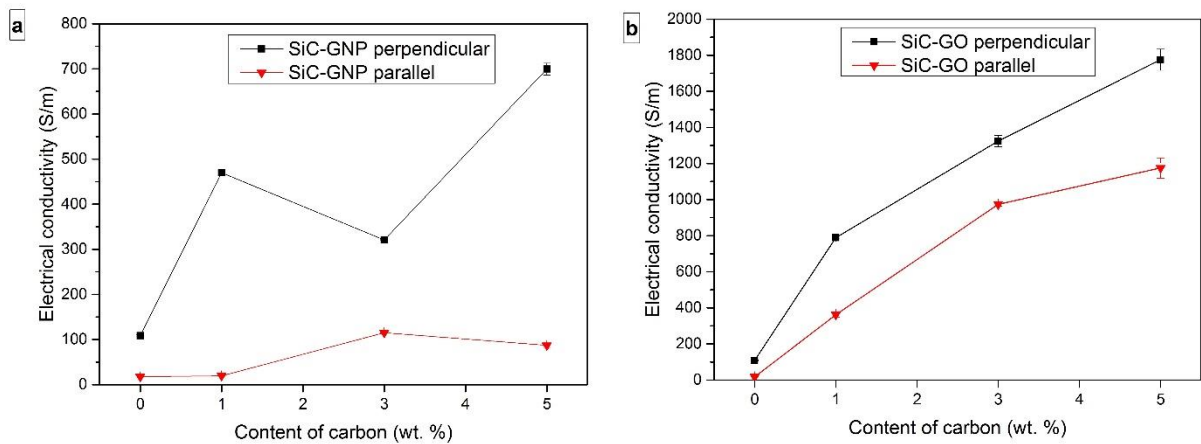


Fig. 4: Electrical conductivity of (a) SiC-GNP and (b) SiC-GO composites in parallel and perpendicular direction to pressing axis

Thermal diffusivity of SiC-GNPs and SiC-GO composites measured by laser flash technique is given in Fig. 5. Different behaviour was observed for composites with GNPs and GO. In case of SiC composites with incorporated GNPs there is anisotropy in thermal diffusivity in direction parallel and perpendicular to RHP pressing axis. In the parallel direction thermal diffusivity decrease as a content of GNPs increase. In the perpendicular direction thermal diffusivity values of composites are higher than reference sample, except sample with 3 wt. % of GNPs. As a content of GNPs increase the anisotropy of thermal diffusivity is more obvious.

In case of SiC-GO trends in direction parallel and perpendicular to RHP pressing axis are very similar. Sample with 1 wt. % of GO has similar value of thermal diffusivity as reference sample and then with increasing content of GO thermal diffusivity decreases in both directions probably due to the fact that thermally reduced GO had a number of defects: nano-holes, nano-strips, amorphous phase of rGO, microcracks, etc. [7]. These defect could act as a places for phonon scattering and therefore decrease thermal diffusivity. As a content of GO increase anisotropy of thermal diffusivity in these composites disappear.

The anisotropy of the reference sample may be attributed to the directional growth of the SiC grains during RHP due to the application of the uniaxial mechanical pressure (50 MPa)

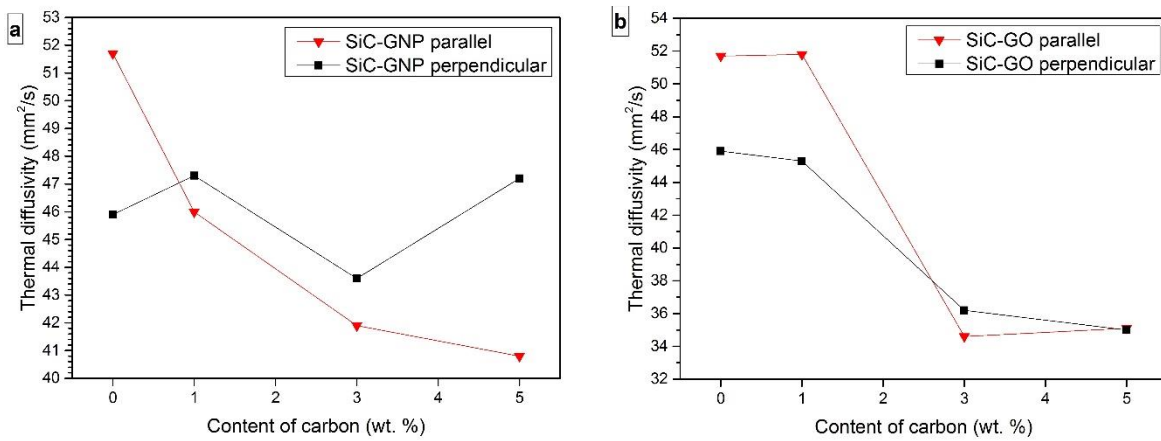


Fig. 5: Thermal diffusivity of (a) SiC-GNP and (b) SiC-GO composites in parallel and perpendicular direction to pressing axis

CONCLUSION

Graphene oxide was successfully synthesized from graphene nanoplatelets. Fully dense SiC-GNPs and SiC-GO composites with 1, 3 and 5 wt. % of GNPs (GO) were prepared by rapid hot pressing. With addition of GNPs and especially of GO electrical conductivity increases significantly. Sample with 1 wt. % of GO has higher electrical conductivity than sample with 5 wt. % of GNPs. Highest value of electrical conductivity (1775 S/m) was reached for sample which contained 5 wt. % of GO, in direction perpendicular to pressing axis. Both types of composites exhibit anisotropy in electrical conductivity due to the preferential orientation of graphene during sintering. Anisotropy of thermal diffusivity was observed only in composites SiC-GNPs with highest amount of GNPs. Contrary to this SiC-GO composites exhibit no anisotropy in thermal diffusivity with addition of 5 wt. % of GO.

ACKNOWLEDGMENT

This work was supported by the Slovak Grant Agency VEGA Project No. 2/0065/14 and APVV-0108-12. This publication is the result of the project implementation: „High-current plasma generator based on composite materials“, ITMS code 26240220054, supported by the Research & Development Operational Programme funded by the ERDF.

REFERENCES

- [1] Prasher, R. Graphene spreads the heat. *Materials Science*, vol. 328 (2010) p.185-186.
- [2] Balandin, A. A. Thermal properties of graphene and nanostructured carbon materials. *Nature materials*, vol. 10 (2011) p.569-581.
- [3] Ghosh, S., Calizo, I., Teweldebrhan, D., Pokatilov, E. P., Nika, D. L., Balandin, A. A., Bao, W., Miao, F., Lau, C.N. Extremely high thermal conductivity of graphene: Prospects for thermal management applications in nanoelectronic circuits. *Applied Physics Letters*, vol. 92 (2008) p.151911-1-3.
- [4] Chen, J., Jang, C., Xiao, S., Ishigami, M., Fuhre, M. S. Electronic properties and devices: intrinsic and extrinsic performance limits of graphene devices on SiO₂. *Nature Nanotechnology*, vol. 3 (2008), p. 206–209.
- [5] Marcano, D. C., Kosynkin, D. V., Berlin, J. B., Sinitskii, A., Sun, Z., Slesarev, A., Alemany, L. B., Lu, W., Tour, J. M. Improved synthesis of Graphene oxide. *ACS Nano*, vol. 4 (2010) p.4806-4814.

- [6] Mkhoyan, K.A., Contryman, A.W., Silcox, J., Stewart, D.A., Eda, G., Mattevi, C., Miller, S., Chhowalla, M. Atomic and electronic structure of graphene-oxide. *Nano Letters* vol. 9 (2009) p.1058–63.
- [7] Xia H, Zhang X, Shi Z, Zhao Ch, Li Y, Wang J, Qiao G. Mechanical and thermal properties of reduced graphene oxide reinforced aluminum nitride ceramic composites. *Materials Science and Engineering A* 2015;639:29-36.

Rychlé slinování pokročilé oxidové keramiky konvenčním ohřevem

Rapid sintering of advanced oxide ceramics by conventional heating

V. Prajzler^{1,2}, D. Salamon^{1,2}, K. Maca^{1,2}

¹ CEITEC VUT, Vysoké učení technické v Brně, Purkyňova 123, 602 00 Brno

² Fakulta strojního inženýrství, Vysoké učení technické v Brně, Technická 2, 616 69 Brno

ABSTRACT

The paper is dealing with fast sintering of advanced ceramic materials, namely tetragonal zirconia (particle size 80 and 140 nm) and α -alumina (particle size 150 and 270 nm), in conventional resistance furnace. This approach is made possible by special superkanthal furnace, which is capable of reaching a heating rate of 200 °C/min. Samples obtained through cold isostatic pressing (CIP) and fast sintering reached relative density up to 97.8 % t.d. for zirconia and 99.9 % t.d. for alumina, without forming any cracks in samples. Surprisingly, final relative density in the case of tetragonal zirconia with 80 nm particle size was higher for samples with larger pores in the green body (CIP at 25 MPa) than for samples with smaller ones (CIP at 300 MPa). This behaviour is different from conventional sintering and leads to considerations of heat transfer mainly by radiation.

Keywords: fast sintering, tetragonal ZrO₂, Al₂O₃, core-shell structure

ÚVOD

Pokročilé keramické materiály na bázi oxidových keramik (ZrO₂, Al₂O₃, TiO₂,...) jsou pro své vlastnosti, jako jsou vysoký bod tání, chemická stabilita, vysoká tvrdost a pevnost v tlaku, často využívány v oblasti tzv. špičkových technologií. Výsledné vlastnosti keramického tělesa jsou dány fyzikálními a chemickými vlastnostmi keramického prášku, ale také použitou technologií výroby. Ta se zpravidla skládá z následujících kroků: tvarování keramického polotovaru, odstranění pojiv, slinování, opracování slinutého keramického tělesa (broušení, leštění).

V praxi se používá velké množství různých slinovacích metod, které pracují s různými teplotními profily slinování. Nejčastěji slinování probíhá za zvýšené teploty a při atmosférickém tlaku. Existují však i metody využívající kombinaci zvýšené teploty a tlaku, jako například izostatické lisování za tepla (HIP) nebo plazmou aktivované slinování (SPS). Avšak náročnost těchto metod a vysoké pořizovací náklady vedou v průmyslové praxi k upřednostňování beztlakých slinovacích metod v pecích s konvenčním ohřevem.

Typický teplotní průběh konvenčního beztlakého slinování zahrnuje konstantní rychlost ohřevu (řádově jednotky až desítky °C/min) na slinovací teplotu s následnou výdrží na slinovací teplotě. Parametry teplotního profilu (rychlost ohřevu, teplota a čas prodlevy) jsou voleny tak, aby bylo dosaženo požadovaných vlastností produktu.

Rychlé slinování využívá oproti konvenčnímu slinování velmi rychlý ohřev na slinovací teplotu (běžně v řádech stovek °C/min). Často se provádí bez výdrže na slinovací teplotě nebo s výdrží v řádu minut, přičemž slinovací teplota bývá pro daný materiál vyšší, než u konvenčního slinování. Při rychlém slinování je těleso vkládáno již do přehřáté pece, jejíž konstrukce tomu musí být uzpůsobena. V praxi se nejčastěji používají komorové pece s výsuvným dnem nebo kontinuální pece.

Cílem této práce bylo studium rychlého slinování (100 až 200 °C/min) t-ZrO₂ a α -Al₂O₃ keramických práškových materiálů a vliv slinovacího cyklu na jejich výslednou mikrostrukturu (homogenitu a hustotu vzorku). Oproti doposud používanému konvenčnímu

slinování, by mělo rychlé slinování snížit celkovou finanční a časovou náročnost výroby, při zachování nebo dokonce zlepšení strukturních a funkčních vlastností keramických výrobků.

EXPERIMENTÁLNÍ ČÁST

2.1 POUŽITÉ KERAMICKÉ PRÁŠKOVÉ MATERIÁLY

Při experimentech byly použity následující komerční keramické práškové materiály na bázi ZrO_2 a Al_2O_3 :

- tetragonální ZrO_2 (dopovaný 3mol% Y_2O_3), komerční označení TZ-3Y, velikost částic 80 nm, výrobce Tosoh Corp. (Japonsko),
- tetragonální ZrO_2 (dopovaný 3mol% Y_2O_3), komerční označení TZ-3YSB, velikost částic 140 nm, výrobce Tosoh Corp. (Japonsko),
- $\alpha-Al_2O_3$, čistota 99,99 %, komerční označení TM-DAR (Taimicron), velikost částic 150 nm, výrobce Taimei Chemicals Co. (Japonsko),
- $\alpha-Al_2O_3$, čistota 99,99 %, komerční označení AKP-30, velikost částic 270 nm, výrobce Sumitomo Chemical Co. (Japonsko).

Velikost částic je udávána výrobcem.

2.2 PŘÍPRAVA KERAMICKÝCH POLOTOVARŮ

Keramické polotovary (tzv. green bodies) byly z uvedených keramických prášků vyrobeny pomocí izostatického lisování za studena (CIP) tlaky 25 MPa, 50 MPa, 100 MPa, 200 MPa a 300 MPa (Autoclave Engineering Inc., USA). Hmotnost vzorků byla cca 4,5 g.

Pro odstranění nečistot a nežádoucích organických chemických látek z předchozích procesů výroby byly vzorky vyžehány v peci při teplotě 600 °C s prodlevou 1 hod a rychlostí ohřevu 2 °C/min.

2.3 RYCHLÉ SLINOVÁNÍ

Pec pro rychlé slinování pokročilých keramických materiálů se skládá z pecní komory s výsuvným dnem, na které se umísťují keramické polotovary. Samotná vysokoteplotní komora je vytápěna superkantalovými topnými elementy s maximální povrchovou teplotou 1600 °C. Teplota v peci a teplota u výsuvného dna pece (u vzorků) je snímána pomocí termočlánků PtRh30-PtRh6, tzn., že v průběhu ohřevu pece a následného slinování ji lze monitorovat a regulovat. Pro umožnění rychlosti ohřevu až 200 °C/min byla teplota v pecní komoře při všech experimentech rychlého slinování nastavena na 1560 °C. Automatické zasouvání výsuvného dna do pece bylo zastaveno, když teplota u vzorků dosáhla 1500 °C. Při každém experimentu byly na výsuvné dno pece umístěny kousky Al_2O_3 vaty. Tím byly vzorky izolovány od pecního dna a zároveň byl umožněn rovnoměrnější přenos tepla, resp. bylo zabráněno ochlazování vzorku od výsuvného dna.

Pro slinování připravených keramických vzorků byly použity teplotní profily uvedené v Tab. 1, rychlost ohřevu 10°C/min byla použita z důvodu srovnání konvenčního slinování s rychlým slinováním.

Tab. 1: Přehled provedených slinovacích cyklů.

Metoda slinování	Keramický prášek	Rychlost ohřevu [°C/min]	Slinovací teplota [°C]	Výdrž [min]	Rychlost ochlazování [°C/min]
Konvenční slinování	Všechny	10	1500	1	100
Rychlé slinování	Všechny	100	1500	1	100
Rychlé slinování	TM-DAR, AKP-30	200	1500	1	100

Pozn.: Uvedené teplotní slinovací cykly byly aplikovány od teploty 700 °C.

2.4 POUŽITÉ VYHODNOCOVACÍ METODY

U keramických polotovarů a slinutých vzorků byly měřeny relativní hustoty pomocí metody sycením kapalinou, podle normy ČSN EN 623-2. Tato metoda také umožňuje zjistit procentuální podíl otevřené pórovitosti.

Mikrostruktura keramických polotovarů z keramického prášku TZ-3Y byla vyhodnocena pomocí rtuťové porozimetrie (Pascal 440, Porotec, Německo).

VÝSLEDKY A DISKUZE

3.1 VLASTNOSTI KERAMICKÝCH POLOTOVARŮ

Relativní hustoty keramických polotovarů byly závislé na velikosti tlaku aplikovaného při izostatickém lisování za studena (Tab. 2). Se zvyšujícím se tlakem byl pozorován významný nárůst relativní hustoty (ρ_{0rel}).

Výsledky získané rtuťovou porozimetrií ukazují, že s rostoucími hodnotami lisovacího tlaku se podle očekávání snižuje velikost pórů v keramickém polotovaru (Tab. 2). Distribuce velikosti pórů byla u všech vzorků unimodální, přičemž pro hodnocení velikosti pórů byly použity hodnoty maximální velikosti otevřených pórů (d_{max}) a nejčastější velikost otevřených pórů (d) [1]. Největší póry byly naměřeny u vzorků lisovaných tlakem 25 MPa.

Tab. 2: Relativní hustoty keramických polotovarů a velikost pórů u TZ-3Y vzorků.

	CIP [MPa]	ρ_{0rel} [%]	d/d_{max} [nm/nm]		CIP [MPa]	ρ_{0rel} [%]
TZ-3Y	25	37,2	92/160	TM-DAR	25	52,9
	50	40,2	74/91		50	55,1
	100	43,7	60/73		100	56,5
	200	-	-		200	57,7
	300	49,4	48/55		300	58,3
TZ-3YSB	25	41,5	-	AKP-30	25	53,5
	50	44,3	-		50	55,3
	100	46,9	-		100	57,2
	200	49,8	-		200	58,1
	300	51,3	-		300	58,8

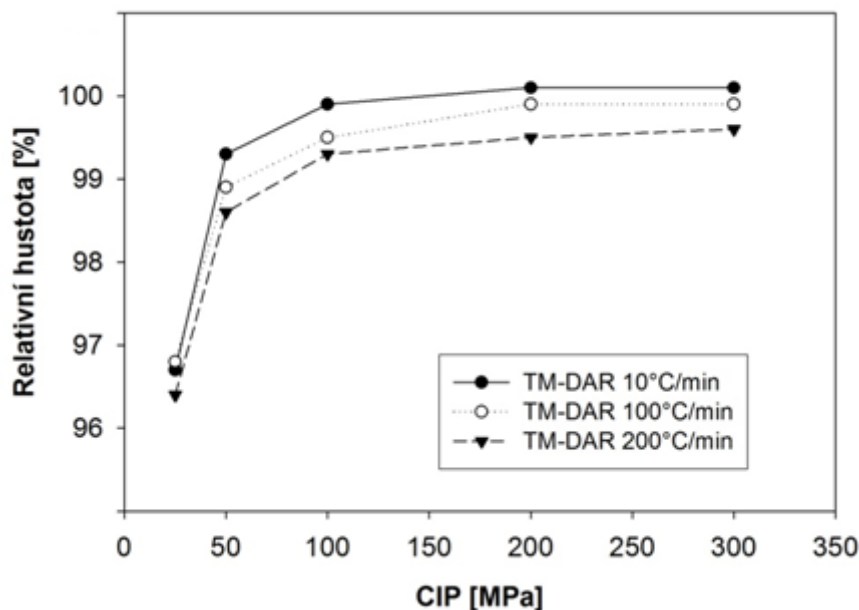
3.2 SLINOVÁNÍ TM-DAR A AKP-30

Dosažené hodnoty relativních hustot (ρ_{rel}) a otevřené pórovitosti (v_o) slinutých TM-DAR a AKP-30 vzorků jsou uvedené v Tab. 3.

Tab. 3: Relativní hustoty a otevřená pórovitost slinutých TM-DAR a AKP-30 vzorků.

	CIP [MPa]	10 °C/min, 1500 °C, 1 min		100 °C/min, 1500 °C, 1 min		200 °C/min, 1500 °C, 1 min	
		ρ_{rel} [%]	v_o [%]	ρ_{rel} [%]	v_o [%]	ρ_{rel} [%]	v_o [%]
TM-DAR	25	96,7	0,9	96,8	0,2	96,4	1,5
	50	99,3	0,1	98,9	0,2	98,6	0,2
	100	99,9	0,1	99,5	0,1	99,3	0,2
	200	100,1	0,1	99,9	0,1	99,5	0,2
	300	100,1	0,1	99,9	0,1	99,6	0,2
AKP-30	25	87,7	12,3	85,9	14,1	84,5	15,5
	50	90,0	10,0	87,8	12,2	86,7	13,3
	100	91,0	9,0	88,7	11,3	88,6	11,4
	200	91,9	8,1	90,1	10,0	89,6	10,5
	300	92,5	7,4	90,3	9,7	89,6	10,4

Při slinování AKP-30 vzorků (velikost částic 270 nm) byly dosažené relativní hustoty u konvenčního slinování vyšší než u rychlého slinování, avšak ani při ohřevu 10 °C/min nebylo dosaženo více než 93 % teoretické hustoty. To znamená, že vzorky nedosáhly stádia uzavřené pórovitosti, což potvrzují i vysoké hodnoty v_o (Tab. 3). Je tedy zřejmé, že při použití rychlého slinování tohoto materiálu s velikostí částic 270 nm by bylo pro dosažení vysokých hustot třeba použít buď delší prodlevy, nebo vyšších slinovacích teplot.



Obr. 1: Porovnání relativních hustot TM-DAR vzorků slinutých konvenčním a rychlým slinováním v závislosti na lisovacím tlaku.

V případě TM-DAR vzorků (velikost částic 150 nm) byly relativní hustoty rychle slinutých vzorků téměř shodné s hustotami konvenčně slinutých vzorků, přičemž i při rychlosti ohřevu

200 °C/min dosáhly vzorky lisované tlaky nad 100 MPa více než 99 % teoretické hustoty (Obr. 1) a to bez přítomnosti trhlin či defektů v materiálu.

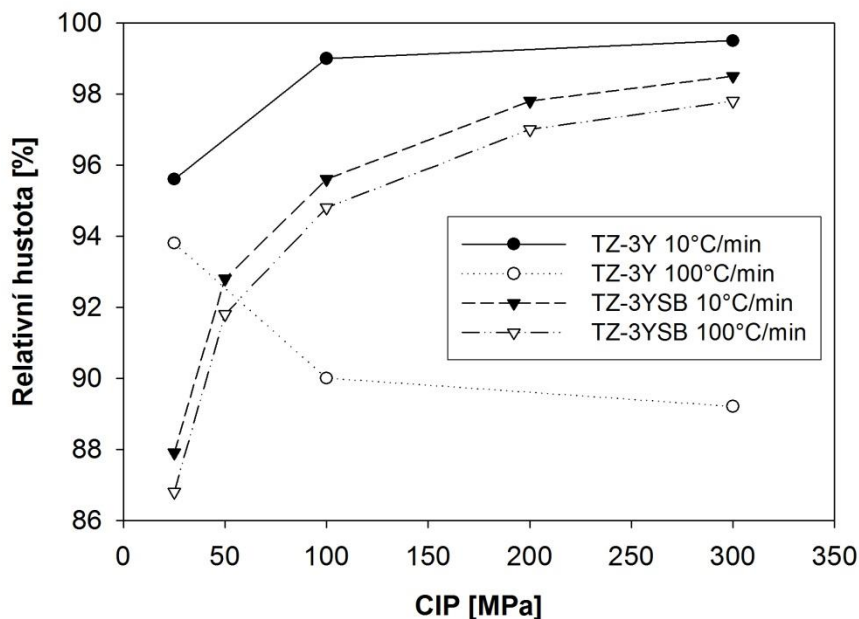
3.3 SLINOVÁNÍ TZ-3Y A TZ-3YSB

Vzorky z obou keramických prášků na bázi oxidu zirkoničitého byly po rychlém slinování bez viditelných trhlin. Obdobných výsledků s keramickým práškem TZ-3Y dosáhli Salamon a kol. [2] v případě beztlakého slinování metodou Spark Plasma Sintering. Tento výsledek je velmi zajímavý, neboť ZrO_2 se vyznačuje relativně vysokou teplotní roztažností a malou tepelnou vodivostí.

Relativní hustoty (ρ_{rel}) a hodnoty otevřené pórovitosti (v_o) slinutých TZ-3Y a TZ-3YSB vzorků jsou uvedené v Tab. 4. Grafická závislost relativních hustot na lisovacím tlaku pro jednotlivé teplotní cykly je znázorněna na Obr. 2.

Tab. 4: Relativní hustoty a otevřená pórovitost slinutých TZ-3Y a TZ-3YSB vzorků.

	10 °C/min, 1500 °C, 1 min			100 °C/min, 1500 °C, 1 min		
	CIP [MPa]	ρ_{rel} [%]	v_o [%]	CIP [MPa]	ρ_{rel} [%]	v_o [%]
TZ-3Y	25	95,6	2,7	25	93,8	3,5
	100	99,0	0,3	100	90,0	0,1
	300	99,5	0,5	300	89,2	0,1
TZ-3YSB	25	87,9	11,3	25	86,8	12,9
	50	92,8	3,1	50	91,8	5,5
	100	95,6	0,3	100	94,8	0,3
	200	97,8	0,4	200	97,0	0,3
	300	98,5	0,4	300	97,8	0,3



Obr. 2: Porovnání relativních hustot TZ-3Y a TZ-3YSB vzorků slinutých konvenčním a rychlým slinováním v závislosti na tlaku izostatického lisování.

V případě TZ-3YSB vzorků (velikost částic 140 nm) byly dosaženy relativní hustoty rychle slinutých vzorků o cca. 1 % nižší než u konvenčně slinutých vzorků. Hustota po slinutí podle očekávání rostla s rostoucím lisovacím tlakem keramického polotovaru. Nejvyšších relativních hustot tedy bylo dosaženo u vzorků lisovaných tlakem 300 MPa, a to 98,5 % u konvenčního slinování, resp. 97,8 % u rychlého slinování (Tab. 4).

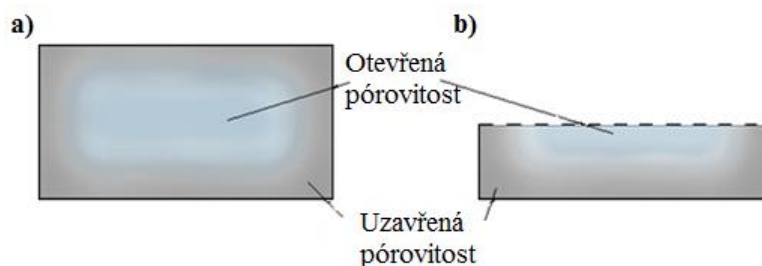
Při konvenčním slinování (rychlost ohřevu 10 °C/min) TZ-3Y vzorků (velikost částic 80 nm) bylo dosaženo vysokých relativních hustot (95,6 % a vyšších). S rostoucím lisovacím tlakem docházelo k růstu relativní hustoty, a to až na 99,5 % u vzorků lisovaných tlakem 300 MPa (Tab. 4, Obr. 2). Vzhledem k tomu, že s lisovacím tlakem klesala velikost pórů v tělese (Tab. 2) je toto chování očekávané a v souladu s dosud publikovanými poznatky [3]. Naopak neočekávané chování bylo pozorováno u vzorků slinutých rychlým slinováním. U těchto vzorků byla změřená relativní hustota menší než u konvenčního slinování, nejvyšší hodnoty (93,8 %) však dosáhl vzorek lisovaný tlakem 25 MPa, tedy vzorek s největšími póry. V případě vyššího lisovacího tlaku 100 MPa hustota klesla na 90,0 % a při lisovacím tlaku 300 MPa byla 89,2 %.

Tento jev byl vysvětlen jako důsledek radiačního mechanismu přenosu tepla při rychlém slinování [4] a počtem bodových kontaktů částic v green body [5].

3.4 CORE-SHELL STRUKTURA U TZ-3Y VZORKŮ LISOVANÝCH VYŠŠÍMI TLAKY

„Core-shell“ struktura je jev, který zaznamenali při rychlém slinování nanokrystalického ZrO₂ prášku Chen a Mayo [6]. Vlivem nízkého koeficientu teplotní vodivosti a velkého teplotního gradientu mezi povrchem a středem keramického tělesa vzniká gradient rychlosti zhutňování keramického tělesa. Povrchová vrstva materiálu se stává velmi rychle hutnou, a brání tak dalšímu smršťování tělesa. Z toho důvodu nedochází k eliminaci pórů uvnitř tělesa ani při delší výdrži v oblasti slinovacích teplot. Vzniká tzv. „core-shell“ struktura s hutnou povrchovou vrstvou a porézním středem vzorku.

Přítomnost „core-shell“ struktury u rychle slinovaných TZ-3Y vzorků (vzorky s menší velikostí částic) byla podložena velmi nízkými hodnotami otevřené pórovitosti při nízké relativní hustotě slinutého vzorku (tab. 4). Kromě vzorků lisovaných tlakem 25 MPa totiž dosažené hodnoty relativní hustoty při rychlém slinování (89 až 90 %) neodpovídaly stádiu uzavřené pórovitosti, tzn., že otevřená pórovitost nemůže být pod 1 % [7]. Nabízí se tedy vysvětlení, že vnější povrchová vrstva vzorku slinula do vysokých hustot (jak tomu odpovídá nízká hodnota otevřené pórovitosti) a vnitřek vzorku zůstal poréznější. Pro potvrzení „core-shell“ struktury byly slinuté vzorky rozříznuty (Obr. 3) a poté u nich byla opět změřena relativní hustota. V případě výskytu „core-shell“ struktury by u nich po rozříznutí měla být otevřená pórovitost. Tabulka 5 srovnává změřené relativní hustoty slinutých vzorků před a po rozříznutí.



Obr. 3: Schematické znázornění distribuce pórovitosti v případě „core-shell“ struktury u slinutých rychle slinovaných TZ-3Y vzorků: a) nerozříznutý vzorek, b) rozříznutý vzorek.

Tab. 5: Naměřené relativní hustoty (ρ_{rel}) a hodnoty otevřené pórovitosti (v_o) rychle slinutých TZ-3Y vzorků (100 °C/min, 1500 °C, výdrž 1 min) před a po rozříznutí.

Lisovací tlak	Nerozříznutý vzorek		Rozříznutý vzorek	
	ρ_{rel} [%]	v_o [%]	ρ_{rel} [%]	v_o [%]
CIP 25 MPa	93,8	3,5	94,0	3,5
CIP 100 MPa	90,0	0,1	87,1	3,7
CIP 300 MPa	89,2	0,1	85,6	6,1

Výsledky z tabulky 5 ukazují, že vzorek lisovaný tlakem 25 MPa měl otevřenou pórovitost už v případě nerozříznutého vzorku a ta zůstala zachována i po jeho rozříznutí. Vzorky lisované tlakem 100 MPa a 300 MPa v nerozříznutém stavu nevykázaly nasákavost (tzn. otevřenou pórovitost), zatímco po rozříznutí byla otevřená pórovitost v očekávané velikosti. Uvedené výsledky tedy podporují úvahy o přítomnosti „core-shell“ struktury u TZ-3Y vzorků lisovaných tlakem větším než 100 MPa. Vznik takovéto struktury byl pozorován jen u vzorků s nejmenší velikostí částic slinovaných rychlostí 100°C/min a bude dále studován analýzou mikrostruktury těles slinutých při různých rychlostech ohřevu.

ZÁVĚR

Studiem rychlého slinování (100-200 °C/min) t-ZrO₂ a α -Al₂O₃ keramik byly zjištěny následující poznatky:

- Hustota všech vzorků byla po rychlém slinování menší než hustota po konvenčním slinování. Tento fakt lze vysvětlit kratším časem stráveným v oblasti slinovacích teplot v případě rychlého slinování. S výjimkou vzorků TZ-3Y však bylo toto snížení hustot jen nepatrné.

α -Al₂O₃:

- AKP-30 vzorky nedosáhly při rychlém ani konvenčním slinování (10 °C/min) stádia uzavřené pórovitosti. Příčinou je zřejmě nízký slinovací čas, který je nedostatečný pro slinutí polotovaru složeného z částic o velikosti 270 nm.
- TM-DAR vzorky lisované tlaky 100 MPa až 300 MPa bylo možno slinout rychlostí ohřevu 100 °C/min, resp. 200 °C/min do relativních hustot nad 99 % teoretické hustoty, bez vzniku trhlin. Skutečnost, že Al₂O₃ materiál lze slinout do tak vysokých hustot během řádově dvaceti minut, má význam pro ekonomiku procesu.

Tetragonální ZrO₂ (dopované 3mol% Y₂O₃):

- Rychlé slinování TZ-3YSB vzorků vykazovalo chování analogické konvenčnímu slinování, tzn., že vykazovalo vyšší hustoty pro vzorky lisované vyššími tlaky, přičemž rychle slinuté vzorky dosáhly pouze o cca. 1 % nižší relativní hustoty než konvenčně slinuté vzorky.
- Rychlé slinování bylo z hlediska dosažených relativních hustot efektivnější pro TZ-3Y vzorky s větší pórovitostí keramického polotovaru. Tento poznatek je zcela unikátní, liší se od konvenčního slinování a vede k úvahám o přenosu tepla zejména radiací.
- Rychlým slinováním TZ-3Y vzorků lisovaných tlaky 100 MPa a 300 MPa (tzn. vzorky s větší homogenitou a menší pórovitostí) docházelo ke vzniku tzv. „core-shell“ struktury s hutně slinutým povrchem a poréznějším středem vzorku.

- Vzorčky o hmotnosti 4,5 g nevykazovaly trhliny po rychlém slinování, což je velmi pozitivní poznatek s ohledem na nízkou tepelnou vodivost a vysokou tepelnou roztažnost tohoto materiálu.

Uvedené výsledky mají význam jak při aplikacích (zkrácení celkového času vlivem zkrácení doby ohřevu), tak i pro teoretické výpočty přenosu hmoty při rychlém slinování v konvenční peci (dosud se za „rychlé“ metody slinování považovaly nekonvenční metody jako např. plazmou aktivované slinování nebo mikrovlnné slinování).

PODĚKOVÁNÍ

Tento výzkum byl finančně podpořen Ministerstvem školství, mládeže a tělovýchovy ČR v rámci projektu CEITEC 2020 (LQ1601).

LITERATURA

- [1] TRUNEC, M., MACA, K., SHEN, Z. Warm pressing of zirconia nanoparticles by the spark plasma sintering technique. *Scripta Materialia*. 2008, roč. 59, č. 1, s. 23–26. ISSN 1359-6462.
- [2] SALAMON, D., MACA, K., SHEN, Z. Rapid sintering of crack-free zirconia ceramics by pressure-less spark plasma sintering. *Scripta Materialia*. 2012, roč. 66, č. 11, s. 899-902. ISSN 1359-6462.
- [3] TRUNEC, M., MACA, K. Compaction and Pressureless Sintering of Zirconia Nanoparticles. *Journal of the American Ceramic Society*. 2007, roč. 90, č. 9. ISSN 2735-2740.
- [4] SALAMON, D., KALOUSEK, R., ZLÁMAL, J., MACA, K. Role of conduction and convection heat transfer during rapid crack-free sintering of bulk ceramic with low thermal conductivity. *Journal of the European Ceramic Society*. 2016, roč. 36, č. 12, s. 2955-2959. ISSN 0955-2219.
- [5] KALOUSEK, R. a kol. Rapid Heating of Nanoparticle-Powder Compacts by Infrared Radiative Heat Transfer. *Journal of the European Ceramic Society*, v tisku.
- [6] CHEN, D.-J., MAYO, M. J. Rapid Rate Sintering of Nanocrystalline $ZrO_2-3 \text{ mol\% } Y_2O_3$. *Journal of the American Ceramic Society*. 1996, roč. 79, č. 4, s. 906-912. ISSN 0002-7820.
- [7] SPUSTA, T., SVOBODA, J., MACA, K. Study of pore closure during pressure-less sintering of advanced oxide ceramics. *Acta Materialia*. 2016, roč. 115, s. 347-353. ISSN 1359-6454.

SYNTÉZA YB₄ V TUHEJ FÁZE

SOLID STATE SYNTHESIS OF YB₄ POWDERS

Z. Kováčová^{1,2}, L. Bača¹, E. Neubauer², M. Kitzmantel²

¹ *Institute of Inorganic Chemistry, Technology and Materials, Faculty of Chemical and Food Technology, Slovak University of Technology, Radlinského 9, 812 37 Bratislava*

² *RHP-Technology GmbH, Forschungs- und Technologiezentrum, A-2444 Seibersdorf, Austria*

ABSTRACT

Yttrium tetraboride (YB₄) powders were synthesized via four reactions including: direct synthesis from elements, reduction of yttrium oxide with boron, boron carbide reduction method and combined boron carbide/carbothermal reduction at 1500 °C, 1700 °C and 1900 °C for 2 hours in vacuum. Powders were characterized by X-ray diffraction analysis and scanning electron microscopy. Pure YB₄ was successfully synthesized using combined boron carbide/carbothermal reduction method. Secondary phases, especially Y₂O₃, YB₂ or YBO₃, were found in powders prepared using other three methods.

Keywords: YB₄, solid state synthesis, carbothermal reduction

INTRODUCTION

Borides of rare earth metals possess some unique properties, such as high melting point, high hardness and strength, excellent chemical stability and good electrical and magnetic properties. This combination of properties makes them suitable candidates for application in some extreme environments [1].

According to literature [2] an oxidation of YB₄ is assumed as a two-step process where the formation of Y₂O₃ and B₂O₃ by reaction (1) as a first step and their interaction to form YBO₃ and B₂O₃ by reaction (2) as a second step is considered.



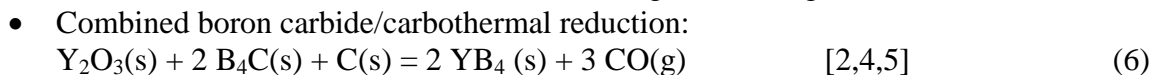
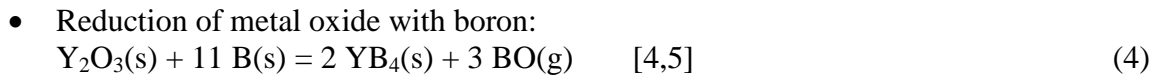
Despite of relatively low liquidus temperature (1373 °C) of oxides mixtures from reaction (2) and melting point of YBO₃ (1650 °C) it is believed that YB₄ has great application potential, especially with combination with other additives (mainly non-oxide ceramics) [3]. However, YB₄ powder is not commercially available and the synthesis method has not been widely explored. In general, several methods are available for the synthesis of borides. A common method is the direct combination of elements, which is appropriate for small-scale laboratory preparation. Other methods for synthesis of metal borides (reduction of metal oxide by boron or boron carbide, combined boron carbide/carbothermal reduction, aluminothermal method, reduction of BX₃ with a metal, etc.) can also be used [4,5]. There is very limited information on the preparation of YB₄ powders [2,3]. YB₄ ceramics has been the subject of few previous studies, mainly related to crystal structure [6] and investigation of physical and chemical properties [7,8].

The present study is focused on four different routes for solid state synthesis of YB₄ powders in vacuum. The effect of temperature on products and powder morphology was investigated.

EXPERIMENTAL

Commercially available Y (<75 μm , China Rare Metal Material), B (1-2 μm , China Rare Metal Material), Y_2O_3 (<2 μm , ABCR), B_4C (<4,8 μm , ABCR) and C (<4 μm , Imerys Graphite & Carbon) were used as starting materials.

The YB_4 powders were synthesized according to following reactions:



The stoichiometric amount of corresponding starting powder was calculated regarding to reactions (3) – (6). Powder mixtures were homogenized on rolls in cyclohexane using zirconia balls and dried in evaporator. Powder mixtures were cold-pressed into discs. Discs were positioned in graphite crucibles coated with BN. The synthesis were performed in gas pressure furnace (FCT, 8307, FPW) in vacuum at three temperatures – 1500 °C, 1700 °C and 1900 °C. After synthesis, discs were milled in agate mortar into powders and consequently analysed by XRD (Stoe Theta-Theta with $\text{CuK}\alpha$ radiation) and SEM (JEOL 6061, FEG – JEOL 7600F).

RESULTS

The XRD analysis of the powders synthesized from elements at 1500 – 1900 °C for 2h is presented in Fig. 1. The reaction of stoichiometric amount of yttrium with boron resulted in the formation of two crystalline phases identified as YB_4 and Y_2O_3 at 1500°C. With increasing temperature to 1700°C a phase composition was changed and apart of YB_4 and Y_2O_3 a new intermediate phase of yttrium diboride (YB_2) was identified. At the same time the Y_2O_3 content decreased indicating the reaction of Y_2O_3 with amorphous boron. The YB_2 phase almost disappeared at 1900°C the most probably caused by reaction with rest of boron and formation of YB_4 as product. However the yttrium oxide was still present though the intensity of Y_2O_3 peaks again decreased. Results show that the stoichiometric amount of boron seems to be insufficient for complete conversion to pure YB_4 even at 1900°C.

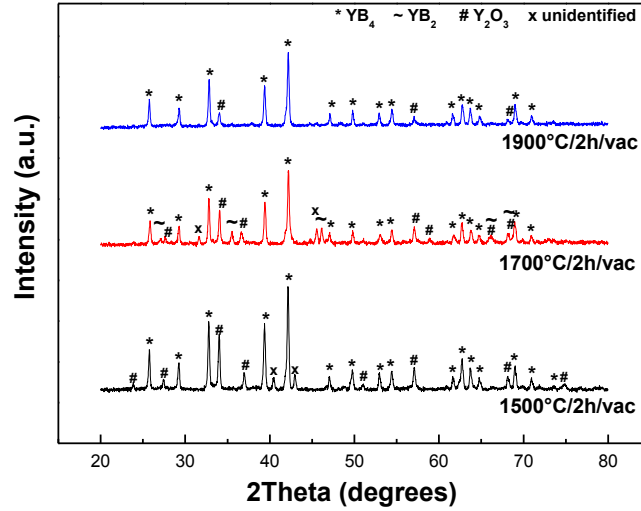


Fig. 1: XRD patterns of powders synthesized at different temperatures according to reaction (3):
 $Y(s) + 4 B(s) = YB_4(s)$

If yttrium oxide was used for preparation of YB_4 by borothermal reduction a several crystalline phases such as YB_4 , Y_2O_3 and minor phases YB_6 , YB_{12} , YBO_3 were identified at 1500 °C (Fig. 2). As the temperature increased to 1700 °C and 1900°C the predominant phase was YB_4 but a small amount of Y_2O_3 still remained.

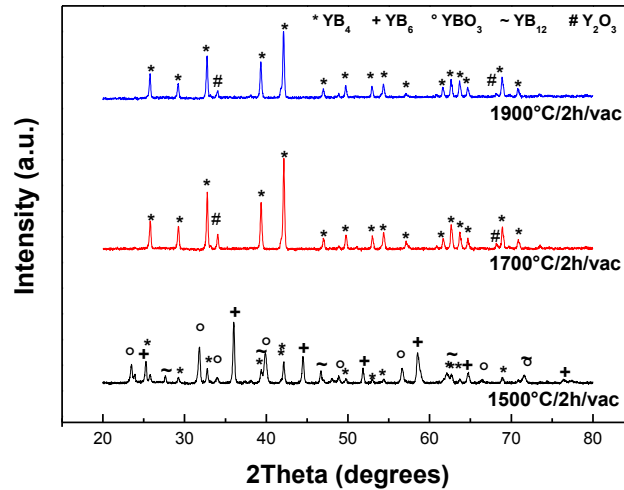


Fig. 2: XRD patterns of powders synthesized at different temperatures according to reaction (4):
 $Y_2O_3(s) + 11B(s) = 2 YB_4(s) + 3 BO(g)$

Fig. 3 shows the effect of temperature on the synthesis of YB_4 using boron carbide for reduction of yttrium oxide. XRD analysis showed that YB_4 was found as major phase in all powders. After synthesis at 1500 °C, small content of YBO_3 was found. According to previous work of Li et al. [3], YBO_3 is formed by a two-step reaction



and when the temperature further increases, the amount of YBO_3 decreases by reacting with B_4C to form YB_4 according to the following equation:



For the powders synthesized at 1700 °C and higher, nearly pure phase YB_4 was obtained with small amount of Y_2O_3 and YBO_3 .

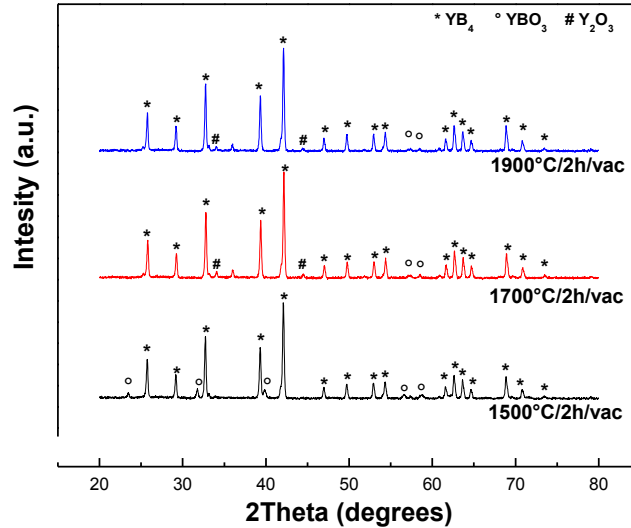


Fig. 3: XRD patterns of powders synthesized at different temperatures according to reaction (5):
 $\text{Y}_2\text{O}_3(\text{s}) + 15 \text{B}_4\text{C}(\text{s}) = 14 \text{YB}_4(\text{s}) + 2 \text{B}_2\text{O}_3(\text{g}) + 15 \text{CO}(\text{g})$

The XRD analysis patterns from the combined boron carbide/carbothermal reduction are shown in Fig. 4.

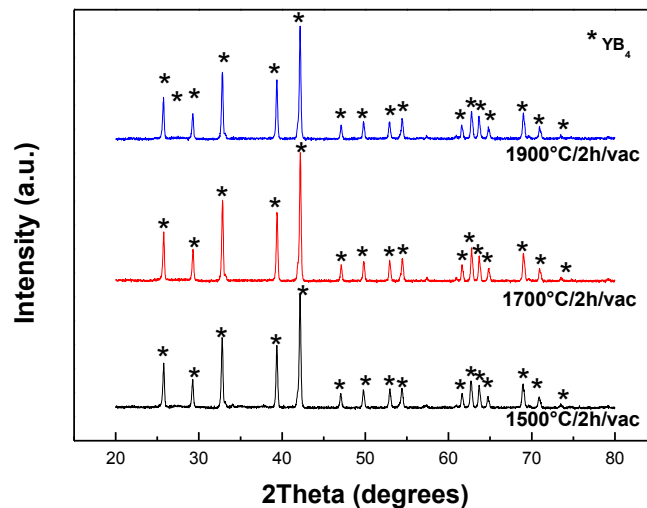


Fig. 4: XRD patterns of powders synthesized at different temperatures according to reaction (6):
 $\text{Y}_2\text{O}_3(\text{s}) + 2 \text{B}_4\text{C}(\text{s}) + \text{C}(\text{s}) = 2 \text{YB}_4(\text{s}) + 3 \text{CO}(\text{g})$

Results show that the pure YB_4 was successfully synthesized at all used temperatures. Detailed view of powders after synthesis is shown in Fig. 5. The finest grains were found in

powder synthesized at lowest temperature. Higher temperature resulted in increase of grain size, though the difference is not striking.

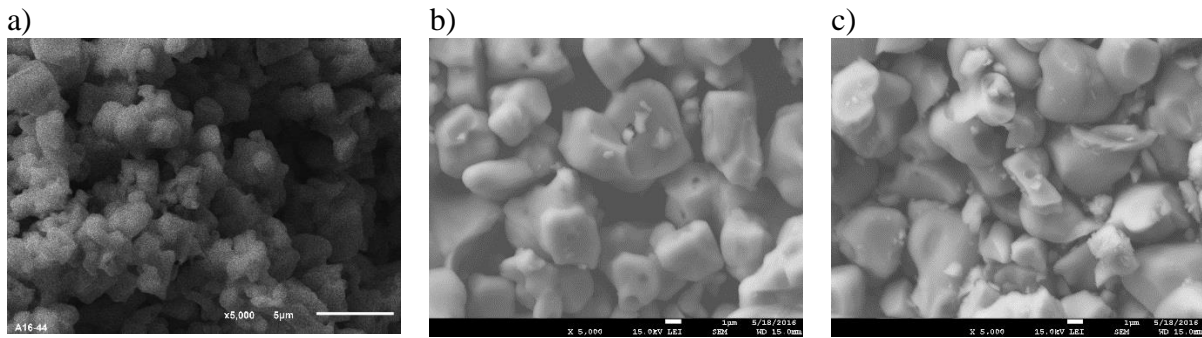


Fig. 5: SEM images of powders synthesized according to the combined boron carbide/carbothermal reduction method at: a) 1500 °C, b) 1700 °C, c) 1900 °C

CONCLUSION

The yttrium tetraboride was successfully synthesized by four different methods, however only boron carbide/carbothermal reduction synthesis led to the pure YB_4 phase without by-products. The high purity YB_4 with grain size around 1-2 microns was synthesized at 1500 °C for 2h. At higher temperatures the grain size increased and reached 7-10 microns. By the same method, however without additional reducing agent (carbon), an incomplete reduction of Y_2O_3 as a reactant and YBO_3 as intermediate phase was observed. If stoichiometric reactions of elementary yttrium or yttrium oxide with amorphous boron were used the by-products such as (Y_2O_3 , YB_2 , YBO_3 , YB_{12} , YB_6) were always present. The most appropriate method for synthesis of pure YB_4 powder was the reduction of Y_2O_3 by B_4C with the carbon. For preparation of pure YB_4 by other methods an excess of reducing agent is needed.

LITERATURE

- [1] Justin, J.F., Jankowiak, A. Synthesis and Characterization of YB_4 Ceramics, *J. Am. Ceram. Soc.*, 2011, p. 4059-4065.
- [2] Zaykoski, J. A., Opeka, M. M., Smith, L. H., Talmy, I. G. Synthesis and characterization of YB_4 Ceramics, *J. Am. Ceram. Soc.*, 2011, p. 4059-4065.5.
- [3] Li, J., Peng, A., He, Y., Yuan, H., Guo, Q., She, Q., Zhang, L. Synthesis of Pure YB_4 Powder via the Reaction of Y_2O_3 with B_4C , *J. Am. Ceram. Soc.*, 2012, p. 2127-2129.
- [4] Greenwood, N. N., Earnshaw, A. Chemistry of the Elements, Second edition, Elsevier, ISBN 0-7506-3365-4.
- [5] Matkovich, V. I. Boron and Refractory Borides, Second edition, Springer - Verlag, 1977, ISBN 978-3-642-66622-3.
- [6] Giesse, R. F., Matkovich, V. I., Economy, J. The crystal structure of YB_4 , *Zeitschrift für Kristallographie*, 1965, p. 423-432.
- [7] Fu, Y.-Y., LI, Y.-W., Huang, H.-M. Elastic and Dynamical Properties of YB_4 : First-Principles Study, *Chin. Phys. Lett.*, 2010, p. 116201-1 – 4. Second edition. A Wiley-Interscience Publication, 1976. ISBN 0-471-47860-1.
- [8] Gmelin Handbook of Inorganic and Organometallic Chemistry, 8th Edition, Springer – Verlag, ISBN 0-387-93604-1.

Oxidácia nerezovej ocele a keramických vrstvičiek pripravených z organokremičitých prekurzorov

Oxidation behavior of stainless steel and polymer derived ceramic coatings

M. Parchovianský¹, I. Petříková¹, G. Barroso², P. Švančárek¹, G. Motz², D. Galusek¹

¹*Vitrum Laugaricio – Joint Glass Center of the IIC SAS, TnU AD, and FCHFT STU, Študentská 2, 911 50 Trenčín, Slovakia*

²*University of Bayreuth, Ceramic Materials Engineering, D-95440 Bayreuth, Germany*

ABSTRACT

In this work, the development of a novel thermal barrier coating system based on polymer-derived ceramics, applied by simple lacquer methods is reported. The system consists of a polysilazane (PHPS) bond-coat and an insulating layer formed by the combination of passive yttria-stabilized zirconia (YSZ) and active ZrSi₂ fillers with glass microspheres and an (organo)silazane (Durazane 1800). The aim of this study is to investigate the oxidation resistance of a AISI441 stainless steel with and without the coating. The high temperature oxidation behaviour of these materials in a flow-through oxygen atmosphere was investigated at the temperatures of 900 °C, 1000 °C and 1100 °C. The resulting oxidized steel and coatings were investigated by SEM and EDS. Beneficial effect of the PDC coating was observed at the temperature of 900 °C, demonstrated by marked reduction of the weight gain of coated steel after 196 h of exposure to flowing oxygen. At higher temperatures the protective action of the PDC coating was not observed, and a thick layer of oxidation products was formed at the steel/coating interface.

Keywords: steel, PDC coatings, oxidation

INTRODUCTION

New technologies for high temperature applications are always in demand and are a great challenge in many fields of industry. However, high temperatures usually result in high energy consumption connected with environmental issues, short lifetime of exposed materials and therefore, there are requirements for special materials. Rather than designing new structural materials which can sustain harsh environmental conditions, the combination of conventional materials and coatings with tailored properties is usually a technologically simpler and economically more interesting approach [1]. Polymer-derived ceramics (PDCs) have been investigated in the past few decades for several applications, such as bulk materials, ceramic fibers and porous ceramics. Additionally, the PDC approach has proven to be a suitable alternative for the processing of functional coating systems with protective properties against oxidation and corrosion, high optical emissivity, and many others [2, 3]. The main advantage of PDC systems is the easy processability provided by the preceramic polymers, also known as ceramic precursors, which are either liquid or solid and, in the last case, meltable or soluble. Thus, the polymers can be deposited on substrates with the most varied geometries by simple lacquer methods like dip-, spray- or spin-coating as well as by typical ceramic shaping methods like tape-casting. The thermal treatment of PDCs has also advantages in comparison to traditional ceramic processing as it requires much lower temperatures [3, 4].

The aim of this work was the development of oxidation resistant coating system with protective action at elevated temperatures around 1000 °C. The rate of oxidation in pure flow-through oxygen atmosphere was determined, and the oxide scales formed after different exposures times and temperatures on coated and uncoated samples were characterized by

SEM/EDS and XRD, including detailed microstructural analysis of the oxide scales formed in the atmosphere of oxygen.

EXPERIMENTAL

The bond-coat was prepared from the perhydropolysilazane precursor PHPS (Merck KGaA, Germany) by dip-coating of the cleaned metal sheets (dip-coater RDC 15, Relamatic, Switzerland) with a hoisting speed of 0.3 m/min. The pyrolysis of the bond-coat was performed in air at a temperature of 500 °C for 1 h with heating and cooling rates of 5 K/min (Nabertherm® N41/H, Nabertherm, Germany). For the top-coat, yttria-stabilized zirconia (YSZ) (H. C. Starck GmbH, Germany) with $d_{90} = 0.50 \mu\text{m}$, $d_{50} = 0.3 \mu\text{m}$ was used as passive filler, while zirconium disilicide (ZrSi_2 , ball-milled to $d_{90} = 3 \mu\text{m}$, $d_{50} = 1.5 \mu\text{m}$, HMW, Germany) was used as active filler. The top-coat was prepared by mixing the ceramic filler particles YSZ (64.8 vol.%), ZrSi_2 (5.4 vol.%), and glass microspheres (3.4 vol.%) with the composition (in mol.%) $80\text{SiO}_2\text{-}10\text{Al}_2\text{O}_3\text{-}10\text{ZrO}_2$, prepared by flame synthesis, with the liquid (organo)silazane Durazane 1800 (Merck KGaA, Germany) (26.3 vol.%). The pyrolysis of the composite coatings was performed in air (Nabertherm® N41/H, Nabertherm, Germany) at 1000 °C with the heating and cooling rate of 3 K/min and a holding time of 1 h.

High temperature oxidation tests were carried out in a high temperature horizontal electric tube furnace (Clasic 0213T, Czech Republic) at the temperatures of 900 °C, 1000 °C and 1100 °C and the exposure times in the range of 1 – 96 hours in flowing oxygen (purity 99.5%, Linde, Slovakia). After each test the coated and uncoated samples were weighted and specific weight changes related to the samples' surface area were calculated in order to investigate the role of the coating during oxidation. Microstructure of oxidized samples was in detail examined by scanning electron microscopy (JEOL JSM 7600 F, Japan) equipped with EDS detector (Oxford Instruments, UK).

RESULTS

Fig. 1 a-b show the weight gain of the uncoated and coated steel, respectively, as a function of time at various temperatures. The time dependence of weight gain of uncoated steel (Fig. 1a) due to the surface oxide scale growth approximately followed the classic Wagner parabolic relationship. At 900 °C the mass gain of coated samples was about one half of the uncoated steel (Fig. 1a). It seems that the coating provides some protection at this temperature. However, at higher temperatures the mass gain of uncoated steel was lower than the weight gain measured for coated samples. SEM/EDS studies were carried out on the surface and scale cross sections to reveal any changes in the microstructure and the chemistry of steel and the coating, including the underlying substrate oxidized in oxygen at elevated temperature.

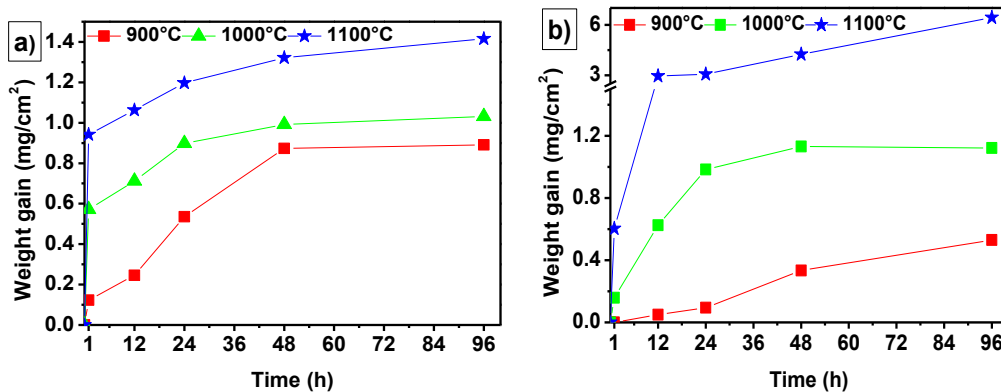


Fig. 1: Mass gain of samples a) AISI 441 steel, b) coated steel.

Fig. 2 shows the oxidized surfaces and cross-sections of uncoated steel and coated samples exposed to oxygen at different temperatures and holding times. Most of the surface of steel (Fig. 2a) was covered by a non-protective oxide layer consisting of a thin base oxide and evenly distributed crystal nodules up to 10 μm in size. While the uncoated steel was already oxidized, the coated samples (Fig. 2b) were partially protected against oxidation.

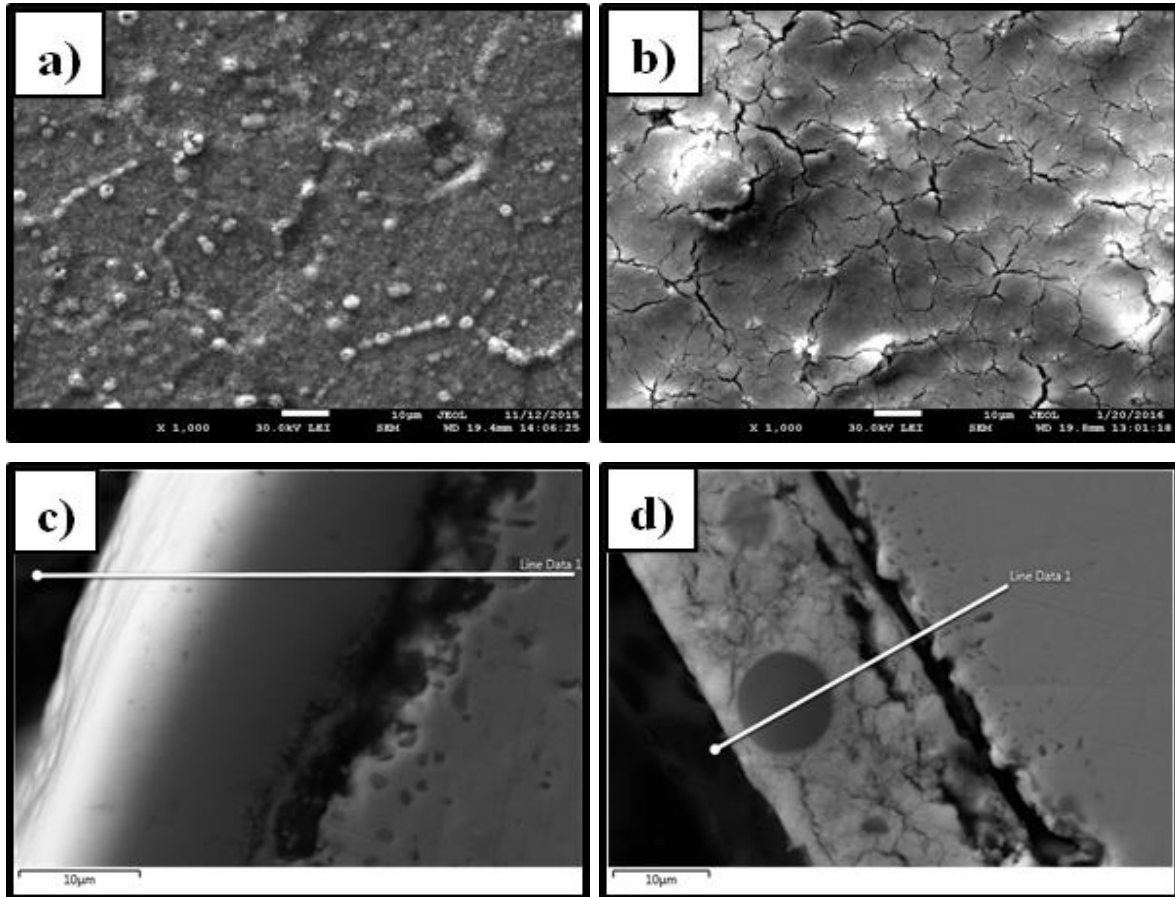


Fig. 2: Microstructures of steel and coat after oxidation tests; top view on a) steel – 900 °C/24 h, b) coated steel -1000 °C/24 h and cross-section of c) steel - 1100 °C/96 h and d) coated steel – 1000 °C/96 h.

SEM/EDS examination of the cross-section of steel (Fig. 2c, Fig. 3a) revealed that the outer oxide layer contained relatively high amounts of Cr and Mn. The presence of a Si-enriched porous layer at the substrate/chromium oxide interface is also visible. SEM cross-section analyses on PDC coated samples (Fig. 2d, Fig. 3b) revealed gaps along the oxide scale/metal interface. This may be an indication of weak adherence of the oxidized coating layer to the steel substrate. The coating predominantly consisted of ZrO_2 . The EDS analysis (Fig. 2d, Fig. 3b) also revealed the presence of Cr and Mn in the coating. As expected, the oxide scale that grew between the steel substrate and the coating were rich in Cr, with a substantial amount of Mn. This was consistent with the oxidation behavior of uncoated ferritic stainless steels, which typically form a dual layer scale consisting of a $(\text{Mn}, \text{Cr})_3\text{O}_4$ spinel-rich top layer and a chromia sublayer. It is likely that the Cr was incorporated into the coating during the early stages of oxide film formation before a fully dense, protective chromia scale could be formed. Especially at high temperature oxidation (i.e. 1000 °C and 1100 °C) the porous coating serves as a gate for oxygen diffusion to steel substrate, resulting in formation of oxide layer at coating/steel interface. Unlike uncoated steel the oxide layer at the coating/metal interface spalls off, for unknown reason. Further optimization of the coating composition is required to achieve effective corrosion protection of steel substrate.

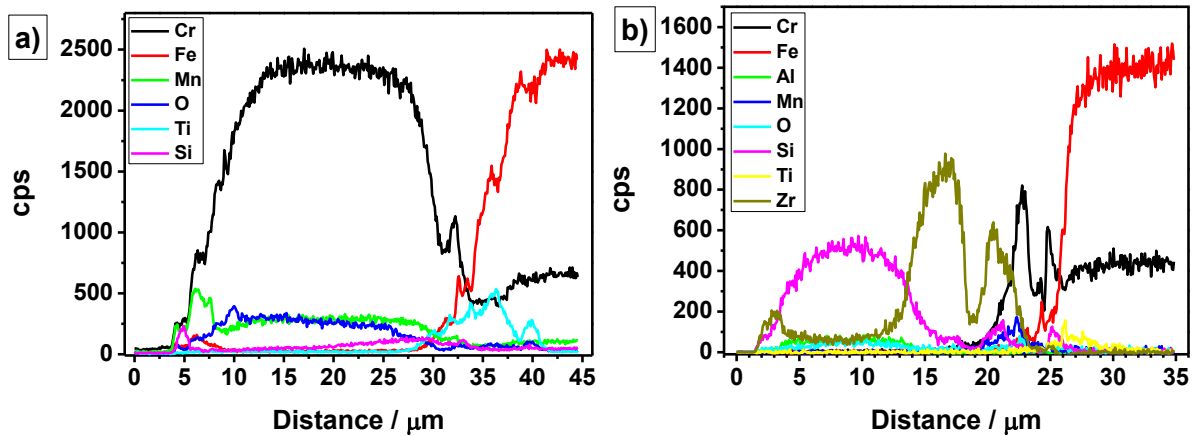


Fig. 3: EDS line scan - cross-section of the corroded surfaces, a) steel – 1100 °C/96 h, b) coated steel – 1000 °C/96 h.

CONCLUSIONS

Beneficial effect of the PDC coating with the fillers in terms of oxidation protection of the steel substrate was observed at 900 °C, with the mass gain about one half of that in uncoated steel oxidized under the same conditions, while at 1000 °C and 1100 °C no protective effect of the coating was observed. Oxidation of stainless steel substrate yielded passivation Cr_2O_3 , layer with some TiO_2 and a $(\text{Mn}, \text{Cr})_3\text{O}_4$ spinel non-protective upper layer. In coated samples monoclinic and tetragonal ZrO_2 were the dominant phases at 900 °C, while at higher temperatures formation of ZrSiO_4 was observed within the coating, with $(\text{Mn}, \text{Cr})_3\text{O}_4$ and Cr_2O_3 present at the coating/steel interface. Unlike uncoated steel, spallation of the Cr_2O_3 passivation layer was observed under the protective coating at higher temperatures.

ACKNOWLEDGMENT

Financial support of this work by the grant VEGA 2/0058/14 and APVV 0014-15, and the Alexander von Humboldt Foundation in the frame of the institutional cooperation grant scheme is gratefully acknowledged. This publication was created in the frame of the project "Centre of excellence for ceramics, glass, and silicate materials" ITMS code 262 201 20056, based on the Operational Program Research and Development funded from the European Regional Development Fund.

REFERENCES

- [1] P. Colombo, G. Mera, R. Riedel, G.D. Sorarù, Polymer-derived ceramics: 40 Years of research and innovation in advanced ceramics, *Journal of the American Ceramic Society*, 93 (2010) 1805–1837.
- [2] J.D. Torrey, R.K. Bordia, Processing of polymer-derived ceramic composite coatings on steel, *Journal of the American Ceramic Society*, 91 (2008) 41–45.
- [3] M. Günthner, A. Schütz, U. Glatzel, K. Wang, R.K. Bordia, O. Greißl, W. Krenkel, G. Motz, High performance environmental barrier coatings, Part I: Passive filler loaded SiCN system for steel, *Journal of the European Ceramic Society*, 31 (2011) 3003–3010.
- [4] M. Günthner, T. Kraus, A. Dierdorf, D. Decker, W. Krenkel, G. Motz, Advanced coatings on the basis of Si(C)N precursors for protection of steel against oxidation, *Journal of the European Ceramic Society*. 29 (2009) 2061–2068.

Er a Nd dopované hlinitanové sklá**Er and Nd doped aluminate glasses**A. Prnová¹, K. Haladejová¹, R. Klement¹, D. Galusek¹¹ *Vitrum Laugaricio – Joint Glass Center of the IIC SAS, TnU AD, and FCHPT STU, Študentská 2, SK-911 50 Trenčín, Slovak Republic***ABSTRACT**

The yttrium-aluminate glass microspheres with eutectic composition A6M (76.8 mol% Al₂O₃, 23.2 mol% Y₂O₃), doped with different concentrations of Er³⁺ and Nd³⁺ ions (1, 3, 5 mol. %) were prepared by combination of sol-gel – Pechini method and the flame synthesis. The prepared samples were studied by OM, SEM, XRD, HT XRD and DSC analysis. The isothermal crystallisation experiments at 1000°C and 1500°C with different holding times were performed and PL spectra of crystallised and raw microspheres were measured. The typical emission spectra for glassy and polycrystalline materials were obtained. The values of emission intensity, comparable to commercial used materials were measured in as-received glass samples. Slight increase of intensity of PL emission spectra in the samples doped with 1 mol.% of Er³⁺ crystallised for 20 min at 1000°C was observed.

Keywords: glass microspheres, flame synthesis, PL properties

INTRODUCTION

During the last decades, Al₂O₃-Y₂O₃-RE₂O₃ doped transparent ceramic materials have drawn attention in research for their excellent thermomechanical and optical properties in both single-crystalline and polycrystalline forms. Especially YAG (yttrium-aluminium garnet) is very hard material, crystallizes in cubic form which does not damage easily under condition of high irradiance with an electron beam. Accordingly, rare earth doped YAG materials are promising phosphor candidates in cathode ray tubes (CRTs), field emission displays (FED), scintillation vacuum fluorescent displays (VFDs) and electroluminescent (EL) materials [1]. One of the most interesting benefits of Nd-YAG materials is the possibility of high doping of these materials without degradation of their homogeneity and thermal conductivity [2]. Taira et al. [3] described preparation and examination of the 4.8 at. % Nd-doped YAG ceramic material with the efficiency corresponding to four times enhancement of the 0.9 at. % Nd:YAG single crystal microchip laser. Laser applications require homogenous and highly transparent materials and preparation of these materials is energy and time-consuming. Y₂O₃-Al₂O₃ glasses with high alumina content are interesting candidates for replacement of commercially used materials for easier and lower cost preparation and for their higher ability to host transition metal or lanthanide elements. In this work, yttrium-aluminate glass microspheres with eutectic composition A6M (76.8 mol. % Al₂O₃, 23.2 mol. % Y₂O₃), doped with different concentrations of Er³⁺ and Nd³⁺ ions (1, 3, 5 mol. %) were prepared by combination of sol-gel – Pechini method [4] and the flame synthesis. The prepared glass bodies were characterized by OM, SEM, XRD, HT XRD and DSC analysis. On the basis of the results of HT XRD and DSC experiments, the preliminary isothermal crystallization experiments were performed to obtain glass ceramic materials with controlled phase composition. Finally, the fluorescence spectra were recorded to study the optical properties of as received raw and crystallized microspheres.

EXPERIMENTAL

The glass microspheres with eutectic composition from the pseudo-binary system Al_2O_3 - $Y_3Al_5O_{12}$ and with addition of 1, 3 and 5 mol. % of Er_2O_3 and Nd_2O_3 (**Tab.1**) were prepared by combination of sol-gel (Pechini) [4] method and flame synthesis [5]. The Pechini sol-gel method was used to prepare a fine powder with sufficient homogeneity. Aluminium nitrate (99.9 %; Sigma Aldrich, Germany) was dissolved in deionized water and mixed with yttrium nitrate and erbium or neodymium nitrate solution prepared by dissolution of Y_2O_3 , Er_2O_3 or Nd_2O_3 (99.9%: Treibacher Industry, Austria) in diluted nitric acid. An aqueous solution of citric acid and ethylene glycol in the molar ratio 1:1 was then added. The mixture was refluxed at 85 °C for 2 h and then heated to 150 °C to promote polymerization, and to evaporate the solvent. Viscosity of the solution increased rapidly with time until aerated resin was formed. Finally, organic compounds were removed by calcination of the reaction product at 800 °C for six hours in ambient atmosphere. The narrow fraction obtained by sieving the prepared powder through 40 and 25 μm sieves was used as precursor powders for flame synthesis. The precursor powders were fed into methane-oxygen flame where the powder particles melted. The molten droplets were quenched with distilled water, collected and separated. Glass microspheres were dried and calcined at 650° C for 1 hour to remove any organic residua. The respective rare earth elements were added on account of yttrium to preserve the Al/(Y+RE) ratio. The morphology of prepared glass particles was studied by optical microscopy (Nicon ECLIPSE ME 600) and SEM (JEOL 7600F, accelerating voltage 20kV). The X-ray powder diffraction analysis (Panalytical Empyrean, $CuK\alpha$ radiation, 2θ range 10-80°) was used to obtain qualitative information on the phase composition of prepared samples. Thermal behaviour of prepared samples was studied by DSC analysis in the temperature range of 35-1200°C and at a scan rate of 10K/min. HT XRD experiments in temperature interval 750-1500°C and 2 theta range 25-55°, were performed to study a phase composition in prepared systems during heat treatment. On the basis of HT XRD and DSC (**Tab.2**) experimental results, the isothermal crystallization experiments at 1000 and 1500°C were performed (vertical tube furnace Classic CZ). Fluorescence spectra (Fluorolog 3-21, Horiba) were recorded to study of optical properties of non-crystallized and crystallized microspheres.

Tab.1: The composition of prepared samples

sample	Al_2O_3 mol.%	Y_2O_3 mol.%	Er_2O_3 mol.%	Nd_2O_3 mol.%
A6Er1	76,8	22,2	1	0
A6Er3	76,8	20,2	3	0
A6Er5	76,8	18,2	5	0
A6Nd1	76,8	22,2	0	1
A6Nd3	76,8	20,2	0	3
A6Nd5	76,8	18,2	0	5

Tab.2: The onset of crystallization temperature (T_x), maximum of crystallization temperature (T_p), inflex point of crystallization peak (T_f) of samples selected for crystallization experiments.

Sample	T_{x1} (°C)	T_{p1} (°C)	T_{f1} (°C)	T_{x2} (°C)	T_{p2} (°C)	T_{f2} (°C)
A6Er1	926	936	932	993	1002	1000
A6Nd1	925	935	932	996	1003	1000

RESULTS

The study of morphology of the glass microspheres by SEM revealed the presence of partially or fully crystalline particles in prepared systems. This is in good agreement with the results of X-ray powder diffraction analysis, in which the traces of YAG (Y₃Al₅O₁₂) crystalline phase were detected for some compositions.

The excitation (PLE) spectra in the interval 250-750 nm were measured for Er- and Nd-doped samples. Based on the results of these measurements, appropriate excitation wavelengths (380 nm for Er- and 360 nm for Nd-doped samples) were selected. All the measured NIR emission (PL) spectra of Nd-doped samples (Fig.1) consist of two strong characteristic bands attributed to the 4F_{3/2}→4I_{9/2} (906 nm) and 4F_{3/2}→4I_{11/2} (1064 nm) transitions, and a band with smaller intensity at 1339 nm that belongs to 4F_{3/2}→4I_{13/2} transition, respectively [6]. Emission spectra of the Er-doped samples exhibit two bands centered at 524 nm and 547 nm in VIS region and a strong band centered at 1532 nm in NIR region (Fig.1), which can be attributed to the transitions 2H_{11/2}→4I_{15/2}, 4S_{3/2}→4I_{15/2} and 4I_{13/2}→4I_{15/2} of the Er³⁺ ion [7]. From the comparison of the intensities it is evident, that both the VIS and NIR emission intensities decrease with increasing concentration of the dopant ions due to the concentration quenching [8]. For the crystallization experiments, the samples doped with 1 mol% Er and Nd with highest PL intensities were selected.

From the DSC records of selected glass samples, the onset of crystallization temperature (T_x) and maximum of crystallization temperature (T_p) were estimated (Tab.2). The inflection points of crystallization peaks (T_{f1}, T_{f2}) were determined from the first derivation of the DSC curves. Around the T_{f1} temperature, the highest rate of crystallization and sufficient nucleation rate is expected. The study of samples by HT XRD analysis show crystallisation of YAG phase in the temperature interval (750-1300°C), with the onset of crystallisation of YAG phases around 920° C. Also, the crystallisation of α-Al₂O₃ phase in the temperature interval 1300-1500°C was observed. Two temperature intervals were determined from HT-XRD measurements, where significant increase of the YAG content was observed, (930-935°C) and (990-1000°C), which correspond to the two exothermic effects identified in the DSC curve. The third temperature interval with significant increase of α-Al₂O₃ crystalline phase was observed at 1490-1500°C. On the basis of these results isothermal crystallisation experiments at the temperatures of 1000°C (YAG crystallisation as the only phase in the systems) and 1500°C (YAG and α-Al₂O₃ crystallization in systems) with 20 min, 120 min and 5 hour (to obtain fully-crystalline systems) holding times were performed.

The XRD diffraction patterns of individual samples were measured to confirm the presence of YAG and α-Al₂O₃ phase in samples. The Fig.2 shown results of X-ray analysis of individual samples crystallised at 1000°C. In all samples treated at this lower temperature, only presence of the YAG phase was observed. Fig.3 shows PL spectra of the sample A6Er1, crystallised at 1000°C. The highest emission intensity was measured in the sample crystallized for 20 minutes. The longer heat treatment (120 and 300 min) resulted in high fraction of the YAG phase (Fig.2) and had negative influence on PL properties (Stark splitting, decreasing emission intensity). Similar effect was observed in the samples heat treated at 1500°C (Fig. 4 and Fig.5). The crystallisation and presence of α-Al₂O₃ phase in samples caused deterioration of PL properties. Decreasing emission intensity of crystallised samples and Stark splitting in spectra was observed already after 20 min crystallisation. The examination of the influence of YAG and α-Al₂O₃ phase on PL properties in Nd doped samples is in process.

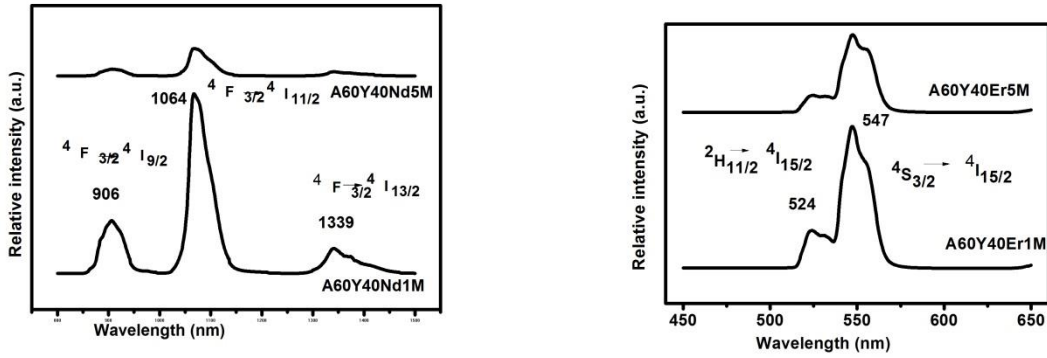


Fig. 4: Emission spectra of A6Nd1, A6Nd5, A6Er1 and A6Er5 glasses measured in the NIR region.

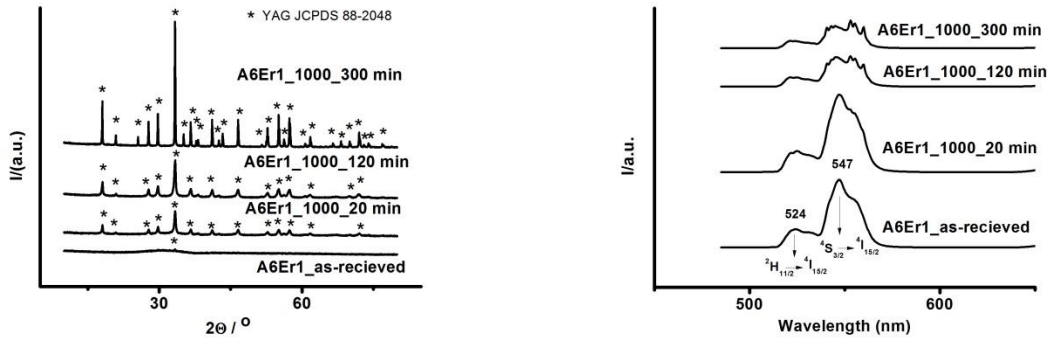


Fig.2: Comparison of XRD diffraction patterns of the as received glass A6Er1 and of the glass heat treated at 1000°C.

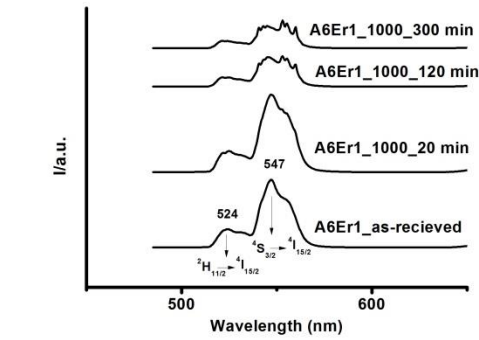


Fig.3: Comparison of emission spectra of A6Er1 sample in visible region

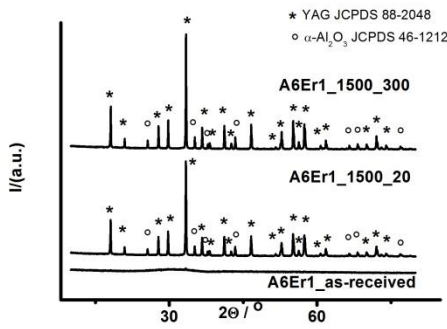


Fig.4: Comparison of XRD diffraction patterns of the as received glass A6Er1 and of the glass heat treated at 1000°C.

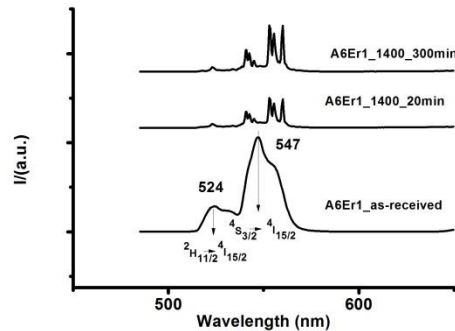


Fig.5: Comparison of emission spectra of A6Er1 sample in visible region

CONCLUSIONS

The yttrium aluminate glass microspheres doped with 1, 3, and 5 mol% Er³⁺ and Nd³⁺ were prepared by combination of sol-gel (Pechini) method and flame synthesis. The prepared systems were characterised by OM, SEM, and X-ray powder diffraction. Thermal behaviour was studied by the combination of DSC and high temperature X-ray diffraction. The crystallisation of YAG phase was observed in the temperature interval (920-1300°C) with two maxima at ≈930 and 1000°C. Crystallization of α-Al₂O₃ was observed at T ≥1300 °C with the maximum crystallization rate at 1500°C. The isothermal crystallisation experiments at

1000°C and 1500°C with 20, 120 and 300 minutes isothermal heating were also performed and the phase composition of crystallized samples determined. PL spectra of Er³⁺ doped crystallised samples were measured. Slight increase of green emission was observed in the sample crystallised at 1000°C for 20 minutes.

ACKNOWLEDGMENT

The financial support of this work by the project SAS-MOST JRP 2015/6, VEGA 1/0631/14, and VEGA 2/0058/14 is gratefully acknowledged. This publication was created in the frame of the project "Centre of excellence for ceramics, glass, and silicate materials" ITMS code 262 201 20056, based on the Operational Program Research and Development funded from the European Regional Development Fund.

REFERENCES

- [1] Y.C. Kang, S.B. Park, I.W. Lenggoro, K. Okuyama, Preparation of nano-aggregation YAG-Ce phosphor particles by spray pyrolysis, *J. Aerosol Sci.*, **29**, (1998), S911
- [2] T. Taira, A. Ikesue, K. Yoshida, W.R. Bosenberg, M.M Fejer, Diode – Pumped Nd:YAG Ceramics Lasers, *Advanced Solid-State Lasers*, **19**, Optical Society of America, (1998), 430,
- [3] Taira T., Kurimura S., Saikawa J., Ikesue A., Yoshida K., Highly trivalent neodymium ion doped YAG ceramic for microchip lasers, *Advanced Solid-State lasers*, **26**, (1999), 212
- [4] M. P. Pechini, "Method of Preparing Lead and Alkaline-Earth Titanates and Niobates and Coating Method Using the Same to Form a Capacitor," U.S. Pat. No. 3 330 697, July 11, 1967
- [5] A. Prnová, K. Bodišová, R. Klement, M. Migát, P. Veteška, M. Škrátek, E. Bruneel, I. Van Driessche, D. Galusek, Preparation and characterization of Yb₂O₃-Al₂O₃ glasses by the Pechini sol gel method combined with flame synthesis, *Ceramics International*, **40**, (2013), 6179
- [6] L. Ding, Q. Zhang, J. Luo, W. Liu, W. Zhou, S. Yin, Preparation, structure and photoluminescence of nanoscaled –Nd:Lu₃Al₅O₁₂, *Journal of Alloys and Compounds*, **509**, (2011), 10167
- [7] X. Zhou, L. Zhang, K. Zhou, Z. wang, Q. Li, Energy transfer and enhanced 1532 nm emission in Er³⁺ and Ce³⁺ co-doped Y₃Al₅O₁₂ nanoparticles, *Materials chemistry and Physics*, **139**, (2013), 327
- [8] A. Prnová, R. Klement, D. Galusek, K. Bodišová, M. Polovka, M. Migát, B. Hruška, Optical properties of Nd³⁺ and Er³⁺ doped yttrium aluminate glasses with different amounts of dopants, In Preparation of ceramic materials. Xth international conference, 18-20th june, 2013 : proceedings. - Košice : Technical University of Košice, 2013, p. 130

Elektricky vodivé kompozity na báze SiC s prídavkom Ti a NbC

Electrically conductive composites based on SiC with addition of Ti and NbC

R. Bystrický¹, J. Sedláček¹, M. Fides², P. Šajgalík¹

¹Ústav anorganickej chémie, Slovenská akadémia vied, Dúbravská cesta 9, 841 04 Bratislava

²Ústav materiálového výskumu, Slovenská akadémia vied, Watsonova 47, 040 01 Košice

ABSTRACT

In this work silicon carbide based composites were prepared by hot-press method. 30, 40 and 50 mass% of Ti and NbC were used as sintering additives. Their molar ratio was kept at 1:1.8 (Ti:NbC). Samples were sintered by two step sintering to avoid the squeezing out the melted titanium above 1668 °C. Composites were sintered at 1650 °C for 3 h and subsequently at 1850 °C for 1 h under mechanical pressure of 30 MPa in Ar atmosphere. Composite with 50 % of Ti-NbC phase showed the electrical conductivity of 240 S·mm⁻¹, the Vickers hardness of the composite was 25.43 GPa. Highest indentation fracture toughness (2.97 MPa·m^{1/2}) was achieved in the sample with 40% of Ti-NbC phase. XRD pattern confirmed the formation of (Ti, Nb)C solid solution in the SiC matrix.

Keywords: silicon carbide, niobium carbide, electrical conductivity, hot-pressing

INTRODUCTION

SiC ceramics are used in many industrial applications such as fusion reactor parts, turbine components, hot-gas filters, optical mirrors, structural parts, diesel particulate filters, heating elements due to its high strength, high hardness, high corrosion and creep resistance [1-9]. Specific characteristics of SiC such as electrical conductivity and high breakdown field, low conduction losses and thermal stability at very high temperatures make it an appropriate material for application in conditions where conventional Si-based devices cannot be used due to their limitation coming from physical properties of Si.

However, densification of SiC without sintering additives or external pressure is difficult.

Oxides of rare earth elements are usually used as sintering additives for densification of silicon carbide ceramics. These additives increases the electrical conductivity of SiC but on the other hand they deteriorate the mechanical properties. [10-14]

Niobium carbide is a good candidate to use as secondary phase in SiC ceramics due to its high stability, high hardness and high wear resistance. Moreover in combination with Ti helps to densify the SiC ceramics and can significantly increase the electrical conductivity of resulted material. [15]

In this work, we focused on adding a Ti-NbC as secondary phase to SiC matrix. The various amounts of Ti-NbC were added and their influence on electrical properties and mechanical properties of final composite was investigated.

EXPERIMENTAL PART

The commercially available powders of β -SiC (HSC-059, Superior Graphite, USA), Ti (TOHO Titanium Co., Japan) and NbC (Japan New Metals Co., Japan) were used for the starting mixtures preparation. The SiC-based composites were prepared by the addition of the various amount of electrically conductive Ti-NbC phase what is a mixture of Ti and NbC in a molar ratio 1:1.8 (Ti:NbC). The chemical composition of starting mixtures are briefly listed in Tab. 1.

Tab. 1: Chemical composition of starting mixtures

Sample	W [mass%]		
	SiC	Ti	NbC
SiC30TiNbC	70	10.8	19.2
SiC40TiNbC	60	14.4	25.6
SiC50TiNbC	50	18.0	32.0

The powder mixtures were homogenized in planetary mill in water with WC balls at 150 rpm for 1 h. The homogenized suspensions were freeze dried. The pre-pressed pellets were hot pressed in two steps: at 1650 °C for 3 h and at 1850 °C for 1 h under mechanical pressure of 30 MPa in Ar atmosphere.

The densities of the samples were measured by Archimedes method in mercury. The theoretical densities were calculated according to the rule of mixtures. The crystalline phases present in the ground samples were identified using X-ray diffraction (XRD) (Panalytical Empyrean, Netherlands, Cu K α radiation).

The electrical conductivity measurement was performed by Van der Pauw method.

RESULTS

Tab. 2 shows the densities of sintered samples. Samples with addition of 40 and 50 mass % of Ti-NbC phase have densities near theoretical density. Sample SiCN30 has density only 91.7 % of theoretical density.

Tab. 2: The density and relative density of samples after sintering at 1850 °C

Sample	ρ [g·cm ⁻³]	TD [%]
SiCN30	3.44	91.7
SiCN40	3.86	97.2
SiCN50	4.14	98.3

Fig. 1 shows the XRD patterns of prepared composites.

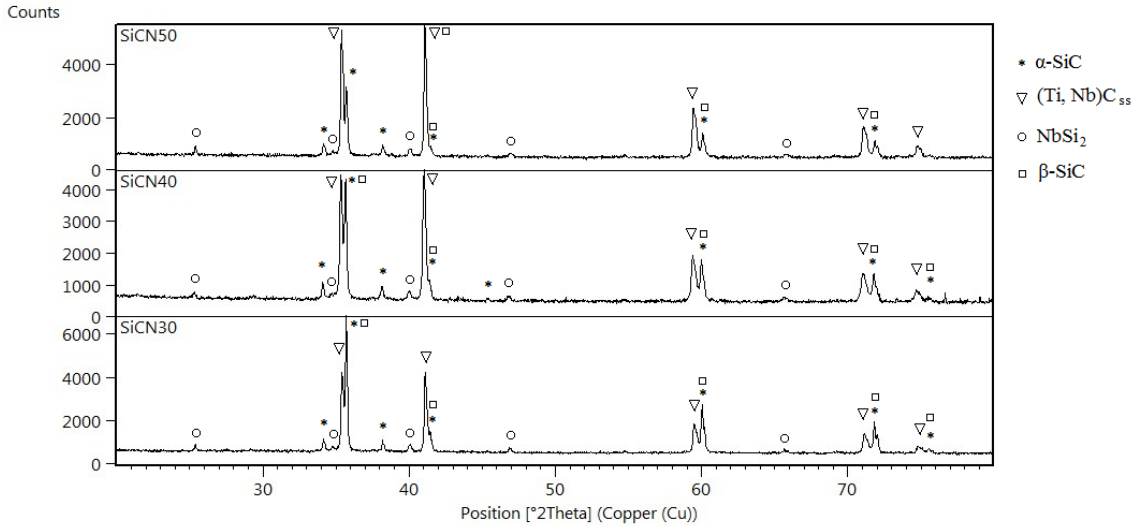


Fig. 1: Comparison of XRD patterns of sintered samples

XRD patterns of SiC30TiNbC, SiC40TiNbC, SiC50TiNbC showed that the samples contain β-SiC (ICDD 03-065-0360) and α-SiC (ICDD 01-073-1663) as a result of β→α transformation, also (Ti, Nb)C_{ss} (ICDD 03-065-7915) and NbSi₂ (ICDD 03-065-3551) as secondary phases. Presence of higher content of solid solution encourages phase transformation of SiC matrix.

Fig. 2 shows the hardness and indentation fracture toughness of prepared composites compared to reference sample.

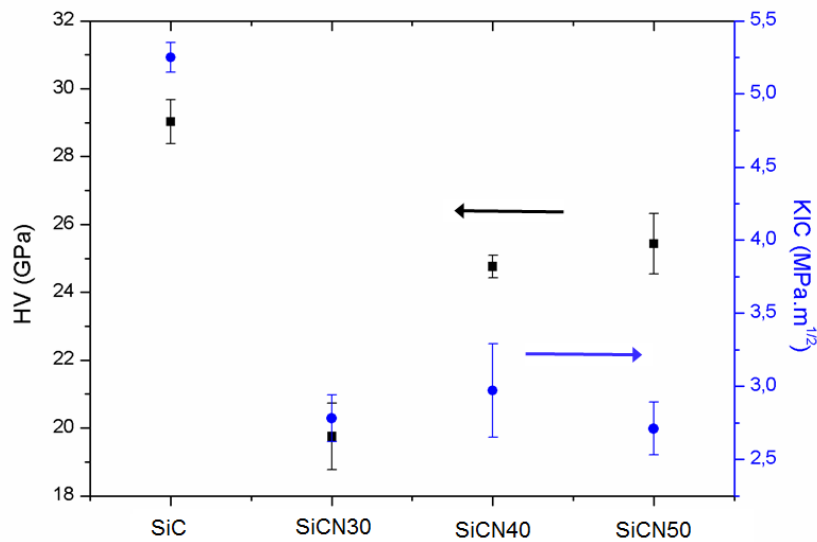


Fig. 2: Hardness and indentation fracture toughness of composites and reference SiC [16]

The hardness values increase from 19.8 GPa for SiCN30 to 25.4 GPa for SiCN50. The lowest hardness in the SiCN30 composite is connected to the higher porosity which is approximately 8%. Comparing to the reference SiC without any additives, hardness of the composites are lower. In the case of indentation fracture toughness addition of Ti-NbC also decreases the fracture toughness of SiC ceramics.

Fig. 3 shows the electrical conductivity of composites comparing to SiC reference sample.

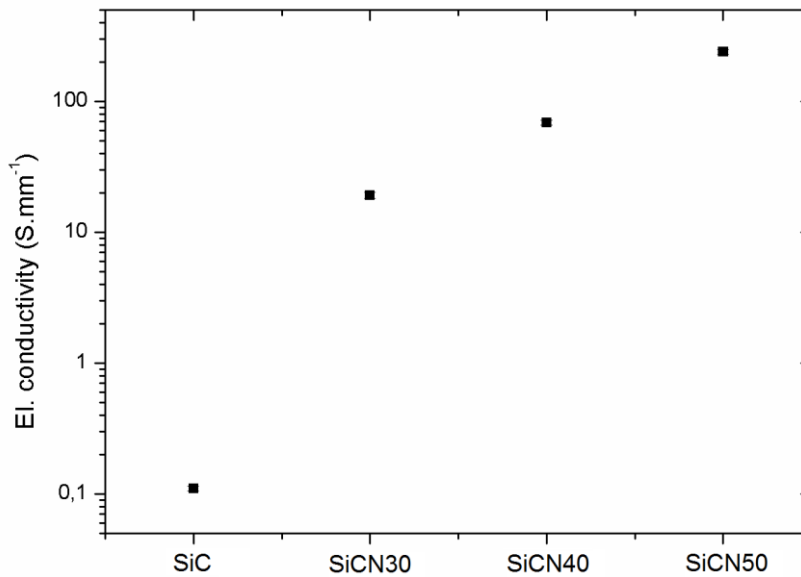


Fig. 3: Electrical conductivity of composites and reference SiC [16]

As it can be seen the electrical conductivity of the composites are up to 3 orders of magnitude higher than in reference sample and varied from 19.15 to 240 S·mm⁻¹. Comparing to other composites, SiCN50 composite has 2 orders of magnitude higher value than other published composites with high electrical conductivity [10-14, 17]. Despite the fact that the composition of composites were the same as in case of the work of Frajkorova [15], higher values of the electrical conductivity were reached in this work. We attributed this difference to another method of drying the powder after homogenization. While in the work of Frajkorova [15] vacuum evaporization was used to drying the suspensions, in our work mixtures were sprayed into the liquid nitrogen where the suspensions were immediately frozen. Therefore there was no separation of phases due to their different density. Water was then removed by freeze drying. With this drying method better distribution of conductive phase in powder mixtures were achieved.

CONCLUSIONS

Electrically conductive SiC composites were prepared by using NbC and Ti as sintering additives. Composites were sintered at 1650 °C for 3 h and subsequently at 1850 °C for 1 h under mechanical pressure of 30 MPa in Ar atmosphere.

The increasing content of Ti-NbC phase led to the increase of hardness. On the other hand, addition of Ti-NbC phase decreases the indentation fracture toughness of composites comparing to reference SiC without any additives. The presence of Ti-NbC phase significantly increased the electrical conductivity of SiC composites. The highest electrical conductivity 240 S·mm⁻¹ was reached in the SiCN50 composite.

SiC composites with electrically conductive Ti-NbC phase are promising materials as alternative to Si in microelectronics.

ACKNOWLEDGEMENT

This work was supported by the Slovak Grant Agency VEGA Project No. 2/0065/14, APVV-0108-12 and ERANET (GRACE). This publication is the result of the project implementation: „Applied research of technology of thermal plasma processes“, ITMS code

26240220070, supported by the Research & Development Operational Programme funded by the ERDF.

REFERENCES

- [1] Baxter, D., Bellosi, A., Monteverde, F. Oxidation and burner rig corrosion of liquid phase sintered SiC, *J. Eur. Ceram. Soc.*, 20 (2000), 367–382
- [2] Magnani, G., L. Minocari, G. L., Pilotti, L. Flexural strength and toughness of liquid phase sintered silicon carbide, *Ceram. Int.*, 26 (2000), 495–500
- [3] Sciti, D., Bellosi, A. Effects of additives on densification, microstructure and properties of liquid-phase sintered silicon carbide, *J. Mater. Sci.*, 35 (2000), 3849–3855
- [4] Rixecker, G., Wiedmann, I., Rosinus, A., Aldinger, F. High-temperature effect in the fracture mechanical behavior of silicon carbide liquid-phase sintered with AlN–Y₂O₃ additives, *J. Eur. Ceram. Soc.*, 21 (2001), 1013–1019
- [5] Strecker, K., Hoffmann, M. J. Effect of AlN-content on the microstructure and fracture toughness of hot-pressed and heat-treated LPS-SiC ceramics, *J. Eur. Ceram. Soc.*, 25 (2005), 801–807
- [6] Jenny, J. R., Malta, D. P., Muller, S. G., Powell, A. R., Tsvetkov, V.F., Hobgood, H.M., Galss, R.C., Carter Jr, C.H. High-purity semi-insulating 4H-SiC for microwave device applications, *J. Electron. Mater.*, 32 (2003), 432–436
- [7] Hayun, S., Paris, V., Mitrani, R., Kalabukhov, S., Dariel, M.P., Zaretsky, E., Frage, N. Microstructure and mechanical properties of silicon carbide processed by Spark Plasma Sintering (SPS), *Ceram. Int.*, 38 (2012), 6335–6340
- [8] Borrero-Lopez, O., Ortiz, A.L., Ciudad, E., Rodriguez-Rojas, F., Guiberteau, F. Microstructural evolution and contact-mechanical properties of SiC ceramics prepared colloiddally with low additive content, *Ceram. Int.*, 38 (2012), 5979–5986
- [9] Hermann, M., Standke, G., Hohn, S., Himpel, G., Gestrich, T. High-temperature corrosion of silicon carbide ceramics by coal ashes, *Ceram. Int.*, 40 (2014), 1471–1479
- [10] Kim, Y.W., Kim, K.J., Kim, H.C., Cho, N.H., Lim, K.Y. Electrodischarge-machinable silicon carbide ceramics sintered with yttrium nitrate. *J. Am. Ceram. Soc.*, 94 (2011), 991–3.
- [11] Román-Manso, B., Domingues, E., Figueiredo, F. M., Belmonte, m., Miranzo, P. Enhanced electrical conductivity of silicon carbide ceramics by addition of graphene nanoplatelets, *J. Eur. Ceram. Soc.*, 35 (2015), 2723–2731
- [12] Lim, K.Y., Kim, Y.W., Kim, K.J., Yu, J.H. Effect of in situ-synthesized nano-size SiC addition on density and electrical resistivity of liquid-phase sintered silicon carbide ceramics, *J. Ceram. Soc. Jpn.*, 119 (2011), 965–7.
- [13] Zhan, G.D., Mitomo, M., Xie, R.J., Mukherjee, A.K. Thermal and electrical properties in plasma-activation-sintered silicon carbide with rare-earth-oxide additives, *J. Am. Ceram. Soc.*, 84 (2001), 2448–50.
- [14] Can, A., McLachlan, D.S., Sauti, G., Herrmann, M. Relationships between microstructure and electrical properties of liquid-phase sintered silicon carbide materials using impedance spectroscopy. *J. Eur. Ceram. Soc.*, 27 (2007), 1361–3.
- [15] Frajkorová, F., Lenčėš, Z., Šajgalík, P. Electrically conductive silicon carbide without oxide sintering additives, *J. Kor. Ceram. Soc.*, 49 (2012), 342–346

- [16] Šajgalík, P., Sedláček, J., Lenčěš, Z., Dusza, J., Lin, H.T. Additive-free hot-pressed silicon carbide ceramics - A material with exceptional mechanical properties. *J. Eur. Ceram.Soc.*, 36 (2016), 1333-41
- [17] Hanzel, O., Sedláček, J., Šajgalík, P. New approach for distribution of carbon nanotubes in alumina matrix, *J. Eur. Ceram. Soc.*, 34 (2014), 1845-51

Príprava a luminiscenčné vlastnosti Mn^{2+} dopovanej $MgAl_2O_4$ keramiky. Preparation and luminescent properties of Mn^{2+} -doped $MgAl_2O_4$ ceramics.

P. Švančárek¹, R. Klement¹, D. Galusek¹

¹ *Vitrum Laugaricio - Joint Glass Center of the IIC SAS, TnUAD, and FChPT STU, 911 50 Trenčín, Slovak Republic*

ABSTRACT

A series of Mn^{2+} -doped $MgAl_2O_4$ spinel specimens was prepared. The first series was prepared from a commercial spinel powder to which 0, 0.1, 0.2, 0.4, and 0.8 at. % of Mn^{2+} active atom was added in the form of $Mn(ac)_2$. Second series was prepared by co-precipitation of solutions which contained $Mg(NO_3)_2$, $Al(NO_3)_3$ and $Mn(ac)_2$ in the amounts according to the formula $Mg_{1-x}Al_2O_4 \cdot xMn^{2+}$ where x was adjusted to 0, 0.1, 0.2, 0.4, and 0.8 at. %. Co-precipitated specimens show patterns of nanocrystalline spinel in X-ray powder diffraction (XRD) records after 12 hours of annealing at 800 °C. While phosphors prepared from commercial spinel powder exhibit a green emission centered at about 520 nm, phosphors prepared by co-precipitation showed the emission at 650 nm due to oxidation of Mn^{2+} to Mn^{4+} by NO_3^- anions. In both sets of prepared phosphors the strongest green/red emission was observed when doped by 0.2 at % of Mn^{2+} .

Keywords: spinel, Mn^{2+} -doping, green emission, photoluminescence

INTRODUCTION

$MgAl_2O_4$ spinel is a mixed oxide with good mechanical properties such as hardness, fracture toughness, high melting temperature (2135 °C) and good electrical insulating properties. It crystallizes in cubic, face centered group that is favorable for preparation of transparent ceramics due to its optical isotropy. It has broad window of transparency in between 250-6500 nm. Addition of small amounts of transition metal ion dopants into atomic lattice of spinel often leads to luminescence. Examples of dopants include manganese (Mn^{2+} -for green emission, and Mn^{4+} - for red emission), nickel (Ni^{2+} - for emission in infrared part of spectra), cobalt (Co^{2+} -for red emission), chrome resp. titanium (Cr^{3+} resp Ti^{3+} - for blue emission). Commercial applications range from LED diodes for solid state lighting to tunable solid state lasers. For example Co^{2+} -doped $MgAl_2O_4$ single crystals can be used as active media for passive Q-switch of lasers operating in the spectral range of 1.3–1.6 μm [1].

EXPERIMENTAL

Commercial powder. The commercial $MgAl_2O_4$ spinel powder obtained from Baikowski (Baikalox S30CR), with 99+% purity, the average particle size of agglomerated particles was 250nm (composed of \approx 60 nm particles) and a specific surface of 30 m²/g was used (Fig. 1). Five suspensions of composition of final material corresponding to $MgAl_2O_4 \cdot xMnO$ where x = 0, 0.1, 0.2, 0.4, 0.8 mol.% were prepared by mixing the spinel powder with calculated amount of manganese diacetate tetrahydrate (Acros Organics, 99+% purity) in distilled water. Aqueous solution of Darvan C-N (Vanderbilt Chemicals LLC) was added as defloculant, in 150 % of the recommended amount relative to the spinel surface. Excess of citric acid (AFT Bratislava, 99.8 % purity) was added (about 25 times of the molar amount of Darvan C-N) to prevent hydrolysis of manganese diacetate by Darvan C-N in the suspension. The suspension was homogenized by ball milling for 24 hours, then evacuated to remove air microbubbles. Then the suspensions were poured into Teflon dies to dry. After several days, the pellets were

further dried in electric oven in air to constant weight at 100 °C, and then sintered at 1600 °C for 1 hour with the heating rate of 10 °C/min, followed by free cooling inside the furnace.

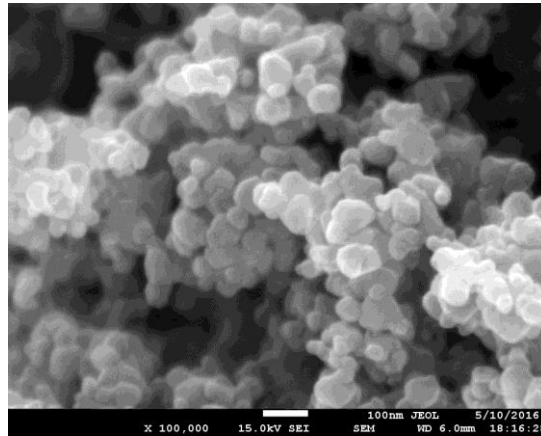


Fig 1: Microstructure of the commercial spinel powder.

Co-precipitated powder. $\text{Al}(\text{NO}_3)_3 \cdot 9\text{H}_2\text{O}$ (AFT Bratislava, for analysis, 98+% purity), $\text{Mg}(\text{NO}_3)_2 \cdot 6\text{H}_2\text{O}$ (Lachema Brno, purum, recrystallized) and manganese diacetate tetrahydrate (Acros Organics, 99+% purity) were added to distilled water as to create 1M solutions with the composition of $\text{Mg}_{1-x}\text{Mn}_x\text{Al}_2\text{O}_4$ where $x = 0, 0.1, 0.2, 0.4, 0.8$ at.%. The solution was added dropwise into a vigorously stirred 1 M solution of ammonium hydroxide (AFT Bratislava, for analysis, 25% solution in water). The amount of 1M ammonium hydroxide solution was determined as 5 times of the amount needed for hydrolysis of nitrate and acetate salts. Obtained precipitate was filtered by vacuum filtration and rinsed by distilled water. Precipitate was then dried at 100 °C overnight (approximately 12 hours), ball milled to receive fine powder and then annealed at 800 °C for 12 hours. Obtained powder was characterized by XRD (Panalytical Empyrean, $\text{CuK}\alpha$ radiation, 2θ range 10 - 80 °). After that, the powder was axially pressed into pellets in a steel die at 100 MPa and the resulting pellets with diameter of 12 mm and approximately 2 mm thick were heated at 5 °C/min to 1100 °C with 1 hour dwell time, followed by 5 °C/min heating to 1300 °C with 20 minutes dwell time, and eventually free cooled inside the furnace.

Scanning electron microscope (JEOL JSM-7600 Thermal FE SEM) was used for imaging powder, fracture planes and polished surfaces of specimens.

Both the emission and excitation fluorescence spectra were measured by Fluorolog 3 (FL3-21, Horiba) fluorescence spectrometer.

RESULTS

Commercial spinel powder is composed of agglomerates. These agglomerates are made from nanocrystals of about 60 nm in diameter, bound together into agglomerates of 200-400 nm in size, as shown in Fig 1. While it is easy to create stabilized suspension from this powder, the quality of slip cast pellets is low due to irregular shape and different sizes of spinel agglomerates. It results in low green density, and fragility of the pellets. High sintering temperatures are also needed (1600 °C for 1 hour). The highest density obtained was 94.7 % for undoped spinel specimen (Fig. 2). Due to high sintering temperatures required, the sintered microstructure is composed of large grains as shown in Fig. 2a. The sintered specimens also contain large pores, several micrometers in diameter. When manganese is introduced into the suspension, citric acid has to be added to suppress hydrolysis of manganese acetate by the dispersant Darvan C-N. Even if hydrolysis was visibly suppressed, the quality of casts was impaired considerably.

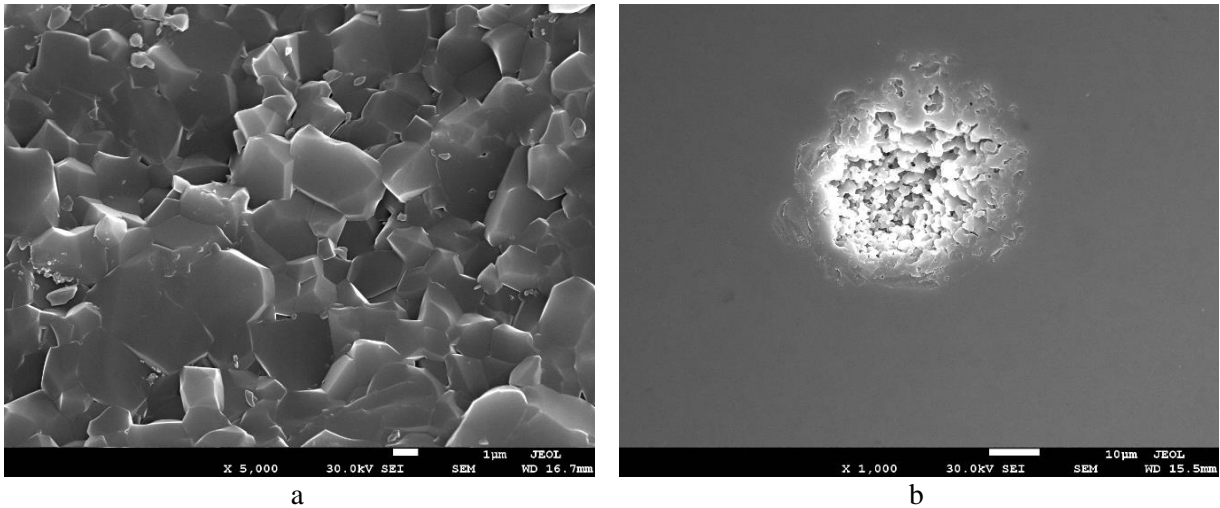


Fig 2: Fracture plane (a) and polished surface (b) of slip cast pellets prepared from the commercial powder.

Alternative approach - preparation of co-precipitated powders from solutions - was therefore applied. While this approach can be tricky, the benefit is in obtaining fine grained powders without chemically bonded hard agglomerates which allows the use of very low sintering temperatures [2]. Another benefit is the possibility to prepare powders with nearly homogeneously distributed optically active metal cation dopants. Prepared spinel powders were nanocrystalline as demonstrated by X-ray diffraction peaks broadening in the as-received powder (Fig. 3b) and SEM (Fig.4.).

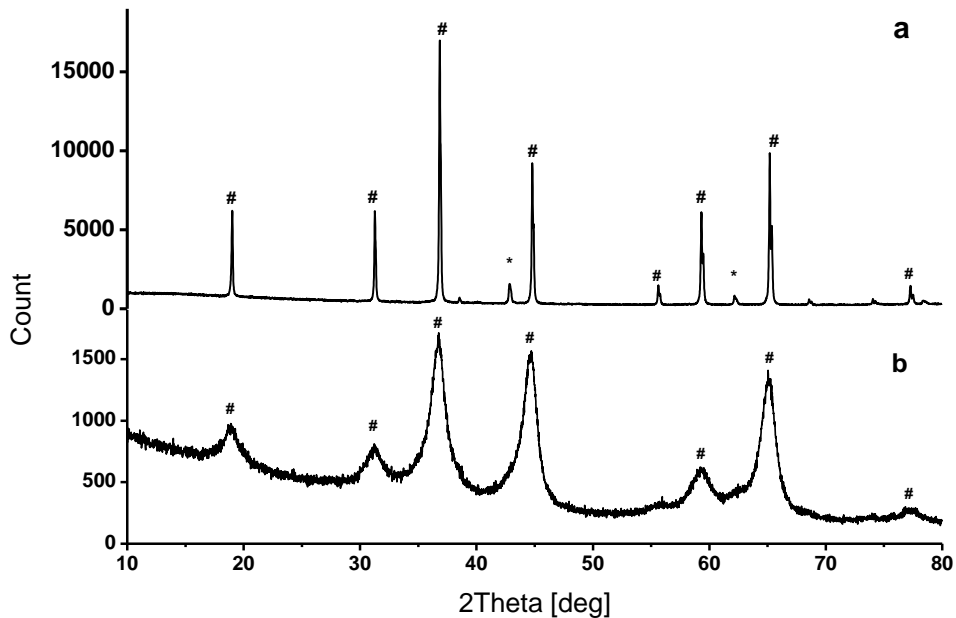


Fig 3: XRD analysis of sintered pellet (a) and of calcined powder before sintering (b) Spinel diffractions are marked by (#) and periclase (MgO) diffractions are marked by (*)

After sintering the width of X-ray diffraction peaks was significantly smaller, indicating grain growth, and possibly the crystallization of amorphous precipitate leftovers (Fig 3a). Micrograph of precipitated and calcined powder is shown on Fig. 4a. An average particle size of the co-precipitated powder is about 10 nm which grows during sintering up to average grain size of 120nm (Fig. 4b). Green pellets were pressed with pressures of 100MPa obtaining average green density of 40%. This low green density suggests presence of agglomerates and

inhomogeneities in green specimens. After firing for 20 minutes at 1300 °C specimens reached densities of 76-82 %. This very low value is due to agglomerated starting powder and of low sintering temperature. Higher pressures, often in the GPa range, are necessary to crush agglomerates and overcome friction forces acting between nanoparticles when using uniaxial pressing [3].

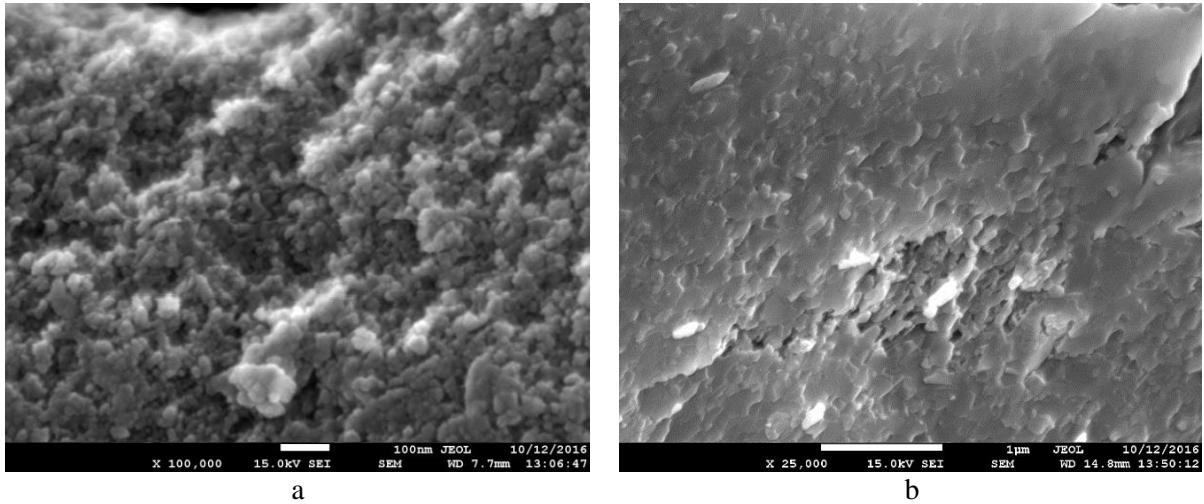


Fig. 4: Micrograph of agglomerated precipitate (a) and of sintered precipitate – fracture plane (b)

The temperature 1300 °C was used according to literature [2], where green pellets contained 9 nm particles and 95.5% relative density was reached after 20 minutes of sintering while keeping grain growth low. Clearly, in this work the agglomerates interfered and prevented obtaining of well-ordered structure of green pellets and influenced the final density of sintered product.

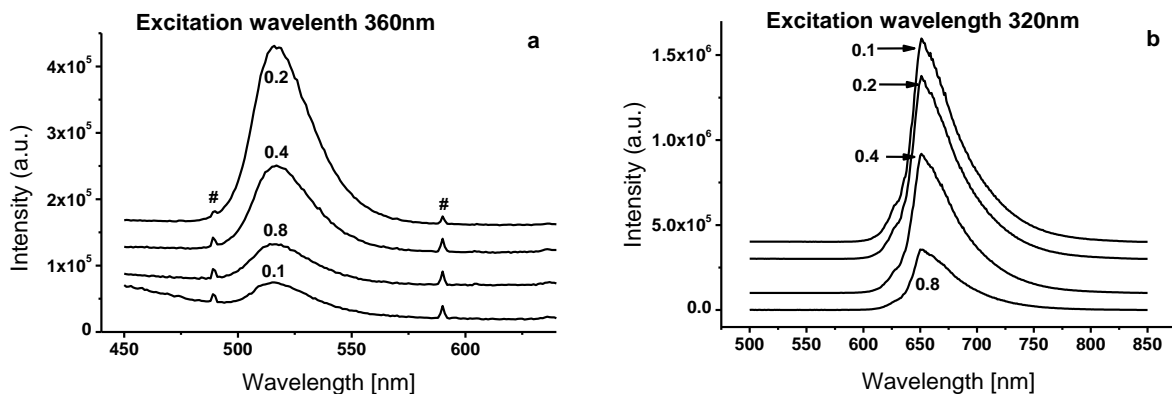


Fig. 5: Luminescence spectra of specimens prepared from commercial spinel by slip casting (a) and by co-precipitation (b). (#) is artefact of measurement.

The photoluminescence emission spectra are shown in Fig. 5. The Mn^{2+} doped spinel prepared from commercial nanopowder (Fig. 5a) exhibits relatively strong green emission centered at 523 nm when excited at 360 nm, corresponding to the d-level spin-forbidden transition of Mn^{2+} ion (${}^4\text{T}_{1g} - {}^6\text{A}_{1g}$). The maximum green emission intensity was observed at the concentration of 0.2 at. % of Mn^{2+} . The spinel prepared by co-precipitation method contains Mn^{4+} ions, which allow relatively strong red emission at 650 nm when excited at 320 nm (Fig. 5b). This corresponds to the spin-forbidden ${}^2\text{E}_g - {}^4\text{A}_{2g}$ electron transition of the tetravalent manganese ions. The maximum red emission intensity was observed at the concentration of 0.1 at. % of Mn^{4+} .

CONCLUSION

A series of MgAl_2O_4 spinel specimens doped by various concentration of manganese dopant was prepared with the goal of obtaining of the strongest luminescence intensity phosphor. The strongest green emission measured by fluorescence spectrometry for 0.2 at. % Mn^{2+} concentration (in case of doped commercial spinel powder). On the other side, by co-precipitation prepared specimens of spinel phosphor showed emission in the red part of spectra, and the strongest intensity was observed for sample doped by 0.1 at. % of Mn^{4+} concentration. The control of active metal ion oxidation state and the fine adjustment of precipitation conditions is necessary to obtain better defined precipitate.

ACKNOWLEDGMENT

The financial support of this work by the projects SAS-NSC JRP 2012/14 and VEGA 1/0631/14, is gratefully acknowledged. This publication was created in the frame of the project "Centre of excellence for ceramics, glass, and silicate materials" ITMS code 262 201 20056, based on the Operational Program Research and Development funded from the European Regional Development Fund.

LITERATURE

- [1] Anis Jouini, Akira Yoshikawa, Alain Brenier, Tsuguo Fukuda, and Georges Boulon: Optical properties of transition metal ion-doped MgAl_2O_4 spinel for laser application, *phys. stat. sol. (c)* 4, No. 3, 1380–1383 (2007) / DOI 10.1002/pssc.200673872
- [2] Jorgen Rufner,[‡] § David Anderson,[‡] Klaus van Benthem[‡] and Ricardo H. R. Castro: Synthesis and Sintering Behavior of Ultrafine (<10 nm) Magnesium Aluminate Spinel Nanoparticles, *J. Am. Ceram. Soc.*, 96 [7] 2077–2085 (2013).
- [3] Ł. ZYCH: Consolidation and sintering of nanometric ceramic powders, *Materials Science-Poland*, Vol. 26, No. 2, 2008

Luminiscenčné vlastnosti Ce/Mn kodopovaných luminoforov pripravených pomocou sól-gél metódy

Sol-gel synthesis of Ce/Mn co-doped silicate phosphors and their luminescence properties

P. Veteška¹, A. Prnová², D. Galusek¹

¹ *Department of Inorganic Materials, Institute of Inorganic Chemistry, Technology and Materials, Faculty of Chemical and Food Technology, Slovak University of Technology, Bratislava, Slovak Republic,*

² *Vitrum Laugaricio – Joint Glass Centre of the IIC SAS, TnU AD and FChPT STU, Trenčín, Slovak Republic*

ABSTRACT

The effect of Mn concentration on the luminescence and phase composition of Sr-åkermanite 1 mol % Ce co-doped phosphors prepared by sol-gel synthesis was investigated. Green-yellow luminescence intensity of Mn²⁺ enhanced via the efficient energy transfer from Ce³⁺ to Mn²⁺, increased with the manganese content and reached an optimum at 3.0 mol%. At 4.5 mol% of Mn the green-yellow emission intensity dropped down due to the concentration quenching and was comparable with the luminescence of undoped sample.

However, at the same time an unexpected increase of the broad violet-blue emission (350 to 450 nm) was also observed. This is characteristic for the allowed 5d1–4f1 transition of Ce³⁺. XRD analysis revealed the change in the phase composition and merwinite as a major phase was detected.

Keywords: luminescence, transition element, sol-gel

INTRODUCTION

Due to limited world supplies of rare-earth elements (REE), which are the cornerstone of modern electronics and LED industry, new combinations of doping agents for phosphor preparation must be investigated. The transition elements are a suitable replacement for luminescence materials preparation, should the prices of REE skyrocket again as in the year 2011.

The strontium disilicate - Sr₂MgSi₂O₇ (Sr-based analogue of Ca₂MgSi₂O₇ – åkermanite) has attracted great interest as the phosphor host material and has been widely studied, especially in combination with REE [1 - 3]. The åkermanite phosphors are often prepared by a sol-gel method due to the high homogeneity of prepared material [4, 5].

EXPERIMENTAL

A series of manganese-cerium co-doped strontium åkermanite (Sr₂MgSi₂O₇) based phosphors has been prepared by modified Pecchini method described in [6]. The solution of the respective nitrates and a mixture of ethylene glycol and citric acid have been mixed together. The resulting solution was kept at 85°C for 3 hours to form a sol. Afterwards, the sol has been partially evaporated at 120°C for approximately 16 hours and the dried gel has been crushed in agate mortar and pre-calcined for 2x6 hours at 800°C to remove the residual nitrates and carbon. The powders were subsequently annealed at 1200°C and their phase composition and luminescence properties were examined. Designations of prepared samples are summarised in Tab. 1.

Tab. 1: Sr-åkermanite sample designation

Sample designation	Cerium content mol. %	Manganese content mol.%	Annealing temperature °C
SG2 -0	1	0	1200
SG2 - 1.5	1	1.5	1200
SG2 -3.0	1	3	1200
SG2 -4.5	1	4.5	1200

The phase composition of prepared powders was measured by X-ray powder diffractometer Panalytical Empyrean equipped with Cu X-ray lamp (CuK α radiation with 0.15405 nm wavelength). The fluorescence emission spectra of prepared phosphors were measured using fluorescence spectrometer Fluorolog FL3-21 spectrometer (Horiba Jobin Yvon) using Xe (450°) arc lamp as the excitation source.

RESULTS

X-ray diffraction patterns for series of samples containing various amount of Mn are shown in Fig. 1.

The samples are completely crystalline in nature and usually contain very small amounts of the Sr₃MgSi₂O₈ phase (Sr-merwinite). It seems that the doping of Sr-åkermanite with manganese does not considerably influence the host lattice structure for samples up to 3mol% of Mn.

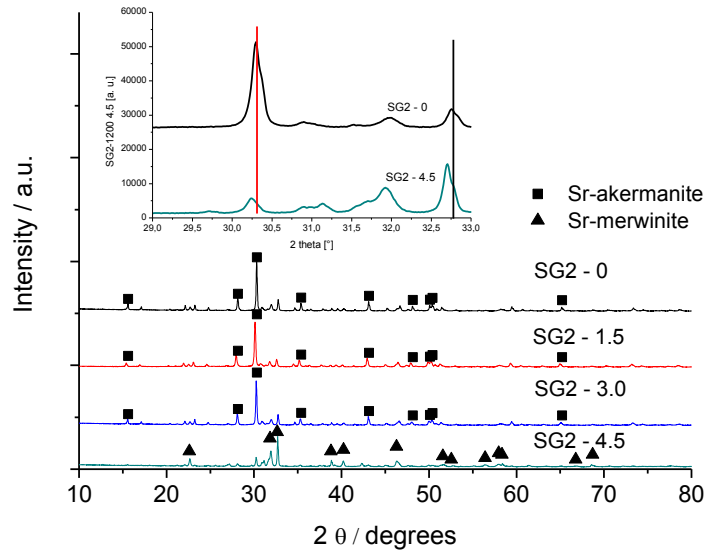


Fig. 1: Results of XRD analyses of prepared Mn-Ce co-doped powders; Inset: shift of åkermanite (red) and merwinite(black) main XRD peak due to lattice distortions.

The SG2-4.5 sample doped with relatively large amount of manganese contains significantly lower fraction of Sr-åkermanite whereas the Sr-merwinite phase becomes a dominant phase. Detailed analysis of XRD patterns of SG2-0 and SG2-4.5 samples also revealed the shift of Sr-åkermanite peaks to the lower angles of 2 Θ for doped sample (Fig.1b). If we consider that the Mn ions can occupy interstitial positions in the tetragonal crystal lattice of åkermanite with the formula Ca₂MgSi₂O₇ then at certain concentration of dopants the crystal structure will be saturated and merwinite monoclinic crystal lattice with the formula Ca₃MgSi₂O₈ can crystallize.

The results of photoluminescence measurements are summarized in Fig. 2. When excited by wavelength of 330 nm (excitation of Ce^{3+}), the SG2-0 sample emits a visible light with wavelengths around 390 – 440 nm (ultraviolet to violet light) with almost no measurable emission at higher wavelengths.

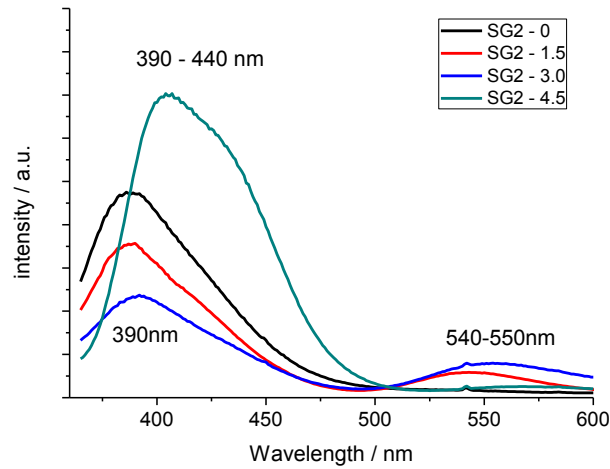


Fig. 2: Emission spectra of Mn-Ce co-doped Sr-åkermanite phosphors after excitation at 330 nm.

When åkermanite samples were co-doped with the 1.5 - 3.0 mol.% Mn^{2+} a new emission band in the green-yellow region (maximum at 540 and 550 nm respectively) appeared. This emission is characteristic for energy transfer from Ce^{3+} to Mn^{2+} [7]. In accordance with theoretical assumption, with increasing amount of Mn^{2+} present the energy transfer intensifies up to the point when concentration quenching occurs. This is accompanied by decrease of Ce^{3+} emission peak at 390 nm. Similar results have been obtained by Zhang et al. [8], studying $\text{Ce}^{3+}/\text{Mn}^{2+}$ co-doped NaSrBO_3 .

According to our previous experiments, samples doped with cerium processed by above described process usually contain some portion of Ce^{3+} and Ce^{4+} ions within the lattice. While the Ce^{3+} are acting as a sensitizer for manganese, the Ce^{4+} do not emit visible light nor enhance the luminescence of manganese. It is assumed that the increase of violet-blue emission in sample SG2-4.5 could be explained by the increase of $\text{Ce}^{3+}/\text{Ce}^{4+}$ ratio due to the large amount of Mn present, which could influence the reduction of Ce^{4+} during forming gas annealing.

CONCLUSION

Luminescence properties and phase composition of sol-gel prepared Ce/Mn co-doped Sr-åkermanite were investigated. Violet-blue and green-yellow emissions were observed. Green-yellow luminescence intensity of Mn^{2+} is enhanced via the efficient energy transfer from Ce^{3+} to Mn^{2+} and the emission increased with increasing manganese concentration, while at the same time the violet-blue emission intensity decreased. The maximum of violet-blue emission is achieved for manganese content of 4.5 mol.%, while the green-yellow emission for this sample was at the minimum (comparable to Ce – only doped sample). The optimal Mn^{2+} concentration for green-yellow emission is 3.0 mol.%.

ACKNOWLEDGMENT

The financial support of this work by the projects SAS-NSC JRP 2012/14 and VEGA 1/0631/14, is gratefully acknowledged. This publication was created in the frame of the project "Centre of excellence for ceramics, glass, and silicate materials" ITMS code 262 201

20056, based on the Operational Program Research and Development funded from the European Regional Development Fund.

LITERATURE

- [1] Li B., Yang J., Wang J., Wu M., Two-color emitting of Eu^{2+} and Tb^{3+} co-doped $\text{Sr}_2\text{MgSi}_2\text{O}_7$ for UV LEDs, *Optical Materials*, **36**, [10], (2014) 1649-1654.
- [2] Yu H., Chen J., Pu Y., Zhang T., Gan S., Photoluminescence properties of Tb^{3+} and Ce^{3+} co-doped $\text{Sr}_2\text{MgSi}_2\text{O}_7$ phosphors for solid-state lighting, *Journal of Rare Earths*, **33**, [4], (2015) 366-370.
- [3] Sahu I. P., Bisen D. P., Brahme N., and Ganjir M., Enhancement of the photoluminescence and long afterglow properties of $\text{Sr}_2\text{MgSi}_2\text{O}_7:\text{Eu}^{2+}$ phosphor by Dy^{3+} co-doping. *Luminescence*, **30**, [8], (2015) 1318–1325.
- [4] Masoud E., Zohreh H., Nmati A., Synthesis and spectral properties of Nd-doped glass-ceramics in $\text{SiO}_2\text{-CaO-MgO}$ system prepared by sol-gel method, *Journal of Rare Earths*, **31**, [6], (2013) 595-599.
- [5] Hao Y., Wang Y.H., Synthesis and photoluminescence of new phosphors $\text{M}_2(\text{Mg, Zn})\text{Si}_2\text{O}_7:\text{Mn}^{2+}$ (M = Ca, Sr, Ba), *Materials Research Bulletin*, **42**, [12], (2007) 2219-2223.
- [6] Prnová A., Bodišová K., Klement R., et al., Preparation and characterization of $\text{Yb}_2\text{O}_3 - \text{Al}_2\text{O}_3$ glasses by the Pechini sol-gel method combined with flame synthesis, *Ceramics International*, **40**, [4] (2014) 6179-84.
- [7] Wang Z, Li P, Guo Q, Yang Z., Luminescence and energy transfer of tunable emission phosphor $\text{Ca}_2\text{PO}_4\text{Cl}:\text{Ce}^{3+}, \text{Mn}^{2+}$, *Spectrochim Acta A Mol Biomol Spectrosc.* Volume 137, (2015), Pages 871–876
- [8] Zhang. X., Zhou, Luminescence Properties of Dual-Emission $\text{Ce}^{3+}, \text{Mn}^{2+}$ Doped NaSrBO_3 Phosphors, *ECS Journal of Solid State Science and Technology*, Volume 2, Issue 5, (2013), Pages R83-R86

Age hardening and toughness enhancement in hard coatings

M. Mikula^{1,2}, T. Roch¹, D. Plašienka¹, M. Truchlý¹, M. Čaplovičová³, P. Kúš¹

¹*Department of Experimental Physics, Faculty of Mathematics, Physics and Informatics, Comenius University, Mlynská Dolina F2, 842 48 Bratislava, Slovakia*

²*Institute of Materials and Machine Mechanics SAS, Račianska 75, Bratislava, Slovakia*

³*Slovak University of Technology in Bratislava, University Science Park Bratislava Centre, Vazovova 5, 812 43 Bratislava, Slovak Republic*

ABSTRACT

Spinodal decomposition of cubic solid solutions during high-temperature exposure resulting in age hardening is well-known phenomenon observed in $Ti_{1-x}Al_xN$ hard coatings. In this paper, the findings of *ab initio* calculations and structural and mechanical analysis show age hardening via spinodal mechanism in $Ta_{1-x}Al_xN$ coatings. Furthermore, obtaining high hardness combined with enhanced toughness represents one of the current challenges in material design of hard ceramic protective coatings. Here, we combine experimental and *ab initio* density functional theory analysis of the mechanical properties of Ti-Al-Nb-N coatings to validate the results of previous theoretical investigations predicting enhanced toughness in TiAlN-based systems highly alloyed (> 25 at.%) with nitrides of pentavalent VB group elements.

Keywords: hard coatings, spinodal decomposition, toughness, *ab initio* calculations

INTRODUCTION

Hard coatings based on ceramic materials such as nitrides, borides, etc., are widely used in engineering systems to protect structural materials during operation in harsh environments. Transition metal nitrides (TMNs), especially Ti-Al-N and Cr-Al-N ternaries, generally characterized by cubic NaCl-structure (B1) solid solutions are typical representatives of contemporary industrial coatings with emphasis on high hardness, high thermal stability, good oxidation resistance, and chemical inertness which allow for significant extension of tools' lifetimes ultimately resulting in drastic reductions of costs caused by wear [1]. Thermally-induced processes produce an increase in the hardness of TMNs, so-called age hardening [2], deriving from decomposition of cubic solid solutions via a spinodal mechanism or precipitation leading to formation of fine-grained nanostructures, in the early stages of phase separation. However, continuous thermal load/unload cycles during industrial machining cause transformation into thermodynamically more stable coarse-grained structures containing hexagonal ZnS-type (wurtzite) AlN and cubic TiN or CrN_x phases resulting in losses of excellent mechanical properties [2]. In order to further improve and/or tune the aforementioned TMNs properties, the concept of multicomponent alloying with nitrides of elements from groups IIIB, IVB, VB and VIB (Y, Zr, Hf, V, W, Nb, Ta, and Mo) is a promising approach [3]. Unfortunately, ceramics are typically characterized by inherently low toughness [4], where the latter is defined as material's ability to resist crack initiation and propagation up to fracture. Sangiovanni et al., using *ab initio* calculations of elastic properties and electronic structure analyses, reported on toughness enhancements for TMN pseudobinaries characterized by valence electron concentrations (VEC) ≥ 10 [4]. The electronic origin for ductility was found to stem from optimized occupancy of metallic shear-sensitive d-d states located at the Fermi level. Incorporation of elements providing increased d-electron concentrations (e.g. Nb, Ta, Mo, and W), significantly changes the electronic structure of TiAlN, which evolves from exhibiting occupied anti-bonding metal-metal states into highly bonding metallic states while preserving strong metal-N bonding. Here, we use

experimental methods supported by *ab initio* density functional theory (DFT) calculations and analysis to investigate the structural and mechanical behavior of ternary Ta-Al-N and highly Nb-alloyed Ti-Al-N coatings prepared by reactively unbalanced direct current magnetron co-sputtering.

EXPERIMENTAL DETAILS

In the present work, 4- μm -thick Ta-Al-N films are grown on mirror-polished Al_2O_3 plates (sapphire) at 450°C by means of reactive unbalanced magnetron sputtering from a powder sintered TaAl target (Ta/Al ratio of 1:1, 50 mm in Dia., 99.5% purity) in Ar + N_2 (both of 99.999% purity) discharge. The magnetron power density was fixed at 6 W cm^{-2} , yielding deposition rate R of $2.85 \mu\text{m h}^{-1}$. All depositions were carried out at a negative substrate bias of -50 V for the used sputtering conditions. The total working gas pressure during the deposition was kept at $\sim 6.7 \times 10^{-1} \text{ Pa}$ with a N_2 partial pressure of $\sim 1.5 \times 10^{-1} \text{ Pa}$. The as-deposited Ta-Al-N coatings were annealed in vacuum (below 10^{-3} Pa) at temperatures of 900°C , 1000°C , 1100°C , 1200°C and 1300°C for 3 min using a heating rate of $30^\circ\text{C min}^{-1}$ and self-limiting cooling rate. Ti-Al-Nb-N coatings were prepared using reactive unbalanced dc magnetron co-sputtering from TiAl target ($\sim 50/50 \text{ at. } \%$, 100 mm dia., 99.5 % purity) and Nb target (100 mm dia., 99.99 % purity). Deposition was carried out in a flowing Ar + N_2 mixture atmosphere. The magnetrons were tilted with the angle of $\sim 50^\circ$ between their axes. The magnetron power densities were set to 6.8 Wcm^{-2} and 7.0 Wcm^{-2} for the TiAl and the Nb targets, respectively. All depositions were carried out at a floating potential on the samples heated to 450°C for the used sputtering conditions. The chemical composition of the coatings was determined via scanning electron microscopy using energy or wavelength dispersive x-ray spectroscopy (EDS/WDS). Structural evolution of the films was observed by Bragg-Brentano X-ray diffraction (XRD) measurements using PANalytical X'pert PRO MRD diffractometer with $\text{CuK}\alpha$ radiation. Detailed studies of the nanostructure of selected samples were conducted with high-resolution transmission electron microscopy (HR-TEM, JEOL ARM 200), analytical scanning transmission electron microscopy (STEM), and selected area electron diffraction (SAED). Mass-thickness contrast images were recorded with an annular dark-field (ADF) detector. Chemical compositions in nanoscale were measured with energy-dispersive x-ray spectroscopy (EDS) during STEM investigations. Specimen preparation was performed using focused ion beam (FIB) work station. The indentation hardness H and effective Young's modulus E of the coatings were measured and calculated using a nanoindenter equipped with a Berkovich diamond tip at a constant load of 10 mN keeping penetration depths below 10% of the film thickness. *Ab initio* density-functional theory (DFT) calculations, performed to support the experimental data, were carried out using the VASP 5.3 code employing projector-augmented wave pseudopotentials and Perdew-Burke-Ernzerhof parametrization of exchange-correlation functional [PBE].

RESULTS

Ta-Al-N coatings

Elemental WDS analysis reveals that Ta-Al-N coatings are stoichiometric, with a nitrogen content of $\approx 50 \pm 2 \text{ at. } \%$ and a N/ (Ta+Al) ratio of 1 ± 0.02 . The metal content is normalized to 50 at. % leading to the notation $\text{Ta}_{1-x}\text{Al}_x\text{N}$ and a composition of $\text{Ta}_{0.55}\text{Al}_{0.45}\text{N}$. According to *ab initio* calculation, $\text{Ta}_{1-x}\text{Al}_x\text{N}$ thin films exhibit energetical preference for cubic structure up to $x = 0.6$ and for wurtzite structure for higher Al content. In the region of x between approx. 0.5 and 0.8, however, the E_f values for cubic and wurtzite structures are very similar and hence a dual cubic/wurtzite structure is likely to be formed. XRD pattern (not shown) of as-deposited $\text{Ta}_{0.55}\text{Al}_{0.45}\text{N}$ coating suggests a dual phase structure composed of a cubic B1 phase

which is represented by a strong 200 reflection at $2\theta \sim 41.7^\circ$ and identified as TaAlN solid solution and wurtzite phase fraction resulting in a low-intensity very broad reflection in 2θ range between 32° and 38° . XRD pattern of annealed coatings at 1100°C , indicates decomposition process in TaAlN solid solution where w-AlN reflections increase. Result of these thermally-induced processes is N_2 -depleted structure containing understoichiometric h-Ta N_x and wurtzite w-AlN and residual Ta_2O_5 phases after annealing at 1300°C .

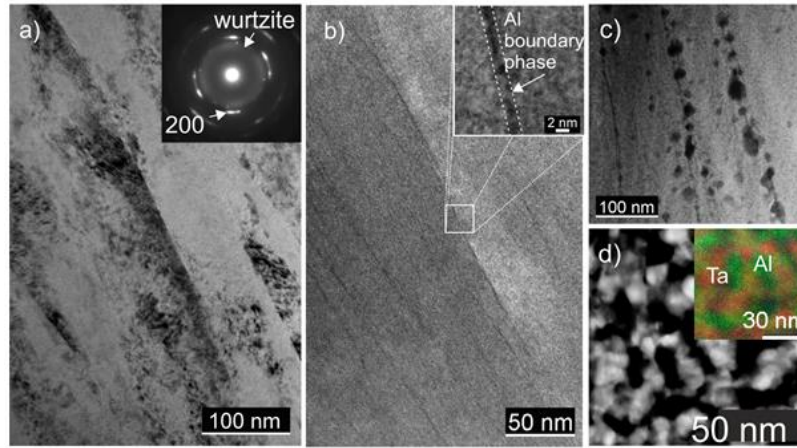


Fig 1: a-b) TEM and STEM-ADF micrograph of as-deposited $\text{Ta}_{0.55}\text{Al}_{0.45}\text{N}$ coating; c) annealed coating at 1000°C and d) annealed at 1100°C after decomposition in vacuum.

Cross-sectional bright-field TEM micrograph (Fig. 1a) obtained from the as-deposited $\text{Ta}_{0.55}\text{Al}_{0.45}\text{N}$ film shows the structure consisting of pronounced columnar grains. STEM-ADF investigation reveals (Fig. 1b) the film seems to have open-voided column boundaries, identified by dark lines separating the columns which represent a phase with lower density. Line scan STEM-EDS analysis (not shown) revealed very high Al content in these $\sim 2\text{-}3$ nm thick regions consisting of very small precipitates. Column boundaries are dissolved (Fig. 1c) after the temperature exceeds 1100°C and a fine-textured structure consisting of subgrains of diameter in the range of $30\text{-}60$ nm forms during decomposition of TaAlN solid solution (Fig. 1c). STEM-EDS map (inset in Fig. 1d) carried out in the decomposed structure after annealing at 1200°C reveals two chemically separated Ta and Al containing nitride phases.

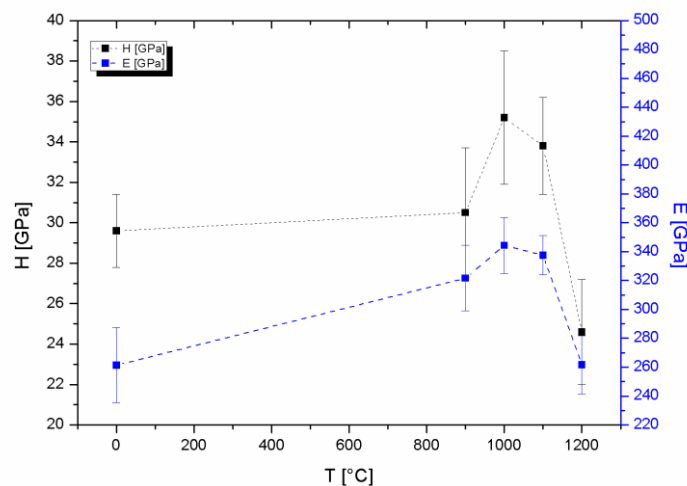


Fig. 2: Mechanical properties of $\text{Ta}_{0.55}\text{Al}_{0.45}\text{N}$ coatings as a function of annealing temperature.

The corresponding age hardening effect due to spinodal decomposition of cubic solid solution can be seen in the hardness evolution of $\text{Ta}_{0.55}\text{Al}_{0.45}\text{N}$ as a function of annealing temperature presented in Figure 2. $\text{Ta}_{0.55}\text{Al}_{0.45}\text{N}$ coatings with a dual phase structure in as-deposited state

exhibit hardness values of $H = 29.6 \pm 1.8$ GPa, which remain almost constant also after thermal exposure at 900°C . Significant increase in hardness $H = 35.2 \pm 3.3$ GPa is observed in the coatings annealed at 1000°C . This age hardening is a result of coherency strains between cubic solid solution and coherent small TaN and AlN domains formed during the early stages of the phase separation. Therefore, the hardness increases because extra stress is required to propagate dislocations through these domains. Increased bulk diffusivity in decomposed cubic TaAlN due to ongoing thermal load lead to the formation of stable, coarse-grained w-AlN and understoichiometric h-TaN_{1-x} phases resulting to a decrease in hardness of 24.6 ± 2.6 GPa.

Ti-Al-Nb-N coatings

Elemental analysis by EDS reveals that our as-deposited Ti-Al-Nb-N coatings are stoichiometric (the nitrogen content $\sim 50 \pm 2$ at. %) with $N/(Ti+Al+Nb)$ ratios of 1.00 ± 0.01 . Content of metals is normalized to 50 at. % leading to the notation $Ti_{1-x-y}Al_xNb_yN$ and following compositions: $Ti_{0.46}Al_{0.54}N$, $Ti_{0.35}Al_{0.43}Nb_{0.22}N$, $Ti_{0.27}Al_{0.40}Nb_{0.33}N$, $Ti_{0.24}Al_{0.33}Nb_{0.43}N$, $Ti_{0.20}Al_{0.28}Nb_{0.52}N$, and $Ti_{0.18}Al_{0.21}Nb_{0.61}N$. The difference in the structure of as-deposited $Ti_{1-x-y}Al_xNb_yN$ coatings with various Nb contents is illustrated by XRD patterns in a 2θ range between 40° and 54° (Fig. 3a). Analysis of the patterns shows that all $Ti_{1-x-y}Al_xNb_yN$ coatings crystallize in a single phase cubic B1 structure identified as TiAl(Nb)N solid solutions.

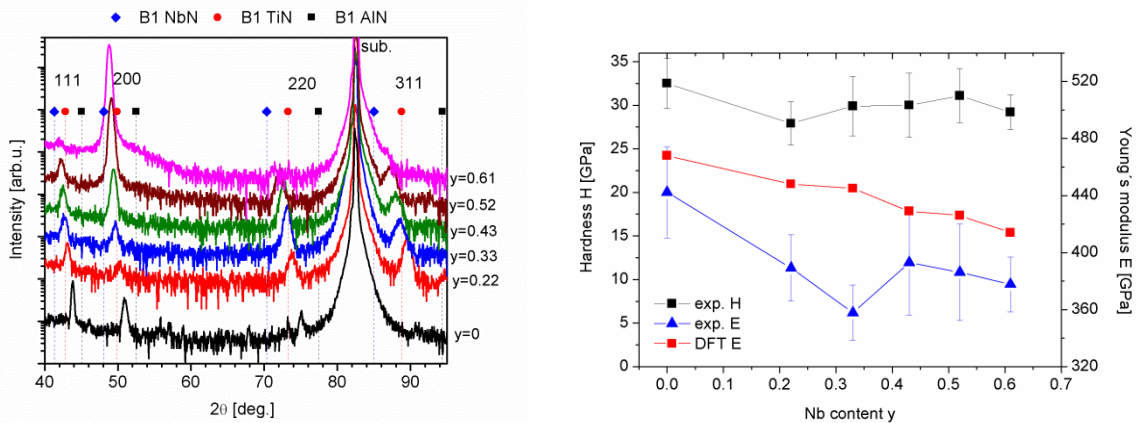


Fig. 3: a) XRD pattern of as-deposited Ti-Al.Nb-N coatings; b) Hardness and Young's modulus of as-deposited Ti-Al.Nb-N coatings as a function of niobium content.

Indentation hardness H and Young's modulus E of $Ti_{1-x-y}Al_xNb_yN$ are plotted as a function of Nb content in Fig. 3b. The $Ti_{0.46}Al_{0.54}N$ coating, which exhibits preferred 111 growth-orientation, possesses the highest hardness ~ 32.5 GPa and Young's modulus ~ 442 GPa. The hardness of NbN-alloyed Ti-Al-N is slightly reduced compared to $Ti_{0.46}Al_{0.54}N$ and remains approximately constant (between 28 ± 2 and 31 ± 3 GPa) for all Nb contents (the variations in hardness are within error bars, Fig. 4). Quaternary alloy $Ti_{1-x-y}Al_xNb_yN$ coatings exhibit significantly lower values of Young's moduli in comparison to $Ti_{0.46}Al_{0.54}N$. The lowest E value, ~ 358 GPa, is observed for $y = 0.33$. The coatings with higher Nb concentration show slightly higher values of Young's moduli ranging from ~ 378 to ~ 389 GPa.

$Ti_{1-x-y}Al_xNb_yN$ ductility trends plotted in Fig. 4 show monotonic increases in Cauchy's pressures C_{12} - C_{44} and decreases in G/B ratios as a function of y . C_{12} - C_{44} and G/B DFT values obtained for TiAlN are -53 GPa and 0.719 , respectively. For increasing Nb concentrations, Cauchy's pressures become progressively less negative (slightly positive for $y = 0.61$) while G/B ratios decrease steadily up to 0.588 . Thus, according to Pettifor and Pugh criteria, TiAlNbN alloys are more ductile, or at least less brittle than TiAlN.

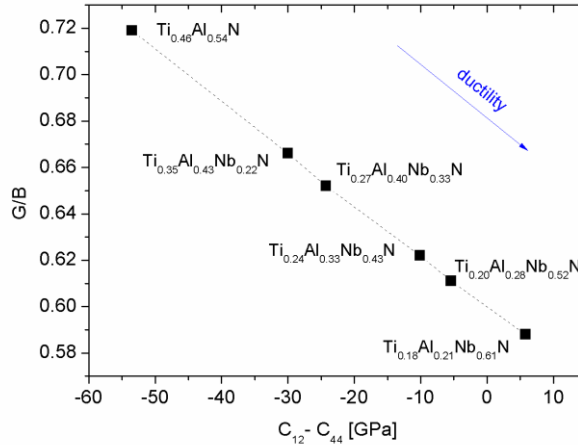


Fig. 4: Ductility trends in $Ti_{1-x-y}Al_xNb_yN$ plotted according to Pettifor and Pugh criteria.

CONCLUSION

Here, we show age hardening via spinodal mechanism in $Ta_{0.55}Al_{0.45}N$ coatings. Formation of fine-textured structure consisting of subgrains of diameter in the range of 30-60 nm during decomposition of TaAlN solid solution led to significant increase in hardness from ~ 29.6 to ~ 35.2 GPa observed in the coatings annealed at $1000^\circ C$. All as-deposited $Ti_{1-x-y}Al_xNb_yN$ coatings exhibited single phase cubic sodium chloride (B1) structure identified as TiAl(Nb)N solid solutions. The highest hardness, ~ 32.5 GPa, and the highest Young's modulus, ~ 442 GPa, were obtained in Nb-free $Ti_{0.46}Al_{0.54}N$. Increasing the Nb content results in a slight reduction of hardness, in the range from ~ 27.9 to ~ 31.1 GPa accompanied by a significant reduction of Young's moduli, which decreases by up to -20% (from ~ 442 to ~ 358 GPa), suggesting enhanced plasticity for in the highly NbN-alloyed coatings.

ACKNOWLEDGMENT

This work was supported by the Slovak Research and Development Agency [grant number APVV-14-0173], Operational Program Research and Development [project ITMS: 26210120010 and ITMS 26240220084].

REFERENCES

- [1] M. Mikula et al., Acta Materialia 121 (2016) 59-67.
- [2] P.H.Mayrhofer, et al., Self-organized nanostructures in the Ti-Al-N system, Applied Physics Letters (2003) 83 10 2049-2051.
- [3] D. Holec, L. Zhou, R. Rachbauer, P.H. Mayrhofer, Alloying-related trends from first principles: An application to the Ti-Al-X-N system, J. Appl. Phys. 113 (2013) 113510.
- [4] D.G. Sangiovanni, V. Chirita, L. Hultman, Toughness enhancement in TiAlN-based quaternary alloys, Thin Solid Films, 520 (2012) 4080.

Nové sklené a sklo-keramické materiály na báze hlinitanov vzácnych zemín pre aplikácie v pc-WLED

New rare-earth aluminate-based glass and glass-ceramics materials for applications in pc-WLED

K. Haladejová¹, R. Klement¹, A. Prnová¹, D. Galusek¹

¹ *Vitrum Laugaricio – Joint Glass Centre of the IIC SAS, TnU AD and FChPT STU, Trenčín*

ABSTRACT

The glasses in the systems $Y_2O_3-Al_2O_3$ and $Y_2O_3-Al_2O_3-SiO_2$ were prepared by flame-spraying synthesis in the form of glass microspheres form precursor powder synthesized by sol-gel method. The glasses were doped with small amount of Ce^{3+} and Mn^{2+} ions. The prepared glasses exhibit low thermal stability. The only phase crystallizing from glasses up to $1200^\circ C$ is YAG ($Y_3Al_5O_{12}$). The glasses exhibit intensive emission in blue spectral region, while crystallized phosphors in green-orange spectral range. The co-doping by Mn^{2+} ions (Ce^{3+}/Mn^{2+}) improved the emission in the orange spectral region.

Keywords: luminescence, yttrium aluminium garnet, thermal properties, phosphors, pc-WLED

INTRODUCTION

Phosphor-converted white light emitting diodes (pc-WLEDs) are regarded as new and perspective lighting sources for the next generation. In 1996, Ce^{3+} -activated phosphors were invented for white light emitting LED with remarkable properties. The most of current pc-WLEDs utilise the yellow emitting $Y_3Al_5O_{12}:Ce^{3+}$ (YAG: Ce^{3+}) phosphor and blue InGaN LEDs [1]. However, YAG: Ce^{3+} phosphor has a deficient emission in red spectral region resulting in the pc-WLED devices with low colour rendering index ($R_a < 80$) and high colour temperature ($T_c > 7000$ K). To improve the red emission in current pc-WLED devices, a phosphor blend of YAG: Ce^{3+} and red emitting phosphor is generally applied [2]. On the other hand, the Ce^{3+} ion can also act as an excellent sensitizer, transferring a part of its energy to activator ions such as Mn^{2+} ion that in octahedral coordination emits orange-red light [3]. In generally, the Mn^{2+} ions in photoluminescence spectra exhibit a broad emission band in the green or orange-red spectral region depending on coordination environment around the Mn^{2+} centre; Mn^{2+} in tetrahedral coordination – green emission, in octahedral coordination – from orange to red emission. Due to the spin forbidden character of ${}^4T_1-{}^6A_1$ transition, the emission intensity of Mn^{2+} -doped phosphors is relatively weak under UV excitation. Thus, the Mn^{2+} emission can be realized efficiently by energy transfer from excited Ce^{3+} ions to Mn^{2+} centres and this mechanism plays an important role in the development of efficient phosphor materials [3, 4]. Recently, much effort has been made to develop phosphors using energy transfer from Ce^{3+} to Mn^{2+} . Controlling the dopant concentrations in the host causes the emitting colour to move from the blue/green to orange/red region. For example, by co-doping Ce^{3+} and Mn^{2+} into the YAG host, the colour hues can be varied from blue to red.

In the present work, we report on the preparation and characterization of single doped, Ce^{3+} , and co-doped, Ce^{3+}/Mn^{2+} , glasses and glass-ceramics phosphors in the system $Y_2O_3-Al_2O_3$ and $Y_2O_3-Al_2O_3-SiO_2$, respectively. The studied phosphors were prepared in the form of microspheres using the flame synthesis. The precursor powders were synthesised by sol-gel Pechini method [5] that ensures the good homogeneity and distribution of luminescence active centres in the host matrix. The prepared glasses were characterized by optical microscopy (OM) scanning electron microscopy (SEM), X-ray diffraction (XRD), high

temperature XRD (HT XRD) and differential scanning calorimetry (DSC) analysis. The glass-ceramics phosphors were subsequently prepared by controlled crystallization of glasses and their luminescence properties were studied in details.

EXPERIMENTAL

The starting (precursor) powder was prepared by modified Pechini method [5] and glass microspheres by flame synthesis as described previously [6]. The dried powder of glass microspheres was heat-treated in temperature calibrated tube furnace at selected temperatures from 880 to 1500 °C for 3-5h (heating rate 10°C/min) in an air atmosphere. Thereafter, the samples were reduced in N₂:H₂ (90:10 vol.%) atmosphere at selected temperature sufficiently low to prevent the further crystallization of the samples. The glass microspheres (sample denoted as Y40A60Ce0.25) were prepared with following theoretical composition: 76.86 mol. % (59.94 wt. %) Al₂O₃ and 23.01 mol. % (39.74 wt. %) Y₂O₃. The doping level was 0.125 mol. % Ce₂O₃ corresponding to 0.25 at. % of Ce³⁺. The theoretical composition of the Ce³⁺/Mn²⁺ co-doped glasses is summarised in Tab. 1.

Table 1: The theoretical composition of the Ce³⁺/Mn²⁺ co-doped glasses (in mol. %).

SAMPLE	Y ₂ O ₃	Al ₂ O ₃	Ce ₂ O ₃	MnO, SiO ₂	Sum
A6Y4Ce0,25CC2AlMnSi0,5	23,108	76,517	0,125	0,125	100,000
A6Y4Ce0,25CC2AlMnSi1,0	23,108	76,267	0,125	0,250	100,000
A6Y4Ce0,25CC2AlMnSi1,5	23,108	76,017	0,125	0,375	100,000
A6Y4Ce0,25CC2AlMnSi2,0	23,108	75,767	0,125	0,500	100,000
A6Y4Ce0,25CC2AlMnSi2,5	23,108	75,517	0,125	0,625	100,000
A6Y4Ce0,25CC2AlMnSi3,0	23,108	75,267	0,125	0,750	100,000
A6Y4Ce0,25CC2AlMnSi3,5	23,108	75,017	0,125	0,875	100,000
A6Y4Ce0,25CC2AlMnSi4,0	23,108	74,767	0,125	1,000	100,000

The morphology of the samples was examined by optical microscopy (NIKON LV 100 UDM, Japan), scanning electron microscopy (SEM, JEOL JSM-7600 F/EDS/WDS/EBS, Japan). The DSC traces were recorded using Netzsch STA 449 F1 Jupiter (TG/DTA/DSC) at heating rate 10°C/min in the temperature range from room temperature to 1450 °C. The fluorescence spectra (excitation/emission) were recorded using Fluorolog FL3-21 spectrometer (Horiba). The 450 W xenon lamp was used as an excitation source. All spectra, except of excitation, presented herein were corrected for spectrometer response and lamp. The TCSPC (Time Correlated Single Photon Counting) technique was used to measure lifetime of photoactive species. The pulsed laser diodes (344 nm and 444 nm) with repetition rate of 1 MHz and pulse duration less than 200 ps was used as the pulsed pumping source.

RESULTS

The prepared glass microspheres with composition Y40A60Ce0.25 were found to be XRD amorphous within detection limit. The SEM however revealed regular features (faces) at the surface of some microspheres indicating that very little of them were at least partially crystalline.

The thermal properties of the sample Y40A60Ce0.25 were examined by DSC analysis. The DSC record of the glass microbeads is shown in Fig. 1. The T_g of studied glass (endothermic effect) was found to be in the range 875 – 901°C (875 °C onset, 893 °C inflection and 901 °C end of the endothermic effect). The characteristics of exothermic effects corresponding to crystallization of the sample Y40A60Ce0.25 are: $T_{x1} = 923$ °C, $T_{p1} = 936$ °C, $T_{x2} = 989$ °C and $T_{p2} = 1000$ °C, respectively. The origin of the two crystallization peaks (exothermic effect) was examined by high temperature XRD (HT XRD) that revealed the crystallization of

YAG phase ($Y_3Al_5O_{12}$) up to 1200 °C. The crystallization of α - Al_2O_3 phase was observed at temperatures above 1300 °C. This point to the fact, that both exothermic effects in DSC trace correspond to YAG phase crystallization; the first peak mainly to nucleation and partial crystallization of YAG phase, the second peak to crystal growth of YAG phase. The polycrystalline phosphors were prepared by controlled crystallization at selected temperatures (see Fig. 1). The crystallization time was adjusted according to the isothermal DSC experiments (not shown).

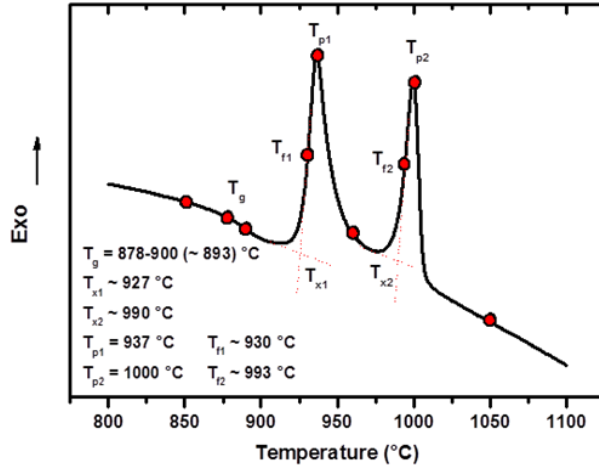


Fig. 1: DSC trace of as prepared glass microbeads with the composition Y40A60Ce0.25.

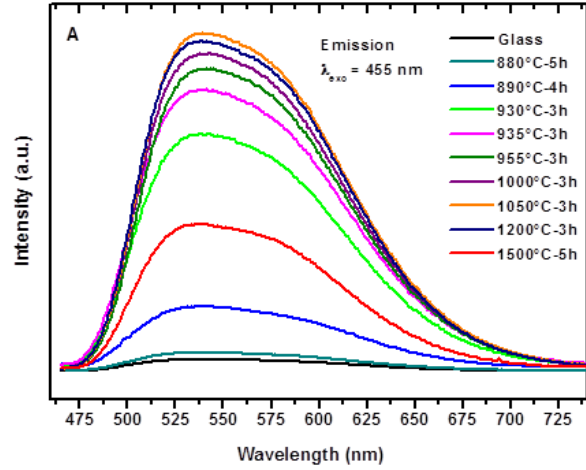


Fig. 2: PL emission spectra of crystallized glass microbeads Y40A60Ce0.25 treated at different temperatures.

The emission spectrum (not shown) of Ce^{3+} doped glass Y40A60Ce0.25 recorded under UV excitation at 345 nm exhibits intensive blue emission; broad emission band in spectral range of 365-500 nm with the emission maximum at 407 nm. This emission corresponds to the $5d \rightarrow {}^2F_{5/2}$ and $5d \rightarrow {}^2F_{7/2}$ transitions that are not clearly resolved. This is most likely due to the close energy of the 4f (${}^2F_{5/2}$, ${}^2F_{7/2}$) ground states of Ce^{3+} ions in the yttrium aluminate glass; Ce^{3+} with 4f¹ electron configuration has two mixed ground states of ${}^2F_{5/2}$ and ${}^2F_{7/2}$ due to the spin-orbital coupling. As temperature of the heat-treatment increases, the intensity of blue emission rapidly decreases, indicating that the Ce^{3+} ion is embedded into YAG crystal host.

The PL emission spectra ($\lambda_{exc} = 455$ nm) of samples heat-treated at different temperatures are depicted in Fig. 2. A typical broad emission band centred at ~ 550 nm is seen in spectra of all samples and PL emission intensity strongly depends on the treatment temperature. As the temperature increases from 880 °C to 1050 °C, the PL emission intensity significantly increases, reaching the maximum value at 1050 °C. The peak position, however, is only negligible affected by the heat-treatment. The increase of emission intensity with treatment temperature is due to the improvement of crystallinity of samples; more Ce^{3+} ions entering the YAG crystal lattice and can be efficiently excited. This was confirmed by XDR when apparent size of coherently diffracting domains increases with the heat treatment temperature. When temperature further increases, the PL intensity decreases as seen in Fig. 2, for sample treated at 1500 °C quite significantly. Such a decrease is most likely due to the oxidation of Ce^{3+} to Ce^{4+} during the heat treatment. Moreover, the enlarged average particles size and increased structural defects could cause luminescence quenching at defects as a consequence of higher probability of non-radiative transitions [7]. The lifetime of the excited state was found to be around 62 ns that is typical of Ce^{3+} in the YAG host.

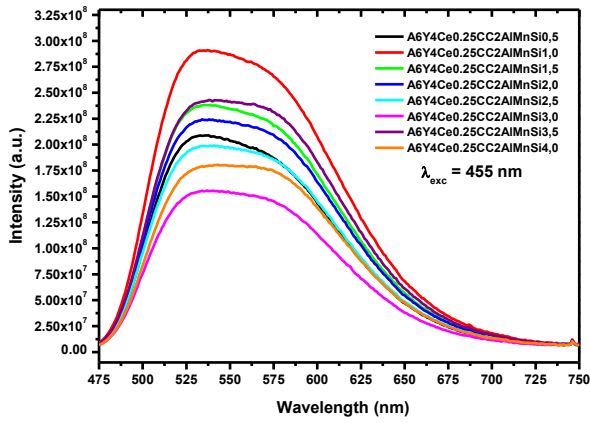


Fig. 3: Emission spectra of $\text{Ce}^{3+}/\text{Mn}^{2+}$ co-doped systems $\text{A6Y4Ce0,25CC2AlMnSi}_X$ crystallized at $1200^\circ\text{C}/4\text{ h}$ and reduced at $750^\circ\text{C}/8\text{ h}$, excited at 455 nm .

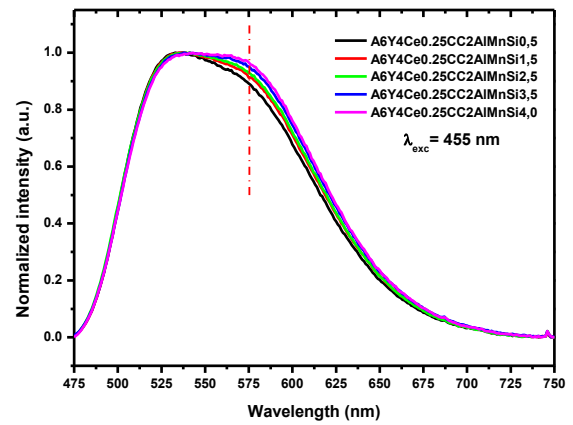


Fig. 4: Normalized emission spectra of $\text{Ce}^{3+}/\text{Mn}^{2+}$ co-doped systems $\text{A6Y4Ce0,25CC2AlMnSi}_X$.

The $\text{Ce}^{3+}/\text{Mn}^{2+}$ co-doped phosphors with different $\text{Ce}^{3+}/\text{Mn}^{2+}$ ratio were prepared by crystallization of corresponding glass at $1200^\circ\text{C}/4\text{h}$ and subsequently reduced in $\text{N}_2:\text{H}_2$ (90:10 vol.%) atmosphere at $750^\circ\text{C}/8\text{h}$. The corresponding glasses, similarly to the glass Y40A60Ce0.25 , exhibit intensive blue emission under UV excitation at 340 nm . The emission spectra of crystallized phosphors are shown in Fig. 3 and 4. The spectra exhibits asymmetric emission characteristic for Ce^{3+} ions that is due to the convolution of two transitions $5d_1 \rightarrow {}^2\text{F}_{5/2}$, ${}^2\text{F}_{7/2}$. In comparison to Y40A60Ce0.25 system, the intensity of the shoulder at $\sim 575\text{ nm}$ (orange emission of Mn^{2+} in octahedral coordination) increases with the increase of Mn^{2+} concentration in the samples indicating better emission in the orange-red spectral region. On the other hand, the Ce^{3+} emission significantly decreases with Mn^{2+} concentration, that is due to the energy transfer (ET) between Ce^{3+} and Mn^{2+} ions in the matrix. Decreasing lifetime of co-doped samples ($\sim 50\text{-}56\text{ ns}$) compared to single Ce^{3+} -doped samples ($\sim 62\text{ ns}$) also confirm $\text{Ce}^{3+} \rightarrow \text{Mn}^{2+}$ energy transfer with efficiency about 15 %. The low value of ET is related to the quite low concentration of Ce^{3+} and Mn^{2+} in the matrix and thus a larger distance between the ions. This distance is critical for the resonant ET mechanism.

CONCLUSION

The Ce^{3+} doped $\text{Ce}^{3+}/\text{Mn}^{2+}$ co-doped glasses and glass-ceramic materials were successfully prepared by flame-straying technique. The thermal analysis in combination with HT XRD revealed the crystallization of YAG phase in two distinct steps. The glasses exhibit intensive emission in blue spectral region, while crystallized phosphors in green-orange spectral range. The co-doping by Mn^{2+} ions improved the emission in the orange spectral region. The energy transfer between Ce^{3+} and Mn^{2+} ions in the host matrix was found to be at the level of about 15 %. The low value of ET is related to the quite low concentration of Ce^{3+} and Mn^{2+} in the matrix and thus a larger distance between the ions.

ACKNOWLEDGMENT

The financial support of this work by the projects SAS-NSC JRP 2015/16 and VEGA 1/0631/14, is gratefully acknowledged. This publication was created in the frame of the project "Centre of excellence for ceramics, glass, and silicate materials" ITMS code 262 201 20056, based on the Operational Program Research and Development funded from the European Regional Development Fund.

REFERENCES

- [1] Yongfu L., Xia Z., Zhendong H., Xiaojun W. and Jiahua Z., ChemComm., 2011,47, 4753.
- [2] Zhang X. and Gong M., Mater. Lett., 2011, 65, 1756.
- [3] Lu W., Jia Y. C., Lv W. Z., Zhao Q. and You H. P., New J. Chem., 2013, 37, 3701.
- [4] Dongxu W., Ying S., Lianzhou J., Shaoxin H. and Dan L., New J. Chem., 39, 2015, 4753.
- [5] Pechini, M.P., "Method of Preparing Lead and Alkaline-Earth Titanates and Niobates and Coating Method Using the Same to Form a Capacitor," U.S. Pat. No. 3 330 697, July 11, 1967.
- [6] Prnová A., Bodišová K., Klement R., Migát M., Veteška P., Škrátek M., Bruneel E., Van Driessche I., Galusek D., Ceramics International, 2013, 40, 6179.
- [7] George N.C., Pell A.J., Dantelle G., Page K., Llobet A., Balasubramanian M., Pintacuda G., Chmelka B.F., Seshadri R., Chem. Mater. 2013, 25, 3979.

Magnetické vlastnosti hlinitanových sklených mikrogulôčok s gelenitovou maticou

Magnetic properties of aluminate glass microspheres with gehlenite matrix

M. Majerová¹, A. Prnová², M. Škrátek¹, A. Dvurečenskij¹, J. Kraxner², M. Parchovianský²,
A. Cigán¹, J. Maňka¹, D. Galusek²

¹ Ústav merania, Slovenská akadémia vied, Dúbravská cesta 9, 842 19 Bratislava

² Vitrum Laugaricio, Centrum kompetencie skla, Spoločné pracovisko ÚACh SAV, TnU AD a FChPT STU, Študentská 2, 911 50 Trenčín

ABSTRACT

A flame-spraying technique was applied for preparation of aluminate glass microspheres with gehlenite matrix. In the first step, the precursor powder was prepared from a stoichiometric mixture of CaCO_3 , Al_2O_3 , SiO_2 by a standard solid-state reaction method. The glass was prepared in the form of microspheres by melting precursor powder in $\text{CH}_4\text{-O}_2$ flame, and by quenching micro-droplets of the melt by spraying them with deionized water. The structural and magnetic properties were studied by SEM, XRD and QD SQUID magnetometer. The gehlenite microspheres show complex magnetic behaviour that is function of temperature and the magnetic field, e.g. diamagnetic behaviour at 300 K, whereas paramagnetic properties at 2 K.

Keywords: gehlenite, flame-spraying synthesis, glass microspheres, magnetic properties

INTRODUCTION

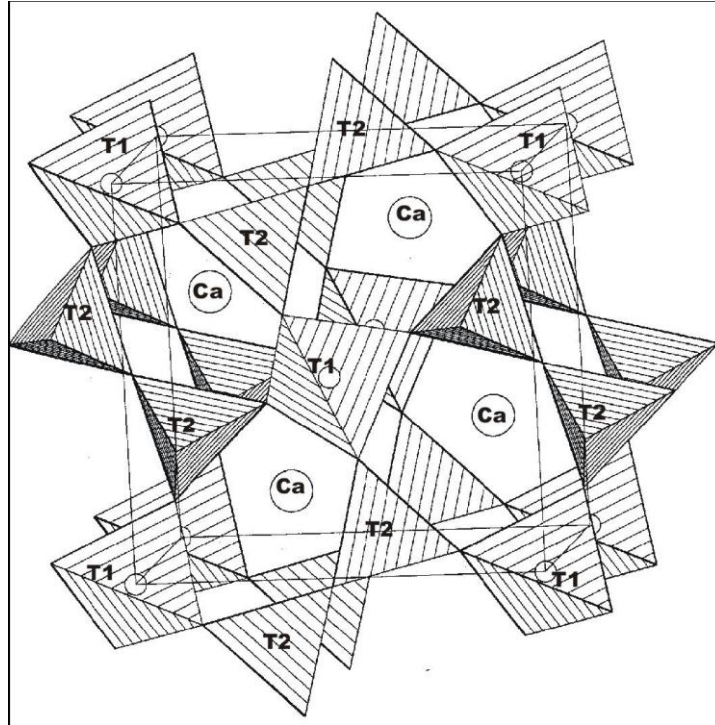
Sklá vykazujú zaujímavé magnetické vlastnosti. Práce, ktoré sa zaoberajú magnetickými vlastnosťami skiel obvykle, popisujú sklá, ktoré väčšinou obsahujú určité množstvo kovových prvkov [1, 2]. Sklá obsahujúce oxidy ťažkých kovov, ako je Bi_2O_3 a PbO , sa intenzívne skúmajú vzhľadom na ich jedinečné vlastnosti, ako je vysoká hustota, vysoký index lomu, priepustnosť pre infračervené žiarenie a vysokú polarizovateľnosť. Veľká pozornosť sa venuje magnetickým vlastnostiam amorfných oxidov v dôsledku pozorovania feromagnetického správania týchto oxidov [3]. Kovové sklá na báze Fe sú zaujímavé kvôli vynikajúcim mechanickým vlastnostiam. Sú to magneticky mäkké materiály s výbornou odolnosťou proti korózii a nízkym výrobným nákladom [4 - 8]. V posledných desaťročiach naberá na intenzite aj výskum binárnych a ternárnych skiel dopovaných iónmi vzácnych zemín, s perspektívami pre širokú škálu technologických aplikácií. Modifikácia štruktúrnych, magnetických a optických vlastností skiel obsahujúcich ióny vzácnych zemín prídavkom nanočastíc je novým trendom vo výskume skiel [9].

Z hľadiska magnetických vlastností bola doteraz relatívne malá pozornosť venovaná hlinitanovým sklám. V oblasti hlinitanových skiel sa študovali najmä hlinitano-kremičitanové sklá s prídavkom rôznych kovov (Co, Mn, Fe), pričom sa ukazuje, že sa jedná o spinové sklá [10 -13].

Gehlenit ($2\text{CaO}.\text{Al}_2\text{O}_3.\text{SiO}_2$) sa podrobne skúmal najmä v posledných desaťročiach, pretože je, vďaka svojej vysokej fyzikálnej a chemickej stabilite, vhodným hosťiteľom pre opticky aktívne dopanty.

V štruktúre gehlenitu sú katióny lokalizované na troch typoch miest: na osemnásobne koordinovaných miestach nazývaných Thomsonova kocka obsadených Ca^{2+} iónmi, v pravidelných tetraédroch (T1) plne obsadených Al^{3+} iónmi a v neusporiadaných tetraédroch (T2), kde sú Si^{4+} a Al^{3+} ióny náhodne (štatisticky) rozdelené [14].

Podľa našich vedomostí doteraz neboli namerané magnetické vlastnosti skiel so zložením identickým so zložením kryštalického gehlenitu. V práci Nöllera a Knolla sú popísané magnetické vlastnosti kryštalického diopsidu a gehlenitu dopovaného železom. Magnetické vlastnosti namerané pri nízkych teplotách pripisujú tetragonálnemu usporiadaniu v štruktúre gehlenitu [15].



Obr. 1: Štruktúra gehlenitu [16].

Predložená práca sa zaoberá prípravou hlinitanových skiel so zložením identickým so zložením kryštalického gehlenitu a následnou analýzou štruktúry a magnetických vlastností.

EXPERIMENTAL

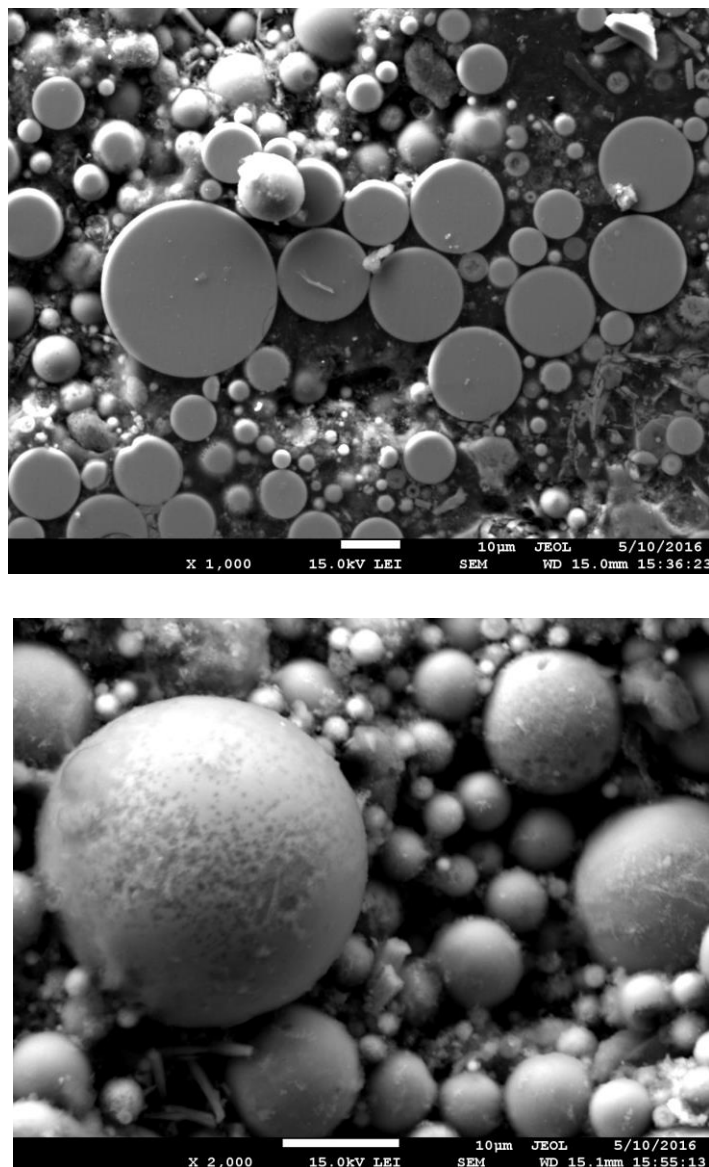
V prvom kroku sa z vysokočistých práškov CaCO_3 (p.a., Centralchem, Bratislava), Al_2O_3 (p.a., Centralchem, Bratislava) a SiO_2 (p.a., Polske odczynniki chemiczne, Gliwice) reakciou v tuhej fáze pripravili práškové prekurzory. Východiskové prášky vo vhodnom množstve sa navázili a homogenizovali v achátovom mlyne v izopropylalkohole a následne sušili pod IČ lampou. Po homogenizácii nasledovala kalcinácia pri $650^\circ\text{C}/4\text{h}$ v žiľiacich téglíkoch. Ďalším krokom bolo predreagovanie práškov v Pt téglíku po dobu 4 h pri 1000°C . Predreagované prášky boli znova pomleté a presitované cez $40\mu\text{m}$ polyetylénové sito. Sklené mikrogulôčky sa pripravili dávkovaním práškového prekurzora do $\text{CH}_4\text{-O}_2$ plameňa s teplotou okolo 2200°C , kde sa častice prášku roztavili. Kvôli dosiahnutiu vyššej chladiacej rýchlosti sa roztavené častice sprchovali jemne rozprášenou destilovanou vodou a odvádzali cez predchladič a chladič do zbernej nádoby. V zbernej nádobe sa častice sedimentovali potrebný čas a následne sa odseparovali. Po odseparovaní sa mikrogulôčky vyžihali v peci po dobu 1 h dobu pri teplote 650°C , aby došlo k odstráneniu prípadných organických nečistôt vzniknutých možným nedokonalým spaľovaním metánu.

Podrobné informácie o morfológii pripravených mikrogulôčok sa získali pomocou skenovacej elektrónovej mikroskopie (FEG SEM JEOL 7600f) pri urýchľovacom napätí 20kV. Sklené mikrogulôčky sa zalisovali do vodivej fenolickej živice (PhenoCure Resin Powder black) a vzorka sa opatrne preleštila na leštičke Buehler Ecomet 300/Automat 300 s použitím diamantových kotúčov, čím vznikli priečne rezy jednotlivých mikrogulôčok. Na

stanovenie fázového zloženia práškových prekursorov ako aj sklených mikrogulôčok sa použila RTG difrakčná prášková analýza. Na meranie sa použil difraktometer Panalytical Empyrean (Panalytical, Eindhoven, Holandsko) s Cu katódou s vlnovou dĺžkou RTG žiarenia $\lambda = 1,5405\text{\AA}$ v rozsahu 2θ uhlov $10\text{--}80^\circ$. Difrakčné záznamy sa vyhodnotili pomocou programu HighScore Plus s použitím databázy COD (Crystallographic Open Database). Magnetické vlastnosti pripravených mikrogulôčok sa namerali pomocou SQUID magnetometra MPMS XL-7 firmy Quantum Design v teplotnom rozsahu $2\text{--}300\text{ K}$.

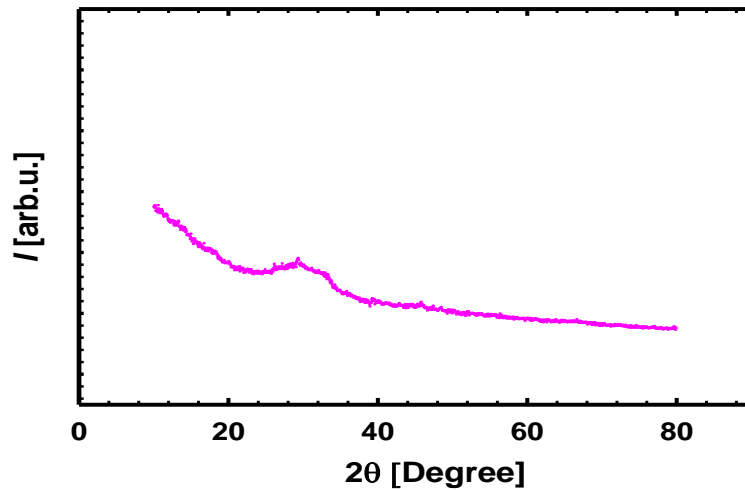
RESULTS

Detailný pohľad na morfológiu pripravených sklených mikrogulôčok poskytla elektrónová mikroskopia (Obr. 2). Vo vzorke sú pozorované okrem nepretavených alebo čiastočne natavených častíc aj čiastočne, resp. úplne skryštalizované častice.



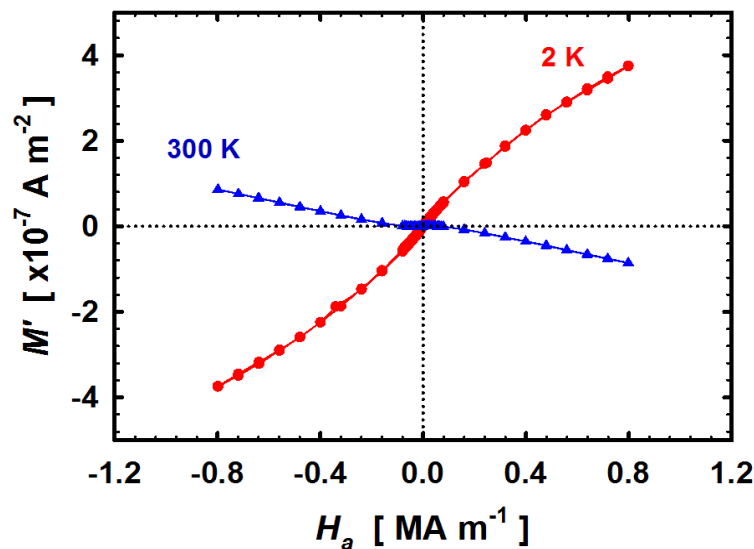
Obr. 2: SEM snímky gelenitových mikrogulôčok.

RTG difraktogram (Obr. 3) pripravenej vzorky potvrdil amorfný charakter pripravených mikrogulôčok, len s náznakmi difrakčných maxim, ktoré je možné pripísať prítomnosti kryštalickej fázy Ca_2SiO_4 v množstvách na hranici detekčného limitu RTG difrakcie.

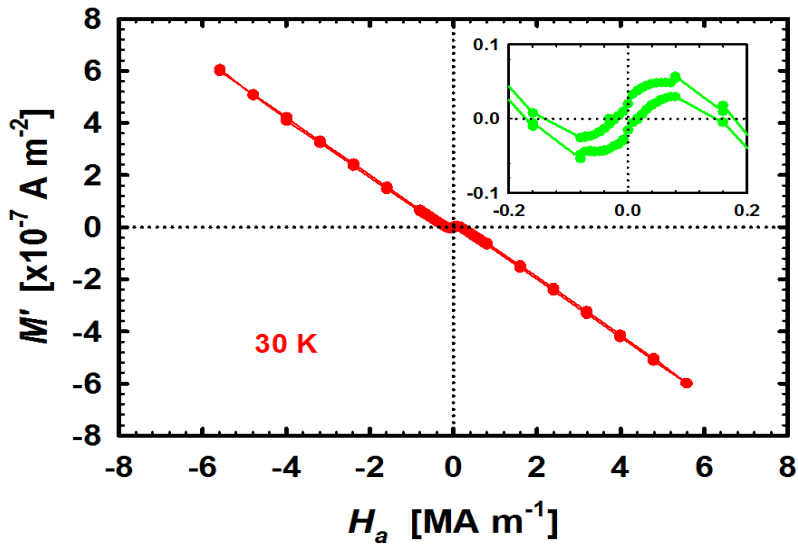


Obr. 3: RTG difrakčný záznam pripravených mikrogulôčok.

Závislosť magnetického momentu M' od aplikovaného magnetického poľa pri teplotách 300K a 2K je znázornená na Obr. 4. Ani jedna z kriviek nevykazuje hysteréziu

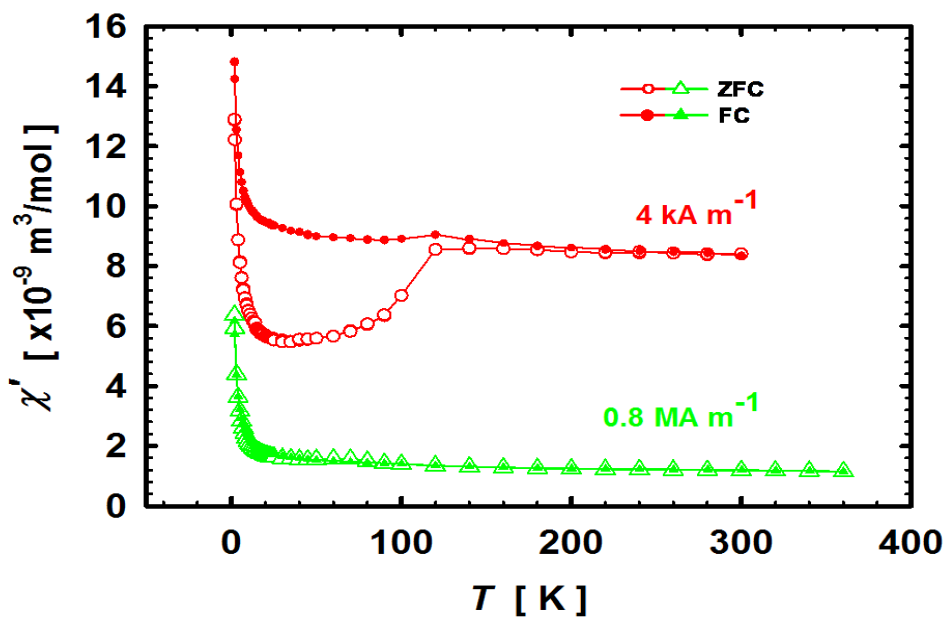
Obr. 4: Závislosť magnetického momentu M' od aplikovaného magnetického poľa H_a pri 300K a pri 2K.

Na Obr. 5) je znázornená závislosť magnetického momentu M' od aplikovaného magnetického poľa pri 30K. Pri vyšších hodnotách aplikovaného magnetického poľa prevláda diamagnetické správanie. Pre magnetické pole v blízkosti nuly možno pozorovať paramagnetický príspevok so slabou hysteréziou.



Obr. 5: závislosť magnetického momentu M' od aplikovaného magnetického poľa H_a pri 30K.

Teplotné závislosti ZFC (Zero Field Cooled) a FC (Field Cooled) molárnej magnetickej susceptibility sú uvedené na Obr. 6.



Obr. 6: Teplotné závislosti ZFC a FC molárnej magnetickej susceptibility χ' .

Pri aplikovanom magnetickom poli 4 kA m^{-1} je vidno rozdelenie kriviek ZFC a FC, ktoré indikuje superparamagnetizmus alebo aj vlastnosti spinových skiel (spin glass). Aplikovaním silnejšieho magnetického poľa 0.8 MA m^{-1} sa rozdelenie kriviek ZFC a FC potlačí a taktiež dochádza k zoslabeniu magnetickej susceptibility. Okrem toho, ZFC a FC krivky vykazujú slabú teplotnú závislosť pri vysokých teplotách, čo naznačuje prítomnosť teplotne nezávislého príspevku χ' .

Z nameraných závislostí boli pomocou Currie-Wiess zákona ($\chi = C/(T - \Theta)$, kde χ je magnetická susceptibilita, C je Curieho konštanta, T je teplota a Θ je Weissova teplota) určené prislúchajúce Weiss-ove teploty pre teplotné rozsahy 120 – 220 K a 1,8 – 15 K. Vo vysokoteplotnom rozsahu sú prislúchajúce hodnoty Weiss-ovej teploty Θ^a 100 K a 65 K pre magnetické polia 4 kAm^{-1} a 0.8 MA m^{-1} . V nízokoteplotnom rozsahu sú hodnoty Θ^b záporné a

to -1,9 K a -1,01 K. Zmena znamienka Weiss-ovej teploty v závislosti od teplotného rozsahu indikuje zmenu magnetického usporiadania z feromagnetika na antiferomagnetikum so znižujúcou sa teplotou.

CONCLUSION

V práci boli pripravené sklené mikrogulôčky so složením identickým so zložením kryštalického gehlenitu. Práškový prekursor pripravený reakciou v tuhej fáze sa použil na prípravu sklených mikrogulôčok plameňovou syntézou. Pripravený systém vykazuje polydisperzný charakter - priemer pripravených mikrogulôčok sa pohybuje v intervale od niekoľkých jednotiek až do desiatok mikrometrov, sú však prítomné aj nepretavené alebo čiastočne natavené častice. Systém obsahuje aj podiel kryštalickej fázy na hranici detekčného limitu RTG difrakcie. Pripravené sklené mikrogulôčky vykazujú komplexné magnetické vlastnosti, ktoré závisia od teploty a od magnetického poľa. Magnetizácia pri 300 K poukazuje na diamagnetické a pri 2 K na paramagnetické správanie. Ďalej sa zistilo, že na ZFC a FC molárnu magnetickú susceptibilitu χ' má významný vplyv aplikované magnetické pole, čo môže byť pripísané prítomnosti pohyblivých nosičov náboja. S ohľadom na štruktúru gehlenitu, je možné predpokladať, že zdrojom pohyblivých nosičov náboja môžu byť v pravidelných tetraédroch (T1) umiestnené Al^{3+} katióny alebo O^{2-} anióny. Diamagnetické vlastnosti môžu byť spojené prítomnosťou neusporiadaných tetraédrov $(\text{Al,Si})\text{O}_4$.

ACKNOWLEDGMENT

Táto práca bola finančne podporená grantom VEGA 2/0152/13 a VEGA 2/0058/14 a Agentúrou Ministerstva školstva SR pre štrukturálne fondy EÚ, kód projektu 262 401 200 19 a 262 402 200 73.

LITERATÚRA

- [1] Chen, L., Dai Y., Journal of Non-Crystalline Solids 452 (2016) 45-49
- [2] Pavić, L., Graca, M. P. F., Skoko, Ž., Moguš-Milanković, A., Valente M. A., Journal American Ceramics Society, 97 [8] (2014) 2517-2524
- [3] Pelluri, S. R., Singh, R., Journal of magnetism and Magnetic Materials 418 (2016) 206-212
- [4] Si, J., Mei, J., Wang, R., Chen, X., Hui, X., Materials Letters 181 (2016) 282-284
- [5] Shen, T.D., Sun, B.R., Xin, S.W., Intermetallics 65 (2015) 111-116
- [6] Liu, Q., a kol., Journal of Non-Crystalline Solids 443 (2016) 108-111
- [7] Zhang, M., Li, J., Kong, F., Liu, J., Intermetallics 59 (2015) 18-22
- [8] Lesz, S., Babilas, R., Nabialek, M., Szota, M., Dośpiał, M., Nowosielski, R., Journal of Alloys and Compounds 509S (2011) S197-S201
- [9] Aziz, S. M., Sarah, M.R., Ghoshal, S.K., Journal of magnetism and Magnetic Materials 423 (2017) 98-105
- [10] Moran, T.J., Batra, N.K., Verhelst, R.A., de Graaf A.M., Physical Review B 11 (1975) 4436-4439
- [11] Ferré, J., Pommier, J., Renard, J.P., Knorr, K., Journal of Physical Chemistry, Solid. St. Phys., 13 (1980) 3697-711

- [12] Meert, A., Wenger, L.E., Journal of magnetism and Magnetic Materials 23 (1971) 165-172
- [13] Ito, A., Torikai, E., Yamauchi, H., Syono, Y., Journal of Physical Chemistry, Solid. St. Phys., 15 (1982) 2759-2765
- [14] Lejus, A.M., Pelletier-Allard, N., Pelletier, R., Vivien, D., Optical Materials 6 (1996) 129-137
- [15] Nöller, R., Knoll, H., Solid State Communications 47 (1983) 237-239
- [16] Proverbio, M., Dapiaggi, M., Artioli, G., Materials Science Forum 443-444 (2004) 401-406

Hollow amorphous and polycrystalline YAG microspheres by flame spraying method

J. Kraxner¹, J. Chovanec¹, K. Haladejová¹, A. Černá¹, I. Petříková¹, D. Galusek¹

¹ *Vitrum Laugaricio, Joint Glass Centre of the IIC SAS, TnU AD and FCHFT STU, Trenčín, 911 50, Slovak Republic*

ABSTRACT

Successful preparation of glassy and polycrystalline hollow microspheres 5-30 μm in diameter with the composition identical to yttrium-aluminum-garnet (YAG, $\text{Y}_3\text{Al}_5\text{O}_{12}$) is reported. Hollow glass microspheres (HGMs) were prepared by flame spheroidization process from powder precursor. Controlled crystallization of the product resulted in preparation of hollow polycrystalline microspheres (HPMs) with the average size of the YAG grains 540 ± 40 nm by controlled heating at 1200°C . The amorphous structures and crystallization behaviors of YAG HGMs were investigated by X-ray diffraction (XRD). Morphology and microstructure of the hollow glass and polycrystalline microspheres were observed by scanning electron microscopy (SEM).

Keywords: hollow microspheres, YAG, flame spheroidisation

INTRODUCTION

Hollow glass microspheres are a low cost but high performance material with a number of various applications. Apart from routine applications, such as fillers for polymer-based composites, paints, varnishes etc., they are also useful as supports for catalysts, hydrogen storage, thermal insulation material, or agents for cancer treatment [1, 2]. Yttrium-aluminum garnet has received much attention because of its high chemical stability and interesting physical properties. It is used as a laser host and a matrix for intensive phosphors [3, 4]. It is also a promising structural material for high temperature engineering for insulating or refractory coating because of its high chemical stability, low electrical conductivity and high creep resistance [5, 6].

Apart from these applications radioactive yttrium containing glass microspheres 20-30 μm in diameter are used for in situ radiotherapy liver cancer treatment. Recently, a new type of in situ radiation treatment has been tested, using $17\text{Y}_2\text{O}_3\text{-}19\text{Al}_2\text{O}_3\text{-}64\text{SiO}_2$ (mol%) glass microspheres prepared by conventional melt quenching method [7]. The ^{89}Y isotope in the glass is not radioactive but neutron bombardment activates it to form ^{90}Y , which is β -emitter with the half-life of 64.1 hours. Radioactive yttrium-containing resin microspheres 30-35 μm in diameter have been also used clinically to treat liver cancer in various countries [8]. However, preparation of the microspheres in glassy state using a conventional melt-quench method the Y_2O_3 content is limited to 17 mol.%. Moreover, the radioactivity of the microspheres decays significantly before use in cancer treatment because of its short half-life [9]. The development of chemically durable microspheres containing a higher Y_2O_3 content is therefore desirable. Recently, dense Y_2O_3 microspheres 20-30 μm in diameter with high chemical durability were prepared using a high frequency induction thermal plasma melting. It is however, feared that microspheres implanted into a tumor may accumulate in the dorsal blood vessels of patients due to their high density [10]. In this case, the use of YAG hollow microspheres with low overall density is a favourable option, both due to high Y_2O_3 content in this system (37.5 mol.%), and their low overall density.

EXPERIMENTAL

The precursor powders were prepared by mixing $\text{Al}(\text{NO}_3)_3 \cdot 9\text{H}_2\text{O}$ (p.a., Centralchem, Bratislava) dissolved in deionized water with yttrium nitrate prepared by dissolution of Y_2O_3 powder (Treibacher Industrie AG, Austria) in 65% HNO_3 in the Al/Y molar ratio identical to that in the yttrium-aluminium garnet $\text{Y}_3\text{Al}_5\text{O}_{12}$. Citric acid dissolved in deionized water and ethylenglycol were added to the solution and the mixture was heated in oil bath for 2 hours at 85-90°C. The dried product was calcined at 1000°C for 4 hours in air and sieved through a 42 μm analytical sieve.

The calcined powder was fed into an oxygen-methane (O_2/CH_4) torch with a vacuum powder feeder at a rate of 2 g/min using oxygen carrier gas. The spherical melt particles were formed in high temperature oxy-methane flame (estimated temperature 2800°C) and then quenched by spraying by distilled water to form hollow glass microspheres (HGMs). The HGMs were separated from distilled water by microfiltration through a ceramic filter with pore size < 0.3 μm .

The crystallization behavior of the HGMs was studied by high temperature X-ray diffraction (HT-XRD) using powder diffractometer Panalytical Empyrean ($\text{CuK}\alpha$ radiation, $\lambda = 1.5405 \text{ \AA}$) equipped with high temperature cell Anton Paar HTK16 with Pt heating strip. The sample was deposited directly on the heating strip and heated at $10^\circ\text{C}\cdot\text{min}^{-1}$ in the temperature interval 800-1200°C, recording one diffraction pattern in the 2θ range 24-56° every 5°C. Internal standard ($\alpha\text{-Al}_2\text{O}_3$, 17 wt%) was added to facilitate quantification of the data by Rietveld refinement, including the amount of residual glass in the course of crystallisation. The data were evaluated using the software HighScorePlus with the PDF4 database. Based on the results of the X-ray diffraction a temperature of heat treatment was determined for complete crystallization of the YAG microspheres.

The morphology and microstructure of the microspheres were examined by scanning electron microscopy (SEM JEOL 7600F). Approximately 1 mg of HGMs was fixed on a conductive carbon tape, coated with Au-Pd to prevent charging and examined by SEM. The microspheres were also embedded in a polymeric resin, polished cross sections were prepared by Ion Beam Cross Section Polisher (CP-polisher, JEOL), and after coating with Au-Pd the details on microstructure were obtained by SEM.

RESULTS

The representative SEM micrograph of microspheres is shown in Figure 1a. The microspheres had smooth surfaces indicating their amorphous nature and their size varied between 5-30 μm in diameter. The polished cross section showing spherical cavities inside the microspheres is shown in Fig. 1b. The voids are most likely created by bloating the melt droplets by carbon dioxide from burning-out the carbon residua in precursor powder during the flame synthesis. Further experiments relating the amount of residual carbon with the frequency of occurrence and size of the voids in microspheres are in progress.

Figure 2 shows X-ray diffraction pattern of the as-prepared microspheres, and phase development in the microspheres with temperature. The broad band in the 2θ range of 25-35° in diffraction pattern of the as-prepared microbeads indicates the fully amorphous state of the material after synthesis, which consists of glass of YAG garnet composition. The sharp diffraction maxima attributed to Pt originate from the heating strip. The diffraction maxima attributed to $\alpha\text{-Al}_2\text{O}_3$ originate from the deliberately added internal standard.

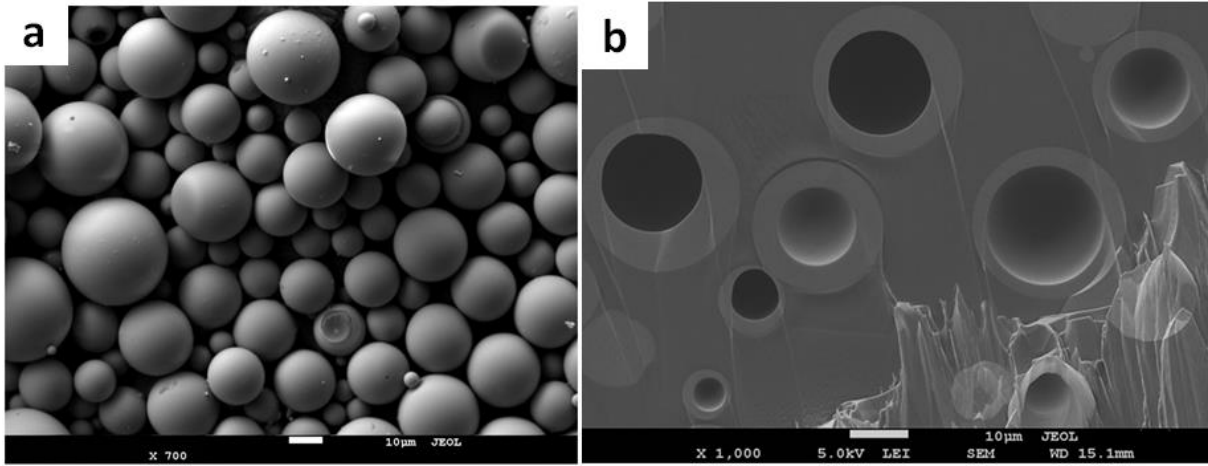


Figure 1: SEM image (a) of HGMs (b) ion beam polishing of HGMs.

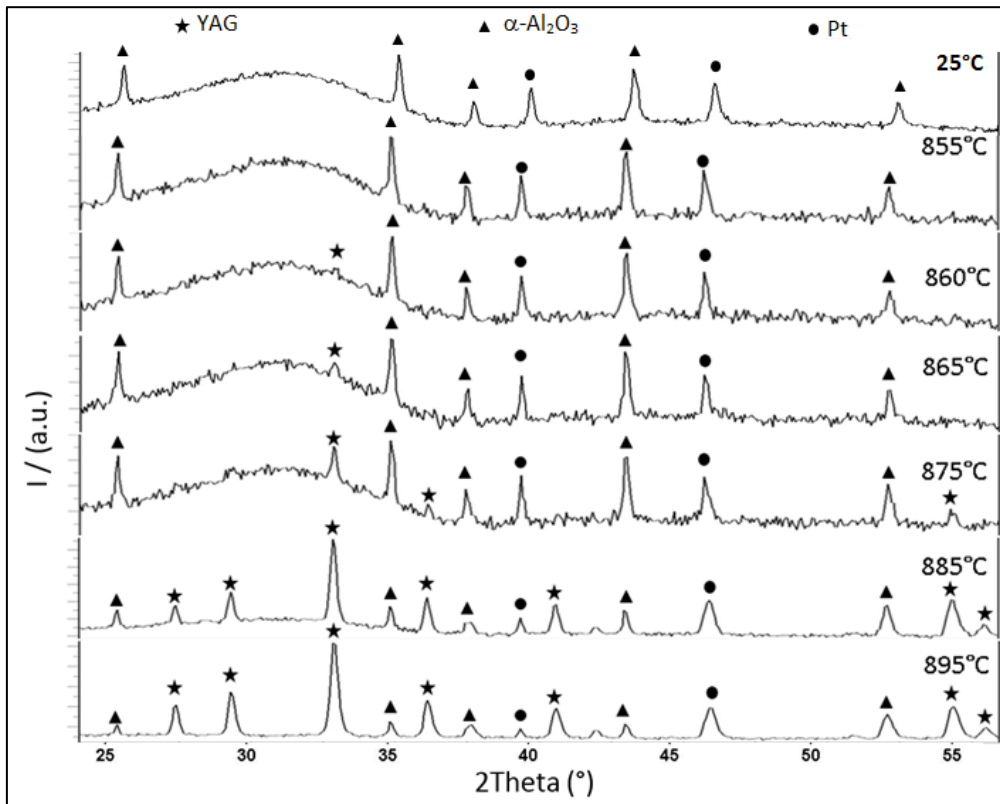


Figure 2: XRD patterns of the as-prepared microspheres, and the HT-XRD records of the microspheres at 25°C and in the temperature range 855-895°C.

Upon heating, the onset of formation of the YAG phase was detected at 860°C. Below this temperature no crystallization was observed. After that the YAG crystallization proceeded very fast and at 895°C the microspheres were fully crystalline, containing 100 % of YAG. Such fast crystallization is attributed to the structure of the YAG glass, which consist of only slightly distorted structural units identical to the structural units of crystalline YAG that require only slight re-arrangement to form polycrystalline material. Figure 3a shows the cavity inside a hollow microsphere after heat treatment at the maximum temperature of 1200°C. Figure 3b shows the detail of the microstructure. The micrographs suggest the hollow microspheres have dense walls consisting of submicron equiaxed YAG grains with an average size of $\sim 540 \pm 40$ nm.

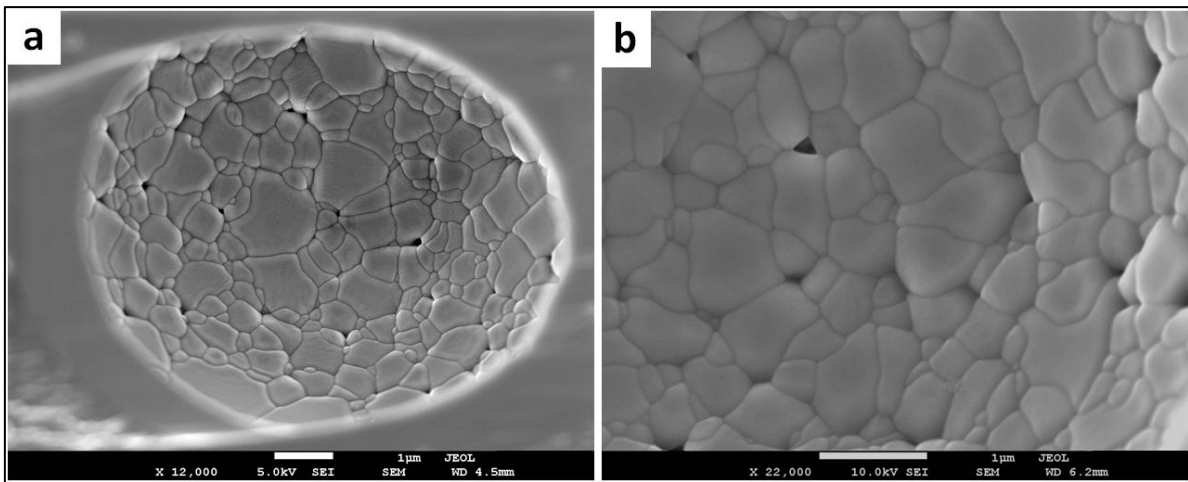


Figure 3: SEM micrograph of the cavity inside a heat-treated microsphere (a) and detail of its microstructure (b).

CONCLUSION

The work reports on successful preparation of hollow glass microspheres with the composition identical to that of crystalline YAG by flame spheroidization process in oxygen-methane (O_2/CH_4) flame. By controlled heating at $895^\circ C$ complete crystallization of the microspheres is achieved, with cubic $Y_3Al_5O_{12}$ as the only detected crystalline phase. Hollow polycrystalline microspheres with dense walls and submicron microstructure with the average size of the YAG grains 540 ± 40 nm were prepared by controlled heating at $1200^\circ C$.

ACKNOWLEDGMENT

The financial support by the grant VEGA 2/0058/14, and the SAS-MOST JRP 2015/6 is gratefully acknowledged. This publication was created in the frame of the project “Centre of excellence for ceramics, glass and silicate materials” ITMS code 262 201 20056, based on the Operational Program Research and Development funded from the European Regional Development Fund.

REFERENCES

- [1] Sridhar Dalai, Pragma Shrivastava, S. Vijayalakshmi and Pratibha Sharma, Adsorption of Nitrogen and Hydrogen on Hollow Glass Microspheres (HGMs), Energy and Environmental Engineering Journal, Volume 1, Issue2, September 2012.
- [2] Yan Hu, riguo Mei, Zhenguo An, Jingjie Zhang, Silicon rubber/hollow glass microspheres composites: Influence of broken hollow glass microsphere on mechanical and thermal insulation property, Composites Science and Technology 79, 2013.
- [3] Song Hu, Chunhua Lu et al., Transparent YAG:Ce ceramics for WLEDs with high CRI:Ce³⁺ concentration and sample thickness effects, Ceramics international 42, (2016.)
- [4] Koen Van den Eeckhout et al., Persistent Luminescence in Non-Eu²⁺ - Doped Compounds: A review, Materials 2013.
- [5] Minati Chatterjee, Milan Kanti Naskar, Synthesis of Yttrium-Aluminum-Garnet Hollow Microspheres by Reverse-Emulsion Technique, J.Am.Ceram.Soc., 89 (2006).
- [6] Gang He, Guanghua Liu, Shibin Guo, Zengschao Yang, Jiangtao Li, Crystallization of $Y_3Al_5O_{12}:Ce^{3+}$ glass microspheres prepared by flame-spraying synthesis, J Mater Sci: Mater Electron 2014.

- [7] Kurt E.Geckeler and Hiroyuki Nishide., Advanced Nanomaterials, Volume1, Nanoceramics for Medical Application, 2010.
- [8] M.R. Ghahramani, A.A. Garibov, T.N. Agayev, Production of yttrium aluminum silicate microspheres by gelation of an aqueous solution containing yttrium and aluminum ions in silicone oil, Int. J. Rad. Research, Vo.12, No.2, 2014.
- [9] M.R. Ghahramani, A.A. Garibov, T.N. Agayev, M.A. Mohammad, A Novel Way to Production Yttrium Glass Microspheres for Medical Applications, Glass Physics and Chemistry, Vol.40, No.3, 2014.
- [10] Masakazu Kawashita, Yoshihisa Takayama, Enzymatic Preparation of Hollow Yttrium Oxide Microspheres for In Situ Radiotherapy of Deep-Seated Cancer, J. Am. Ceram. Soc. 89, 4, 2006.

Elektrická modifikácia povrchu hydroxyapatitu na mikrourovni**Electrically modified surfaces of hydroxyapatite at microscale**

M. Truchlý¹, T. Plecenik¹, M. Gregor¹, M. Zahoran¹, G. Plesch², S.A.M. Tofail³, A. Plecenik¹

¹*Department of Experimental Physics, Faculty of mathematics, physics and informatics, Comenius University in Bratislava*

²*Department of Inorganic Chemistry, Faculty of natural sciences, Comenius University in Bratislava*

³*Materials and Surface Science Institute, University of Limerick, Limerick, Ireland*

ABSTRACT

Biomaterials are defined as synthetic materials which interact with biological systems. Usually are used as replacement or improvement of damaged part of living body. Manmade hydroxyapatite (HAp) is a hard ceramic biocompatible material used in orthopedic and dental surgery. The success of implant is strongly influenced by the biological response which can be improved by different physical methods. Among others, controlling of the adhesion and growth of bacteria, biological cells and biomolecules by adjusting wettability and surface potential modification has been proposed. In this work, surface potential has been modified by electron beam irradiation and mapped by Kelvin probe force microscopy.

Keywords: hydroxyapatite, Kelvin probe force microscopy, electron beam, surface potential

INTRODUCTION

Hydroxyapatite (HAp) – $\text{Ca}_{10}(\text{PO}_4)_6(\text{OH})_2$ – belongs to the group of hard biological materials. Synthetic HAp is an osteoconductive material used in dental and orthopedic surgery as a bulk implant or as a coating for effective adhesion of peptides, proteins, bacteria and strains [1]. To improve the biological response and adhesion, wettability and surface potential (SP) are modified. Several methods have been proposed. Among others, the electron irradiation method provides precise SP patterning and wettability modification [2]. Moreover, electrical modification of biomaterials helps to understand interactions between the biomaterial and bacteria, biomolecules or biological cells.

For a detailed investigation, a method providing imaging in the submicro-scale is necessary. The SP distribution can be studied by Kelvin Probe Force Microscopy (KPFM) which belongs to the group of Scanning Probe Microscopy (SPM) methods.

In this work, the SP modification of HAp thin films by focused electron beam typically available in Scanning Electron Microscopy (SEM) has been studied. By KPFM measurements, possibility of micro-meter sized negative and positive SP domains creation has been shown. The observed SP distribution is in a good agreement with the protein adsorption.

EXPERIMENTAL

The HAp thin films were prepared by a sol-gel synthesis route and subsequent spin-coating on silicon substrates. The electron-induced SP modification by the focused electron beam was done by SEM Tescan VEGA TS 5136 MM. A matrix of points has been irradiated with the incident electron energy in the range from 3 to 30 keV. The surface topography and SP of HAp coatings have been measured by SPM NTegra Aura (NT-MDT). Standard silicon and conductive TiN-coated AFM tips have been used.

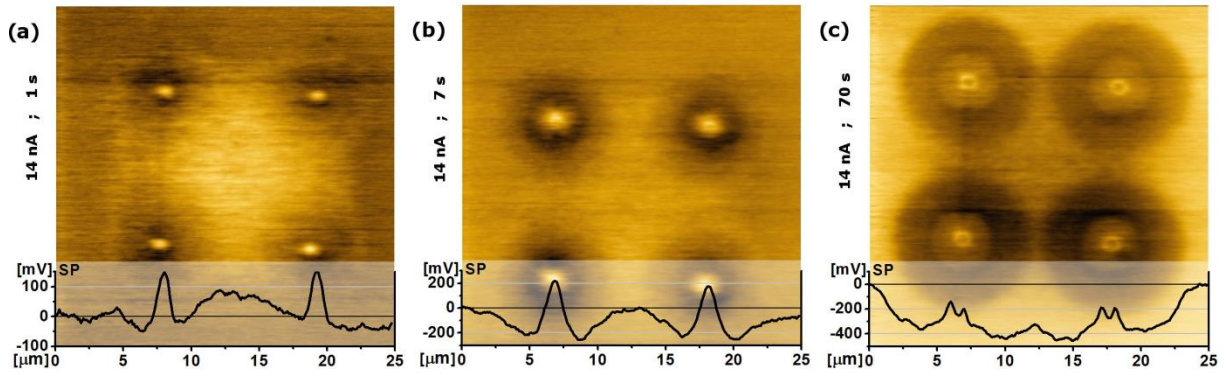


Fig.1: SP distribution of areas irradiated by focused electron beam. The injected charge dosage: (a) 14 nC; (b) 98 nC; (c) 980 nC.

RESULTS

The film thickness was about 330 nm. AFM surface analysis showed the nanocrystalline structure with average roughness less than 3 nm. No surface topography modification was observed after electron beam irradiation. Typical obtained SP patterns are shown in Fig.1. For all used energies and charge doses, circular domains of modified SP were observed. Resulting distribution is influenced by the roughness, porosity, structure and thickness of the HAp thin film, the electron beam current, the time of irradiation and the energy of the electron beam. Physical mechanisms affecting the size and the shape of the domains include: trapping of electrons and generating holes [3], emission of secondary electrons [4], surface contamination by carbon layer [3], spreading of the charge carriers due to local electric fields [5]. Moreover, pyroelectric and piezoelectric effect on unpoled HAp was confirmed [6].

As a probing protein to investigate adsorption onto irradiated HAp film, hen egg white Lysozyme was employed. Typical distribution of the adsorbed lysozyme was observed by confocal microscopy (Fig.2a) Corresponding KPFM image with the SP distribution is shown in Fig.2b. Profile cross-section of single-domain comparison of both the protein adsorption and SP distribution is shown in Fig.2c. In general, the adsorption of the positively charged LSZ is favored onto the negatively charged areas (the areas with lower SP) and follows the SP distribution according to the expectations.

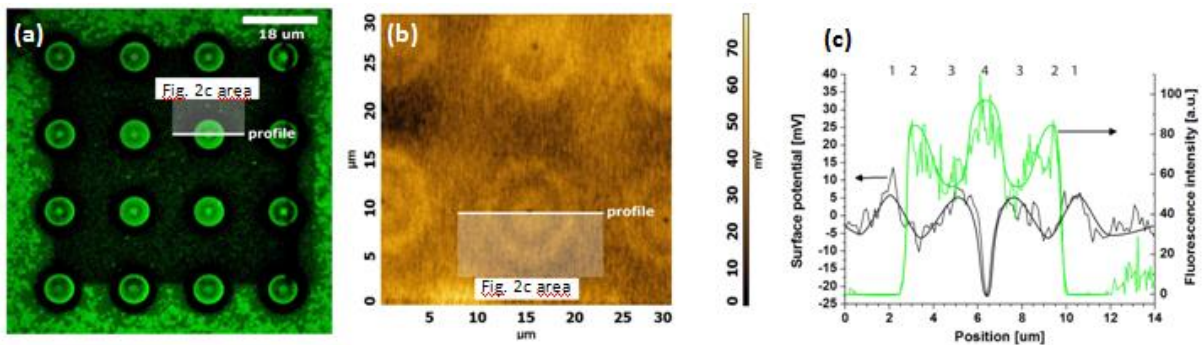


Fig. 2: (a) Protein distribution measured by scanning laser confocal microscopy; (b) Relative surface potential distribution measured by KPFM; (c) Profile of the SP distribution and protein adhesion in a domain cross-section.

CONCLUSION

To conclude, the SP modification by focused electron beam on micro-scale has been demonstrated. Micro-domains with both positive and negative SP have been prepared on HAp

thin films. The adsorption of proteins can be adjusted on at least micro-meter scale. Distribution of the adsorbed proteins is in a good agreement with the observed SP distribution. Presented finding may have practical application where adsorption of specific proteins needs to be adjusted.

ACKNOWLEDGMENT

This work was supported by the Slovak Research and Development Agency [grant number APVV-14-0173], Operational Program Research and Development [project ITMS: 26210120010].

REFERENCES

- [1] J.Y. Wong and J.D. Bronzino, *Biomaterials*, CRC Press Taylor & Francis Group, 2007.
- [2] Y.H. An and R.J. Friedman, *Concise review of mechanisms of bacterial adhesion to biomaterial surfaces*, J. Biomed. Res. 43, 338-348 (1998).
- [3] D. Aronov, R. Rosen, E.Z. Ron, G. Rosenman, Electron-induced surface modification of hydroxyapatite-coated implant, *Surf. Coat. Technol.* 202 (2008) 2093.
- [4] R.Gerhard-Multhaup, Electrets: dielectrics with quasi-permanent charge or polarization, *IEEE Trans. Electr. Insul.* EI-22 (1987) 531.
- [5] P. Molina et al., Effect of electron beam writing parameters for ferroelectric domain structuring LiNbO₃:Nd³⁺, *Opt. Mater.* 31(2009) 1777.
- [6] S.B. Lang, S.A.M. Tofail, A.A. Gandhi, et al., Pyroelectric, piezoelectric, and photoeffects in hydroxyapatite thin films on silicon, *Appl. Phys. Lett.* 98 (2011) 123703.

Korózia a nízokteplotná degradácia dentálnej keramiky na báze ZrO₂

Corrosion and low temperature degradation of zirconia based dental ceramics

S. Mikušínek¹, D. Galusková¹, A. Nowicka¹, D. Galusek¹

¹*Vitrum Laugaricio – Joint Glass Center of the Institute of Inorganic Chemistry, SAS, Alexander Dubček University of Trenčín and Faculty of Chemical and Food Technology, Slovak University of Technology, Študentská 2, 911 50 Trenčín*

ABSTRACT

Corrosion and low temperature degradation (LTD), as well as the temperature cycling in the presence of an acid corrosive media can significantly reduce the strength of yttria stabilized zirconia (Y-TZP) ceramics and affect the durability and lifetime of dental implants and replacements prepared from this material. The effect of long term exposure of commercial yttria stabilized zirconia (3Y-TZP) dental materials IPS e.max[®] ZirCAD (Ivoclar Vivadent AG, Liechtenstein) to acidic medium, and corrosion induced migration of yttria as a stabilizing element on its LTD, which results in transformation of the tetragonal ZrO₂ to monoclinic, was evaluated. The phase transformation was accompanied by a volume increase in the ZrO₂ grains with potential negative impact on surface mechanical properties, shortening of useful lifetime, and the possibility of catastrophic failure of the dental material.

Keywords: corrosion, low temperature degradation, dental implants, acetic acid, accelerated aging test

INTRODUCTION

Dental implants are used to replace missing teeth. The gray color of metal implants, and titanium alloys in particular represents an aesthetic problem. In exceptional cases metals (including Ti) cause hypersensitivity or allergic reactions. Some patients require non-metallic dental materials, in particular implants made of ceramic materials, which have been gradually growing in popularity. However, in order to achieve clinical and commercial success, sufficient strength, long-term stability and good integration into the jaw bone is required. Among the ceramic materials 3Y-TZP bio ceramics (tetragonal ZrO₂, stabilized by the addition of 3 mol. % yttria) occupies an important place. This material is often considered as an alternative to biomedical grade titanium. This ceramic has excellent mechanical strength, excellent biocompatibility and exhibits osseointegration comparable to the Ti-based materials. There are more than 10 manufacturers worldwide who developed ZrO₂ based dental implants, each one with its own production process, design and surface finish designed to osseointegration. It is known that rough surfaces enhance osseointegration and improve mechanical anchoring of implant to the bone [1]. For improved mechanical properties and a controlled microstructure, sintering additives as CuO, MnO, MgO and especially Al₂O₃ have been added to Y-TZP material for preparation high density materials with fine grain microstructure at lower temperatures.[2] Especially, the densification behavior of Al₂O₃ added to 3Y-TZP materials was examined in several works.[3, 4] CAD/CAM technologies have been introduced in the field of dental implants recently, significantly improving quality and accuracy of dentures.[5]

ZrO₂ has several modifications with different crystal structures. Tetragonal ZrO₂ is formed during sintering, by phase transformation from the monoclinic phase at 1170 °C. With suitable stabilizing additives (e.g. Y₂O₃) the tetragonal phase is retained even after cooling down to room temperature. Under suitable conditions the (t → m) phase transformation may be induced, accompanied by volume expansion up to 5 vol. %, with consequent formation of micro-cracks. A failure of dental implant may then result. Dental ZrO₂ ceramics is most often

stabilized by the addition of yttrium oxide (Y_2O_3), and the binary system Y_2O_3 - ZrO_2 is permitted by standards for surgical applications. [6-8]

Some published works show that in an aqueous medium Y_2O_3 reacts with water, yielding $Y(OH)_3$, and leading to gradual leaching of the stabilizer and subsequent transformation to monoclinic ZrO_2 . This process is called low-temperature degradation (LTD). [9] Chevalier et al. [10] suggest that destabilization leading to LTD is caused by oxygen anions O^{2-} from dissociation of water filling the free oxygen positions in the structure of zirconia. Another alternative is the cleavage of Zr-O-Zr bonds by the reaction with water to form zirconium hydroxide, resulting in corrosion of the material. [9, 11] Regardless of the mechanism of LTD, it is generally accepted that the $t \rightarrow m$ transformation starts from the surface of the sample and continues inwards. [8, 11]

This study aims to investigate the influence of the corrosive action of acidic media under conditions simulating the environment in the oral cavity to the corrosion of ZrO_2 based dental materials associated with leaching of stabilizing elements (Y) and the examination of the influence of corrosion on low temperature degradation of these materials under the conditions of the accelerated aging test (AAT).

EXPERIMENTAL

The corrosion tests were conducted under static conditions in the environment of 4 % acetic acid (pH=2.4). The dental implants were exposed to the corrosive medium at three different temperatures 37, 60, and 80 °C for 0.66, 7, 15, 35 and 60 days. Both the un-corroded specimens and the specimens corroded at 80 °C for 60 days were subjected to accelerated ageing tests (AAT) at 134 °C and a pressure of 200 kPa in water vapour in an autoclave, and the influence of corrosion on LTD was evaluated. The exposure times of 2, 5 and 10 hours were applied. The exposure of 1 hour under the conditions of AAT corresponds to 2 years in human body. The initial chemical composition of the tested dental material was determined by SEM-EDS (FEG SEM JEOL 7600f). Corroded surfaces, as well as the surfaces of dental ceramics after LTD tests, were characterized by SEM. The amounts of yttrium and zirconium released into corrosive media during the corrosion tests were determined by ICP-OES (Agilent 5100 SVDV). The changes of phase composition (the content of tetragonal vs monoclinic ZrO_2) was determined by X-ray powder diffraction (Panalytical Empyrean).

RESULTS

Corrosion of dental 3Y-TZP ceramics in the acid environment was associated with leaching of yttrium. The amounts of Y leached from the ceramics at various temperatures are shown in (Fig. 1.) The corrosion caused partial destabilization of t - ZrO_2 and measurable increase of the content of m - ZrO_2 (Fig. 2). Corrosion damage lead to increased susceptibility of the ceramics to LTD, reflected in markedly increased content of m - ZrO_2 after the accelerated ageing test in comparison to un-corroded material (Fig. 3). The SEM examination revealed surface damage in the form of corrosion pits of corroded material after AAT (Fig. 4).

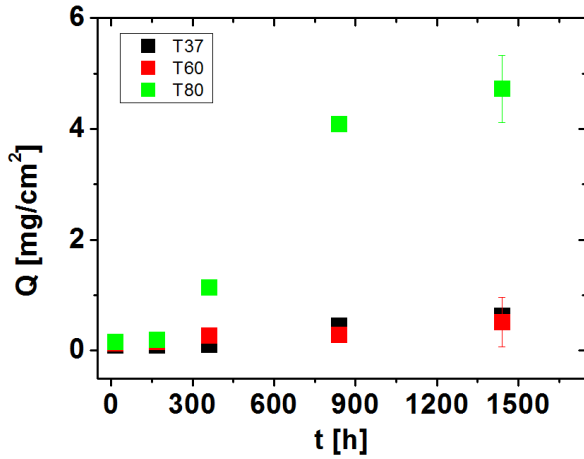


Fig. 1: Amounts of Y (expressed as weight of yttrium excluded to the corrosive solution per unit area – Q) from the 3Y-TZP ceramics at 37, 60 and 80 °C.

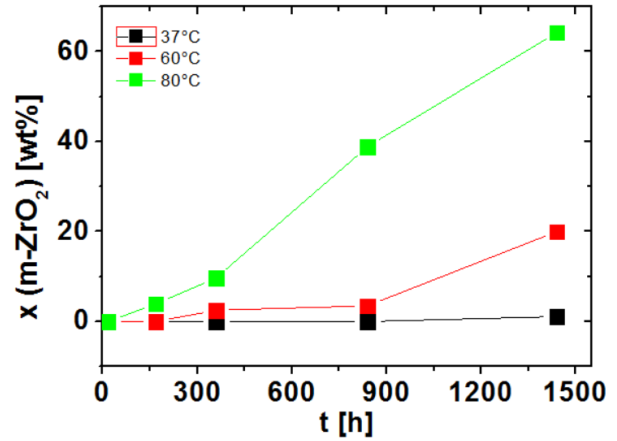


Fig. 2: Weight fraction of m-ZrO₂ in dental ceramics after exposure to acetic acid at 37, 60 and 80 °C.

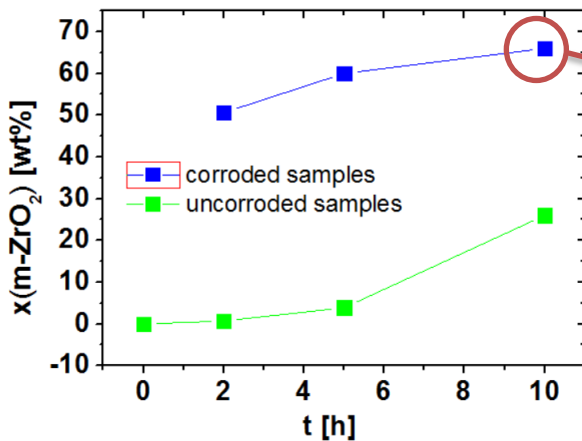


Fig. 3: Weight fraction of m-ZrO₂ in corroded and un-corroded dental ceramics after AAT.

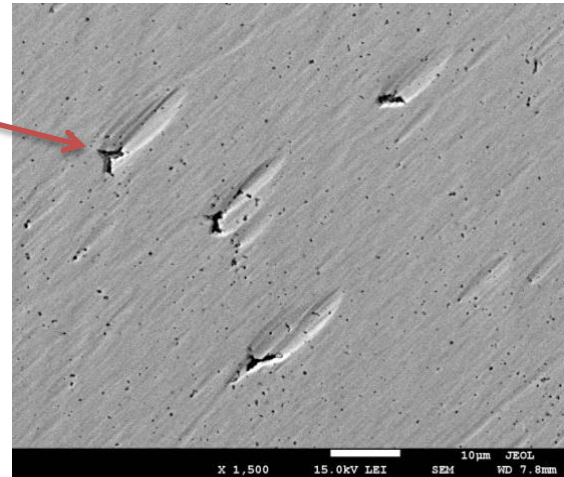


Fig. 4: Surface damage of corroded dental ceramics after AAT.

CONCLUSIONS

The results obtained in the work can be summarised as follows:

- The tested 3Y-TZP dental ceramic is vulnerable to low temperature hydrothermal degradation (LTD), a phenomenon in which, due to the presence of water, the t–m phase transformation is triggered at the ceramic surface.
- Acidic corrosion of 3Y-TZP dental ceramics is associated with leaching of yttrium from zirconia ceramics, resulting in partial destabilization of tetragonal zirconia and measurable increase of the content of monoclinic phase at the surface. This, in turn, results in increased susceptibility of the ceramics to low temperature degradation.
- Other potential negative impacts might include:
 - stress induced phase transformation under the stresses applied during chewing,

- decreased tolerance to surface damage and micro cracking, resulting in overall decrease of mechanical strength and wear resistance and hence, decreased life expectations for dental implants.

ACKNOWLEDGMENT

Financial support of this work by the JECS Trust Grant, contract No 201598, and the grant APVV 0218-11 is gratefully acknowledged. In this work were used the experimental facilities acquired through the project "Centre of excellence for ceramics, glass, and silicate materials" ITMS code 262 201 20056, based on the Operational Program Research and Development funded from the European Regional Development Fund.

REFERENCE

- [1] Sanonn C., Chevalier J., Douillard T., Cattani-Lorente M., S. Scherrer S., Gremillard L. A new testing protocol for zirconia dental implants, *Dental materials* 31, (2015) 15 – 25.
- [2] Yong Yang S., Joon-Hyung L., Jeong Joo K., Jai-Sung L. Sintering behavior of Y-doped ZrO_2 ceramics: the effect of Al_2O_3 and Nb_2O_5 addition, *Solid State Ionics* 172, (2004) 413-416.
- [3] Morales-Rodríguez A., Domínguez-Rodríguez A., de Portu G., Jiménez-Melendo G. Creep mechanisms of luminated alumina/zirconia-toughened alumina composites, *Journal of the European Ceramic Society* 29, (2009) 1625-1630.
- [4] Jiménez-Melendo M., Clauss C., Domínguez-Rodríguez A., de Portu G., Roncari E., Pinasco P. High temperature plastic deformation of multilayered YTZP/ZTA composites obtained by tape casting, *Acta mater.* Vol 46 No. 11, (1998), PII: S1359-6454(98)00066-4, 3995-4004.
- [5] Beuer F., Schweiger J., Edelhoff D. Digital dentistry: a overview of recent developments for CAD/CAM generated restorations, *British Dental Journal* 204, (2008) 505 – 511.
- [6] Chevalier J., Loh J., Gremillard L., Meille S., Adolfson E. Low-temperature degradation in zirconia with a porous surface, *Acta Biomaterialia* 7, (2011) 2986 -2993.
- [7] Gremillard L., Martin L., Zych L., Crosnier E., Chevalier J., Chrabouillot A., Sainsot P., Espinouse J., Aurelle J. – L. Combining ageing and wear to assess the durability of zirconia-based ceramics heads for total hip arthroplasty, *Acta Biomaterialia* 9, (2013) 7545 – 7555.
- [8] Enoiu C., Volceanov A., Volceanov E., Gavrilă R. Nanostructured zirconia composites stabilized with CeO_2 for biomedical applications, *Rom. Jour. Phys.* Vol. 49 Nos. 9-10 P. (2004) 777-787.
- [9] Vanni L., Valter S. Low temperature – ageing - of zirconia: A critical review of the relevant aspects in dentistry, *Dental materials* 26, (2010) 807 – 820.
- [10] Chevalier J., Gremillard L., Virkar AV., Clarke DR. To tetragonal-monoclinic transformation in zirconia: Lessons and learning future trends, *J. Am Ceram Soc.* 92, (2009) 1901-1920.
- [11] Cattani Lorente M., S. Scherrer S., Ammann P., Jobin M., Anselm Wiskott W. H. Low temperature degradation of a Y-TZP dental ceramic, *Acta Biomaterialia* 7, (2011) 858 – 866.

Delaminácia kaolinitu a jeho transformácia na halloysit v prostredí iónovej kvapaliny

Kaolinite delamination and its transformation to halloysite during the treatment with ionic liquid

T. Zacher^{1,2}, V. Hronský³, M. Naftaly⁴, M. Čaplovičová⁵, K. Emmerich⁶, M. Janek^{2,7}

¹ State Geological Institute of Dionýz Štúr, Geoanalytical laboratories, Markušovská cesta 1, SK-052 40 Spišská Nová Ves, Slovakia

² Comenius University, Faculty of Natural Sciences, Department of Physical and Theoretical Chemistry, Mlynská dolina, SK-842 15 Bratislava, Slovakia

³ Department of Physics, Faculty of Electrical Engineering and Informatics, Technical University of Košice, Park Komenského 2, SK-042 00 Košice, Slovakia

⁴ National Physical Laboratory, Hampton Rd, Teddington, Middlesex, TW11 0LW, UK

⁵ Centre STU for Nanodiagnostics, Slovak University of Technology, SK-812 43 Bratislava, Slovakia

⁶ Karlsruhe Institute of Technology, P.O. Box 3640, D-76021 Eggenstein-Leopoldshafen, Germany

⁷ Slovak University of Technology, Faculty of Chemical and Food Technology, Radlinského 9, SK-812 37 Bratislava, Slovakia

ABSTRACT

The intercalation and thermal reactivity of well-ordered kaolinite with poorly ordered halloysite using the ionic liquid (IL) 1-ethyl-3-methylimidazolium ethyl sulphate was studied. Intercalation reactions of IL used the precursors Kaolinite–dimethylsulfoxide and Halloysite–dimethylsulfoxide intercalates for subsequent two hours lasting guest displacement reaction at 180°C. The successful replacement of dimethylsulfoxide in the interlayer space with IL was proved by several independent experimental techniques such as XRPD, FTIR, Simultaneous TG, SEM/TEM microscopy, Solid-state NMR and THz spectroscopy. The thermal reactivity of kaolinite and halloysite IL intercalates was tested subsequently in batch mode experiment at elevated temperature 250 °C for two hours. The TEM showed that kaolinite layers upon repeated treatment with IL preserved their platy morphology, however, rounded particle edges could be observed. This was in contrast to X-ray powder diffraction data which have shown transformation of kaolinite to halloysite-like material. Such delaminated kaolinite may have improved reactivity in specific ceramic applications.

Keywords: kaolinite, halloysite, intercalation, ionic liquid, transformation

INTRODUCTION

The modification of chemical composition and structural properties of inorganic guest particles used as ore in special ceramic synthesis is the strategy how to control and improve the existing properties, or to prepare materials with novel properties. For the preparation of oxide or non-oxide ceramics from the natural low cost clay nanoparticles, different types of materials could be synthesized, depending on the host compound chosen. The 1:1 layered clay mineral kaolinite is frequently investigated for hybrid material preparation, thanks to its abundant occurrence and interesting asymmetric chemical structure. The single kaolinite layer contains gibbsite sheet with aluminol groups on one side, suitable for modification in specific topotactic reaction, connected by the other side to less reactive silicon oxide sheet hexagonal rings with ditrigonal symmetry. Single layers of mineral are formed from two such sheets (1:1 ratio) held together by intense hydrogen bonds among aluminol groups oriented towards silicon oxide atoms of neighbouring layer. Under such conditions only specific reactive guest

molecules can be introduced between single host kaolinite layers. In 2005 Letaief and Detellier reported the first "kaolinite-ionic liquid" intercalation based on pyridinium salt derivate followed by reports of a series of novel kaolinite-ionic liquid materials based on imidazolium and/or alkylammonium derivatives.[1-6] Intercalation of such chemical substances is particularly interesting as this indicate that even molecular species with higher molar mass values can be intercalated in the interlayer space of kaolinite and used for its chemical modification. Such results reflect the behavior of host kaolinite and support the strategy for design of new interesting materials, their chemical functionality and help to achieve material target application. In presented study were compared dioctahedral clay minerals with the comparable chemical formula of $\text{Al}_2\text{Si}_2\text{O}_5(\text{OH})_4$ and $\text{Al}_2\text{Si}_2\text{O}_5(\text{OH})_4 \cdot 2\text{H}_2\text{O}$ per half unit cell for kaolinite and halloysite, respectively. Thanks to its natural nanosized tubular morphology, the later mineral can intercalate monolayer of water molecules in the interlayer space as indicated by the chemical formula above. During the materials preparation a reliable identification of chemical reactions taking place in synthesized materials, novel physical-chemical methods are required for their monitoring. In the presented study was used terahertz time domain spectroscopy (THz-TDS) to examine confined specific host-guest hybrid systems with interesting physical-chemical properties, based on intercalation of kaolinite and halloysite with ionic liquid (IL) 1-ethyl-3-metylimidazolium ethyl sulphate.

EXPERIMENTAL

Materials. The Kaolinite material used in this study was from a primary deposit in Bayern-Oberpfalz at Hirschau, Germany (abbreviated KBO) and Slovak Halloysite from the locality of Biela Hora at Michalovce region (abbreviated HBH). Both techniques used for basic sample characterisation, X-ray powder diffraction (XRPD) and mid-infrared Fourier transform (FTIR) analyses confirmed that highly crystalline kaolinite and less ordered halloysite were the major components of the phases present. In the KBO sample, XRPD detected a minor admixture of illite-like clay mineral. Thermogravimetric analysis showed the highest dehydroxylation gradient at 536 °C with a mass loss of 12.88 % for KBO and at 509 °C with a mass loss of 15.06 % for HBH which agrees closely with the mass loss of 13.9% predicted from the ideal structural formula. Transmisson electron microscopy of the KBO powder shows aggregates of platy particles with lateral lengths of up to 2.0 μm and typical hexagonal and/or pseudo-hexagonal symmetry. For the HBH halloysite sample, tubes, rolls and irregular globular particles with lateral lengths of about 0.5 μm were found (Figure 1).

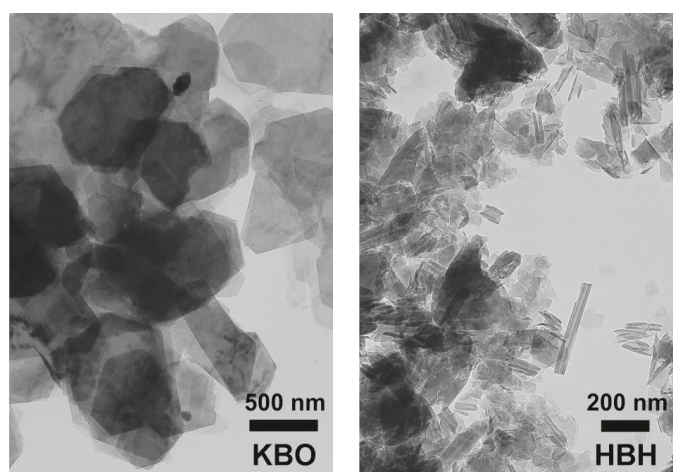


Figure 1: TEM images of starting KBO and HBH samples prior their intercalation with DMSO.

Intercalation reactions. To prepare Kaolinite and Halloysite intercalates with IL, known guest displacement reaction was used.[1-6] For primary intercalates which opens the interlayer galleries of these clay minerals the dimethylsulfoxide as guest molecules were used,

hence dimethylsulfoxide–Kaolinite (DMSO-KBO) and dimethylsulfoxide–Halloysite (DMSO-HBH) intercalates were prepared.[7] These intercalates were used in subsequent guest–displacement reaction using imidazolium salt, 1-ethyl-3-methylimidazolium ethyl sulphate (Io-Li-Tec, quality 99+%, Figure 2). The reaction was done under mild nitrogen gas flow, and the temperature ramp at the heat rate of approximately 5 °C/min up to final 180±2 °C. The reaction mixture was stirred next two hours under nitrogen flow using magnetic stirrer. Afterwards was the solid removed with at least 4 time washing–centrifugation cycles, using a washing step with isopropanol and separation of intercalated particles by centrifuge sedimentation at 6000 rpm. The solids were ground and labeled as IL-KBO and IL-HBH materials. In the next step, almost identical with intercalation procedure of IL, however, using IL-KBO and IL-HBH as starting materials, was done to produce IL/IL-KBO and IL/IL-HBH intercalates. The only difference was focused on the final reaction temperature set up at 250±2 °C, lasting two hours under a flow of nitrogen.

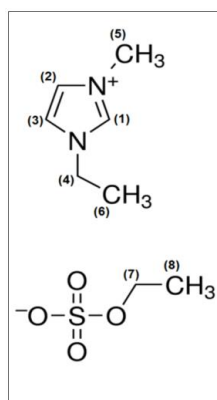


Figure 2: Chemical structure of imidazolium salt, 1-ethyl-3-methylimidazolium ethyl sulphate, with carbon numbers adopted according to a similar ionic liquid in SDBS spectral database.

Techniques. XRPD patterns from all samples were obtained using a PHILIPS PW 1710 X-ray powder diffractometer equipped with a Graphite secondary monochromator PW 1752 and Cu radiation source. The infrared spectra were obtained by a Nicolet 6700 Fourier Transform Infrared (FTIR) spectrometer from Thermo Scientific. The KBr pressed disk technique (1 mg of sample and 200 mg KBr) was used to measure spectra in the MIR region (4000 – 400 cm^{-1}) and spectral calculations were performed using the Thermo Scientific OMNICTM software package. The intercalate reactivity was monitored using a Simultaneous Thermal Analysis (STA) device STA 449C (NetzschGerätebau GmbH, Germany) with a TG/DSC sample holder linked to a Quadrupole Mass Spectrometer QMS 403C (InProcess Instruments / NetzschGerätebau GmbH, Germany). High-resolution solid-state Nuclear Magnetic Resonance (HRSS-NMR) measurements were carried out on a 400 MHz Varian solid-state NMR spectrometer (Palo Alto, CA, USA). Single-pulse (SP) MAS ^{13}C spectra as well as CP MAS ^{13}C spectra were recorded at the resonance frequency of 100.54 MHz and with the use of 4 mm ZrO_2 rotors and magic angle spinning rate of 10 kHz. Terahertz time domain spectroscopy (THz-TDS) was performed using laboratory build equipment with a common configuration based on a femtosecond laser driven photoconductive emitter and electro-optic detection. All measurements were done at the temperature of 20 ± 1 °C, and the THz beam path flushed with dry air to eliminate water absorption lines.

RESULTS

The FTIR spectroscopy is a well-established technique for monitoring of the chemical bonds in layered silicates due to typical vibration frequencies which are found in the mid-infrared region (see also Table 1).[8,9] FTIR spectra of DMSO intercalated Kaolinite and Halloysite

can be found elsewhere.[7] Comparison of IL vibration frequencies for pure IL and after its intercalation in the interlayer space of KBO and HBH are shown in the Figure 3.

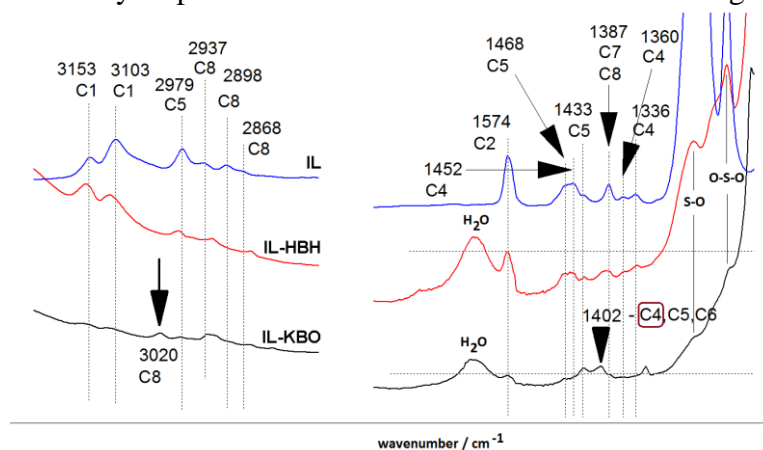


Figure 3: Comparison of absorption bands positions for pure IL and after its intercalation in the interlayer space of KBO and HBH with estimation of carbons involved and numbered as shown in the Figure 2.

The differences found indicate that i) typical C–H stretching frequencies in the range of 3160–2860 cm^{-1} found in pure IL have been slightly shifted to higher wavenumbers, in case the IL molecules were intercalated between the Halloysite layers. However, significant shifts in the stretching bands positions and decrease of their intensities were found if the IL was confined between the layers of Kaolinite. ii) Similar behaviour can be found in the bending, skeletal and rocking vibration region 1700–600 cm^{-1} . It can be expected that the confinement of IL molecules in the interlayer space of Kaolinite is different than in the Halloysite, and the hydrogen bonds interaction of IL with gibbsite sheet in Kolinite is much more intensive than in Halloysite. This interaction as the molecule is held in higher bonding filed is responsible for lesser thermal stability of IL in the interlayer space of Kaolinite than was observed for Halloysite. iii) Despite the precaution made to minimise the water adsorption by the solid samples, the H_2O deformation vibrations at 1600 cm^{-1} , were observed in both KBO and HBH intercalates. The presentation of these vibrations can be connected to intensive sample washing treatments performed with acetone, during removal of excess IL under laboratory conditions.

The intercalation of guest molecules in the interlayer space changes the first basal reflection observable by XRPD, which is indicative to the successful intercalation reaction and interlayer space modification. At the same time the next structural reflections located at 18–28° 2θ were also altered due to structure re-organisation in the c-direction of crystal layers. The most interesting change observed during our study was the gradual transformation of Kaolinite towards the Halloysite-like mineral, in course of guest displacement reaction with IL and high temperature treatment of IL-KBO intercalate in IL at 250 °C (Figure 4).

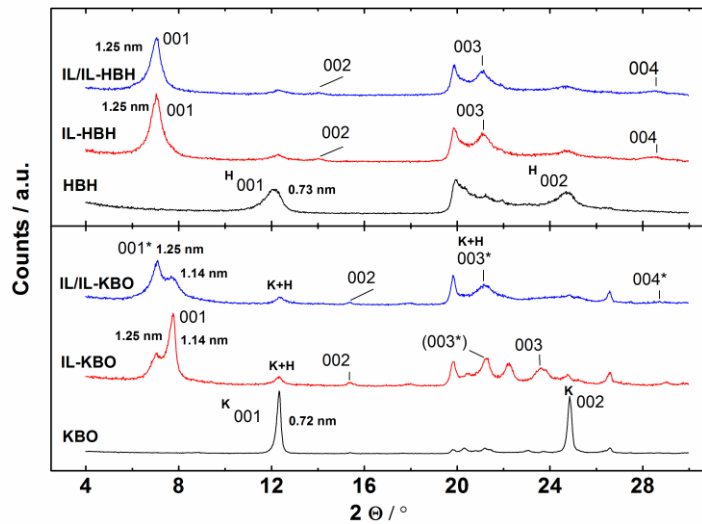


Figure 4: The XRPD patterns of Kaolinite and Halloysite and their intercalates with IL.

From XRPD patterns can be seen that that process of Kaolinite transformation towards Halloysite like structure started already with first intercalation of the ionic liquid at 180 °C and was pronounced with the second IL treatment at 250 °C. According to the first basal spacing intensity ratios, the first guest displacement reaction with IL transformed about 30%, while the second treatment transformed about next 30% of Kaolinite to Halloysite-like mineral. The transformation was also confirmed by the TEM where rounded edges of kaolinite particles can be observed on the images for IL-KBO and IL/IL-KBO materials (Figure 5). Interestingly, the Kaolinite particles preserved their platy morphology despite the 60% transformation to Halloysite-like material.

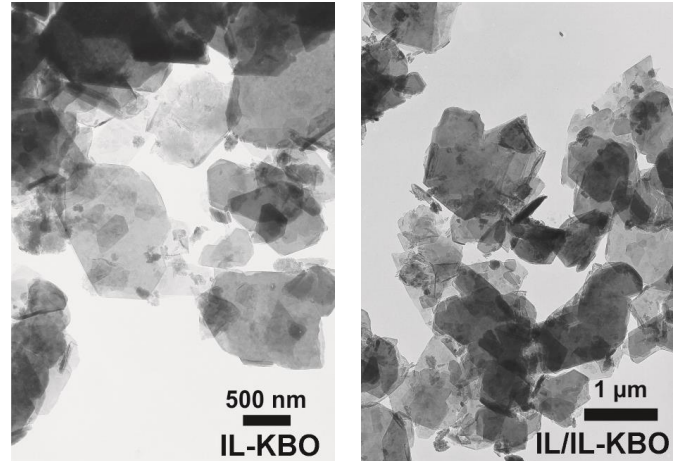


Figure 5: TEM images of starting IL-KBO and IL/IL-KBO samples.

CONCLUSIONS

The imidazolium ionic liquid intercalation into interlayer space of Kaolinite and Halloysite was studied. The products of intercalation reactions were characterized by XRPD, IR spectroscopy, TG-DSC-MS, TEM, Nuclear Magnetic Resonance (HRSS-NMR) and THz time-domain spectroscopy. It was found that 1-ethyl-3-metylimidazolium ethyl sulphate is suitable agent for intercalation and additionally, it is able to transform the Kaolinite to Halloysite-like mineral. During this process the size of crystallite particles is decreased trough their delamination perpendicular to the c-direction of crystals and morphology changes to Halloysite.

ACKNOWLEDGMENT

The authors acknowledge support from MPNS COST ACTION MP1204 - TERA-MIR Radiation: Materials, Generation, Detection and Applications, which promoted cooperation between CU in Bratislava, Slovakia and NPL in Middlesex, UK. Financial support of Slovak Grant Agency VEGA (grant No. 1/0690/15) is also greatly acknowledged.

Table 1: Attribution of FTIR vibrations for the Kaolinite and Halloysite and their intercalates with DMSO or IL.

Wavenumber / cm^{-1}	Attribution
3695	O-H stretching of inner-surface hydroxyl groups 1 of kaolinite
3670	O-H stretching of inner-surface hydroxyl groups 2 of kaolinite
3652	O-H stretching of inner-surface hydroxyl groups 2 of kaolinite
3620	O-H stretching of inner hydroxyl groups of kaolinite
3600-3100	O-H stretching of water molecules
3100-2900	C-H stretching (asymmetric)
2850-2855	C-H stretching (symmetric)
1650-1550	O-H bending of water molecules + C-N rocking vibrations of IL
1500-1400	C-H scissoring
1400-1300	IL ring stretching (symmetric) vibrations (skeletal modes) + C-H bending (symmetric)
1300-1160	C-N stretching + O-S-O (or S-O) stretching + C-H bending
1115	Si-O stretching (longitudinal mode)
1103	Si-O stretching (perpendicular)
1040-1005	Si-O stretching (in-plane)
937	O-H bending of inner-surface hydroxyl groups
913-900	O-H bending of inner hydroxyl groups
800-789	Si-O
760-740	Si-O (perpendicular)
700-680	Si-O (perpendicular)
550-508	Al-O-Si (Al in octahedral sheet)
470-463	Si-O-Si bending
435-430	Si-O bending + C-N-C bending

LITERATÚRA

- [1] Letaief S. and Detellier Ch. Reactivity of kaolinite in ionic liquid: preparation and characterization of a 1-ethyl pyridiniumchloride-kaolinite intercalate. *Journal of Materials Chemistry*, 15 (2005) 4734–4740.
- [2] Letaief S. and Detellier Ch. Nanohybrid materials from the intercalation of imidazolium ionic liquids in kaolinite. *Journal of Materials Chemistry*, 17 (2007) 1476–1484.
- [3] Letaief S. and Detellier Ch. Ionic liquids-kaolinite nanostructured materials. Intercalation of pyrrolidinium salts. *Clays and Clay Minerals*, 56 (2008) 82–89.
- [4] Letaief S. and Detellier Ch. Functionalization of the interlayer surfaces of kaolinite by alkylammonium groups from ionic liquids. *Clays and Clay minerals*. 57 (2009) 638–648.
- [5] Letaief S. and Detellier Ch. Application of thermal analysis for the characterisation of intercalated and grafted organo-kaolinite nanohybrid materials. *Journal of Thermal Analysis and Calorimetry*, 104 (2011) 831–839.
- [6] Dedzo G. K., Ngnie G. and Detellier Ch. PdNP Decoration of Halloysite Lumen via Selective Grafting of Ionic Liquid onto the Aluminol Surfaces and Catalytic Application. *ACS Applied Materials & Interfaces*, 8 (2016) 4862–4869.

- [7] Zich D., Zacher T., Darmo J., Szöcs V., Lorenc D. and Janek M. Far-infrared investigation of kaolinite and halloysite intercalates using terahertz time-domain spectroscopy. *Vibrational Spectroscopy*, 69 (2013) 1–7.
- [8] Madejová, J., Komadel, P. Baseline studies of the clay minerals society source clays: Infrared methods. *Clays and Clay minerals* 49 (2001) 410–432.
- [9] Janek M., Zich D. and Naftaly M. Terahertz time-domain response of amines and aminoacids intercalated smectites in far-infrared region, *Materials Chemistry and Physics*, 145 (2014) 278–287.

Závislosť vlastností SiO₂ sólov a xerogélov od zloženia**Dependence of the properties of SiO₂ sols and xerogels on the composition**P. Balážová^{1*}, M. Čierniková¹, A. Plško¹, P. Exnar², J. Pagáčová³, I. Papučová³¹ *Vitrum Laugaricio – Joint Glass Center of the TnUAD, Študentská 2, 911 50 Trenčín, Slovakia*² *Technical University of Liberec, Faculty of Science, Humanities and Education, Studentská 2, 461 17 Liberec, Czech Republic*³ *Alexander Dubček University of Trenčín, Faculty of Industrial Technologies in Púchov, I. Krasku 491/30, 020 01 Púchov, Slovakia** e-mail: petra.balazova@tuni.sk**ABSTRACT**

The work deals with the study of electrostatic stabilization of aqueous SiO₂ sols. Simultaneously, it examines the effect of composition on properties of SiO₂ sols and xerogels. The polysilicic acid sol was unstable with fast gelation, and therefore it was stabilized by the addition of NaOH solution so that the molar ratio of SiO₂:Na₂O was 80:1, 100:1, 150:1, 200:1 and 250:1. For stabilized SiO₂ sols, the size of particles was measured. The size of particles was characterized by estimation of mean value of particles size and extent of their dispersion using log-normal distribution. Because xerogels are highly porous material, the porosity was determined using nitrogen adsorption. The bimodal distribution of particles size in sols was found from distribution curves. Investigations using dynamic light scattering and nitrogen adsorption showed that the particle size, specific surface area and pore diameter increased with increasing SiO₂:Na₂O ratio.

Keywords: sol-gel method, silicic acid, electrostatic stabilization, aqueous SiO₂ sol, properties of SiO₂ nanoparticles

INTRODUCTION

Stabilized SiO₂ sols exhibit unique and sophisticated characteristics which have applications in many fields of industry, for example as cleaners and detergents, modifying reagents in flotation, binders in agglomeration, in building industries, in food, in cosmetics or health [1, 2]. In the mentioned application, the stability of sols plays an important role that can be achieved by electrostatic, steric stabilization, or their combination [3]. The quality of final product is highly dependent on the size and size distribution of SiO₂ particles [4]. The unique chemical properties, such as buffering ability, surface charges, modifying ability, heat and chemical stability, polymerizing capability and viscosity regulating ability can be achieved selecting a suitable composition and preparation conditions of sols [2]. The most widely used and most important method for the preparation of stabilized sols, which allows to control of the reaction parameters, is the sol-gel method [5].

EXPERIMENTAL

For the preparation of SiO₂ sols an aqueous solutions of sodium silicate have been used, which were fabricated by reaction of amorphous SiO₂ with a solution of NaOH at a ratio 3:1. The solution of sodium silicate was diluted with distilled water so that the SiO₂ content was 5 wt. %. The polysilicic acid sol was obtained by cation exchange of Na⁺ and H⁺ using ion exchanger. The prepared sol was not stable with fast gelation, therefore it was stabilized by addition of NaOH solution so that the ratio of SiO₂:Na₂O was 80:1, 100:1, 150:1, 200:1 and

250:1. and the pH in the range of 8-10.5. The stabilized sol was refluxed for 3 hours. The xerogel was prepared from the SiO₂ sol at 80 °C after 24 hours of ageing.

The particle size of sols was determined by dynamic light scattering method. Measurements of particle size and size distribution were carried out on the device Zetasizer Nano ZS-ZEN3601 in TUL of Liberec. The outputs of measurements were intensities and their subsistent particle size, from which the distribution curves (DC) were treated in the Matlab software package. The estimation of the mean value (D-LND) and the extent of particles dispersion (SD-LND) were calculated by assuming a log-normal particles size distribution.

Information about the porosity of SiO₂ xerogels were obtained using measurements by nitrogen adsorption technique on the instrument Autosorb iQ Station 1 - Quantachrome® Instruments in TUL of Liberec.

RESULTS

The bimodal distribution of particles size in sols was determined from distribution curves. When the SiO₂:Na₂O ratio is increasing, the particles size increased in the first part of DC (Fig. 1a) for D-LNR value from 2.6 nm to 3.2 nm and for SD-LNR value from 0.7 nm to 1.2 nm. In the second part of DC (Fig. 1b) the particles size increased significantly, for D-LND value from 23.3 nm to 78.1 nm and for SD-LNR value from 9.7 to 69.2 nm.

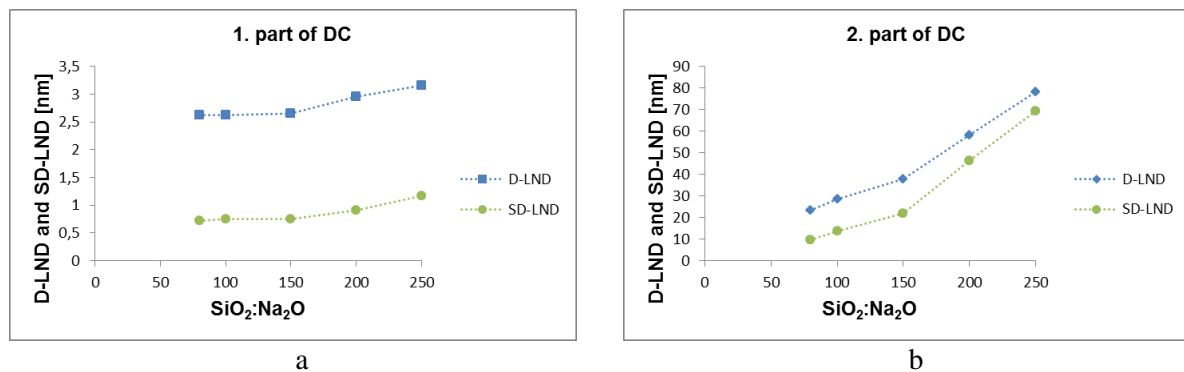


Fig. 1: The estimation of the mean value and the extent of particles dispersion for different SiO₂:Na₂O ratio: a) in the first part of DC, b) in the second part of DC.

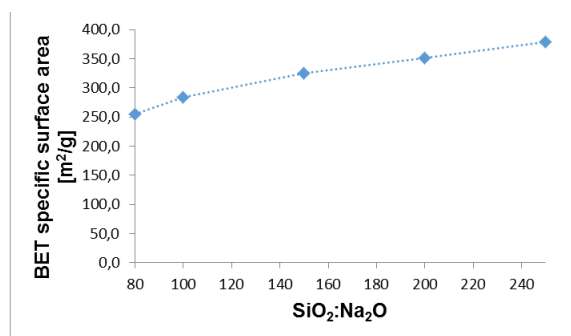


Fig. 2: The dependence of the specific surface area on the SiO₂:Na₂O ratio.

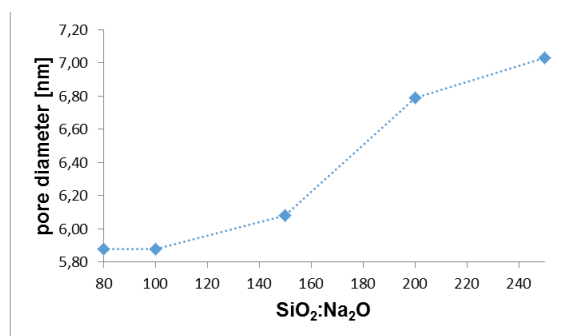


Fig. 3: The dependence of pore diameter on the SiO₂:Na₂O ratio.

From porosity measurements of SiO₂ xerogels the specific surface area was evaluated from the adsorption isotherms by the BET method. The specific surface area of SiO₂ xerogels increased with increasing the SiO₂:Na₂O ratio (Fig. 2). The pore diameter of SiO₂ xerogels

was calculated based on DFT method. From the dependence of pore diameter on the SiO₂:Na₂O ratio (Fig. 3) it was found, that at ratio 80:1 and 100:1 the pore diameter is about 5.9 nm. With further increase of SiO₂:Na₂O ratio the pore diameter increased to 7.0 nm. The particles growth and increasing of porosity could be caused by the fact that during decreasing of the concentration of Na⁺ ions, the repulsive force between the particles decreased and it leads to formation of larger particles and aggregates. The increase of porosity is connected with the formation of larger particles and aggregates.

CONCLUSION

The effect of SiO₂:Na₂O ratio on the structure and properties of stabilized aqueous SiO₂ sols and their xerogels was studied in this work. The results showed that the particles size in sols as well as the porosity of SiO₂ xerogels increased with increasing SiO₂:Na₂O ratio, i.e. the stability of sols decreased. The observed particles growth and porosity with the increasing SiO₂:Na₂O ratio can be explained by electrostatic stabilization – during decreasing of the concentration of Na⁺ ions, the repulsive force between particles decreased and result is the formation of larger particles and aggregates.

REFERENCES

- [1] Bergna, H. E., Roberts, W. O. Colloidal silica fundamentals and applications, CR Taylor and Francis, Boca Raton (2006) 884.
- [2] Yang, X., Roonasi, P., Holmgren, A. A study of sodium silicate in aqueous solution and sorbed by synthetic magnetite using in situ ATR-FTIR spectroscopy, *Journal of Colloid and Interface Science*, **328** (2008) 41-47.
- [3] Stoylov, S. P. Stable colloids at the isoelectric point: dipolar vs. electrostatic interactions, *Colloids and Surfaces A: Physicochemical and Engineering Aspects*, **460** (2014) 516-518.
- [4] Rao, K. S. et al. A novel method for synthesis of silica nanoparticles, *Journal of Colloid and Interface Science*, **289** (2005) 125-131.
- [5] Rahman, I. A., Padavettan, V. Synthesis of silica nanoparticles by sol-gel: size-dependent properties, surface modification, and application in silica-polymer nanocomposites – A review, *Journal of Nanomaterials*, (2012) 15.

Vplyv zloženia anorganicko-organických sólov na vlastnosti anorganicko-organických vrstiev

The effect of the composition of inorganic-organic sols on the properties of the inorganic-organic layers

M. Čierniková^{1*}, P. Balážová¹, A. Plško¹, P. Exnar², J. Pagáčová³, I. Papučová³

¹ *Vitrum Laugaricio – Join Glass Centre of the TnUAD, Študentská 2, 911 50 Trenčín, Slovakia*

² *Technical University of Liberec, Faculty of Science, Humanities and Education, Studentská 2, 461 17 Liberec, Czech Republic*

³ *Alexander Dubček University of Trenčín, Faculty of Industrial Technologies in Púchov, I. Krasku 491/30, 020 01 Púchov, Slovakia*

* e-mail: marianna.ciernikova@tnuni.sk

ABSTRACT

The present paper describes the effect of the composition of inorganic-organic sols on the surface properties of inorganic-organic layers prepared from tetraethoxysilane (TEOS) as inorganic precursor and triethoxyoctylsilane (TriEOS) as modifying organic precursor. The hydrophobicity of the inorganic-organic layers was determined utilizing the contact angle of water. The contact angle on inorganic-organic layers was determined by the method of sessile drop. The Owens-Wendt-Rabel-Kaelble method was used for calculation of the surface free energy and its polar and dispersion components.

Keywords: inorganic-organic layers, dip-coating technique, hydrophobic surface, surface free energy

INTRODUCTION

Inorganic-organic materials have attracted considerable attention due to their excellent properties, such as their high resistance to wear, near-perfect adhesion to the substrate, thermal stability, mechanical strength, high transparency and good processibility [1, 2]. These materials are most commonly prepared by sol-gel method in the form of thin layers on various substrates. The application of inorganic-organic materials includes anti-reflective, anti-static and diffusion layers, anti-corrosion and scratch resistant layers, hydrophobic layers, contact lenses, dental filling materials and many others [1]. The surface free energy plays a crucial role in these applications. The aim of this work was to study the effect of the molar ratios $x(\text{TEOS}):x(\text{TriEOS})$ and $x(\text{H}_2\text{O})/(x(\text{TriEOS})+x(\text{TEOS}))$ on hydrophobicity and surface free energy of inorganic-organic layers.

EXPERIMENTAL

Three groups of inorganic-organic sols with molar ratios $x(\text{TEOS}):x(\text{TriEOS}) = 8:0, 7:1, 6:2, 5:3, 4:4$ and $x(\text{H}_2\text{O})/(x(\text{TriEOS})+x(\text{TEOS})) = 2, 4, 6$ were prepared in the system TriEOS-TEOS-H₂O-IPA-HNO₃ by sol-gel method. Inorganic-organic sols were applied by the dip-coating technique on glassy substrates and subsequently dried at 140 °C for 2 hours. The prepared layers were placed in environment with RH 43.2 % after free cooling to room temperature. The contact angle on prepared inorganic-organic layers was determined by the method of sessile drop. Diiodomethane ($\gamma_l = \gamma_l^d = 50.8 \text{ mJ.m}^{-2}$) and distilled water ($\gamma_l^d = 21.8 \text{ mJ.m}^{-2}$, $\gamma_l^p = 51 \text{ mJ.m}^{-2}$) were used as measuring liquids. The profiles of drops were scanned by Drop Shape Analyzer – DSA30. The Owens-Wendt-Rabel-Kaelble method was used for calculation of surface free energy, polar and dispersion components using the

observed contact angles of distilled water and diiodomethane. The surface free energy (SFE) was calculated according the equation Eq. (1):

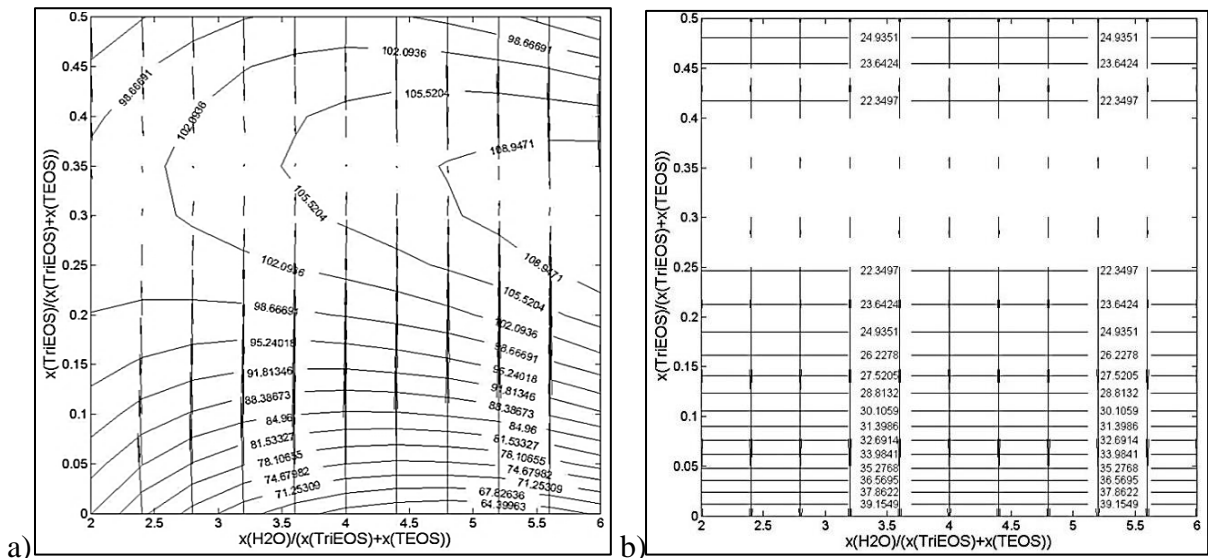
$$\frac{(1+\cos\theta)\cdot\gamma_l}{2\sqrt{\gamma_l^d}} = \sqrt{\gamma_s^p} \sqrt{\frac{\gamma_l^p}{\gamma_l^d}} + \sqrt{\gamma_s^d} \quad (1)$$

where γ_l is the SFE of a measuring liquid ($J.m^{-2}$), γ_l^d is the dispersion component of SFE of a measuring liquid ($mJ.m^{-2}$), γ_l^p is the polar component of SFE of a measuring liquid ($mJ.m^{-2}$), γ_s^p is the polar component of SFE of a measuring solid ($J.m^{-2}$), γ_s^d is the dispersion component of SFE of a measuring solid ($J.m^{-2}$) and θ is the contact angle between the solid and the measuring liquid.

The best description of the studied dependences is the polynomial regression which was selected by mathematical-statistical procedures using AIC criteria [3, 4].

RESULTS

Fig. 1a shows the dependence of contact angle for water on molar ratios $x(TriEOS)/(x(TriEOS)+x(TEOS))$ and $x(H_2O)/(x(TriEOS)+x(TEOS))$ on inorganic-organic layers. The inorganic-organic layers prepared from sols without TriEOS and with different water content were hydrophilic. With rising molar ratios $x(TriEOS)/(x(TriEOS)+x(TEOS))$ and $x(H_2O)/(x(TriEOS)+x(TEOS))$ were contact angles significantly higher than contact angles of layers prepared without triethoxyoctylsilane. These inorganic-organic layers were hydrophobic. The most hydrophobic surface was observed for layer prepared from the sol with molar ratios $x(TriEOS)/(x(TriEOS)+x(TEOS)) \sim 0.35$ and $x(H_2O)/(x(TriEOS)+x(TEOS)) \sim 6$.



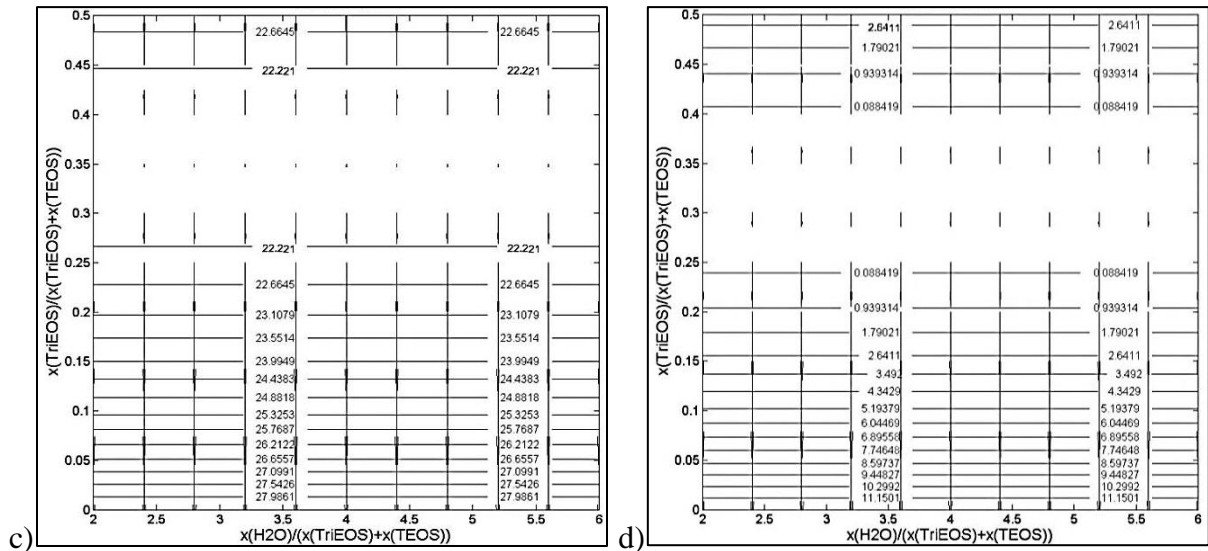


Fig. 1: The dependence of: a) contact angle for water, b) surface free energy, c) dispersion component of SFE, d) polar component of SFE on molar ratios $x(\text{TriEOS})/(x(\text{TriEOS})+x(\text{TEOS}))$ and $x(\text{H}_2\text{O})/(x(\text{TriEOS})+x(\text{TEOS}))$

Fig. 1b shows the dependence of surface free energy on molar ratios $x(\text{TriEOS})/(x(\text{TriEOS})+x(\text{TEOS}))$ and $x(\text{H}_2\text{O})/(x(\text{TriEOS})+x(\text{TEOS}))$ on inorganic-organic layers. The surface free energy of layers prepared from sols with different addition of TriEOS was lower compared to layers prepared from sols without TriEOS. The lowest SFE was observed for layer prepared from sol with the molar ratio $x(\text{TriEOS})/(x(\text{TriEOS})+x(\text{TEOS})) \sim 0.35$. It also showed a high degree of correlation between surface free energy and contact angle. The molar ratio $x(\text{H}_2\text{O})/(x(\text{TriEOS})+x(\text{TEOS}))$ does not significantly affect the surface free energy. The same trend was also found for dispersion (Fig. 1c) and polar components of SFE (Fig. 1d).

CONCLUSION

The TEOS based hydrophobic layers were obtained using TriEOS as the modifying organic precursor by sol-gel method and dip-coating technique on glassy substrates. Based on the results we can conclude that the inorganic-organic layers prepared from sols with a molar ratio $x(\text{TriEOS})/(x(\text{TriEOS})+x(\text{TEOS})) \sim 0.35$ had the most hydrophobic surface and the lowest surface free energy. This molar ratio leads to the most favourable arrangement of the octyl groups on the surface of the prepared inorganic-organic layers.

REFERENCES

- [1] SANCHEZ, C. et al.: Applications of hybrid organic-inorganic nanocomposites, *Journal of Materials Chemistry* 15 (2005) 3559-3592.
- [2] KANG, D. J. et al: Fabrication and characterization of photocurable inorganic-organic hybrid materials using organically modified colloidal-silica nanoparticles and acryl resin, *Journal of Non-Crystalline Solids* 355 (2009) 397-402.
- [3] Akaike, H.: A new look at the statistical model identification, *IEEE Transactions on Automatic Control* AC-19 (1974) 716-723.
- [4] Johnson J. B., Omland K.S.: Model selection in ecology and evolution, *Trends in Ecology and Evolution* 19 (2004) 101-108.

Peny pripravené sól-gél procesom a stabilizované časticami SiO₂**Sol-gel foams stabilized by silica particles**Z. Hajdúchová¹, Ľ. Bača¹

¹ *Department of Inorganic Materials, Institute of Inorganic Chemistry, Technology and Materials, Faculty of Chemical and Food Technology, Slovak University of Technology, Radlinského 9, 812 37 Bratislava*

ABSTRACT

The effect of gelation parameters on silica foam formation was studied systematically. Silica foams were prepared by direct foaming of sol and stabilized by silica powder. The gel was prepared in-situ from the tetraethoxysilane stabilized with silica particles on the surface of the foam lamellas immediately after foam formation, but before the foam collapsed. Finally, highly porous silica foams with low shrinkage and bulk densities of ~120 up to ~ 360 kg.m⁻³ were successfully prepared.

Keywords: silica, foams, sol-gel

INTRODUCTION

Highly porous materials have become of interest to scientists in recent decades due to their excellent insulation properties that give it the potential to improve technologies in a variety of fields e.g. refrigeration, buildings, construction, pipelines. In particular, aerogels offer the lowest densities and the lowest thermal conductivities of any known solid. However, drying controlled by capillary pressure resulting in the shrinkage of the gel is a critical step. Today, only supercritical drying (SCD) method, where the pore liquid is removed above the critical temperature (T_{cr}) and critical pressure (P_{cr}) of the concerned liquid is widely used for preparation of aerogels. At this point there is no liquid–vapour interface and, thus, no capillary pressure [1]. This method however has several limitations such as small maximum dimensions (a few cm or less) or specific geometries, usually high-aspect-ratio structures without sharp corners like discs and rods. Therefore to improve the materials processing and manufacturing routes without impairing the promising mechanical and thermal properties is a challenge for scientists.

Several processing routes using replica, sacrificial template and direct foaming techniques are available for the preparation of highly porous materials (foams) [2]. In direct foaming methods, ceramic foams are produced by incorporating air into a suspension. Wet foams are thermodynamically unstable systems which are sensitive to destabilization mechanisms such as drainage, coalescence and Ostwald ripening, leading to foam collapse. The stabilization of foams can be achieved by rapidly setting the wet foams by sol-gel process. The chemical steps involved in sol-gel polymerization, hydrolysis and condensation, result in formation of a network of Si-O-Si chemical linkages from the alkoxy silane. A subsequent key step is the gel drying process. During this time, the volume of the gel is reduced by approximately 80% resulting in a silica xerogel [3]. In this work, first results of foams prepared by direct foaming method of silica powder and stabilized by sol-gel process with minimal shrinkage are presented.

EXPERIMENTAL

The starting materials used in the foam preparation were tetraethoxysilane (TEOS, ≥99%, Fluka), dodecylbenzene sulfonic acid (DBSA, 95%, Aldrich) as an acid catalyst and also as

a surfactant, NH_4OH (0.1 M) as a base catalyst, SiO_2 particles (10 μm , 99.5%, AlfaAesar) and distilled water. The foams were prepared using the following two-step process.

First, the gelation time was studied by using different volume ratios of TEOS to water (from 1:2 to 1:8). The mixture was acidified with DBSA to catalyze the TEOS hydrolysis. The volume ratio of TEOS to acid was changed from 1:0.01 to 1:0.0175. The solution was stirred 1h at room temperature and the gelation time was adjusted by the diluted ammonium hydroxide (0.1 M) [4]. The foaming of the pure hydrosol was carried out using a laboratory mixer at a mixing velocity of 800 rpm for 90 s. In the second step, the pure sol-gel foams were stabilized by silica particles with the average particle size of 10 μm to prevent the shrinkage. The weight ratios of TEOS to silica particles were 1:2, 1:3 and 1:4. The resulting wet foams were casted into a mould and dried at room temperature for 48-72 h. The bulk density was calculated from the weight-to-volume ratio. The microstructure was analyzed by the light microscope ZEISS Stemi 508 and by the scanning electron microscope HITACHI SU3500.

RESULTS

The gelation time depends on the amount of TEOS, DBSA and also on the amount of base addition as shown in Fig. 1. The wet foams are unstable systems leading to foam collapse. Strengthening can be achieved by gelation of the foam lamella immediately after foam formation. The most important step was to find the parameters needed for preparation of hydrosol foam just before the gelling occurs.

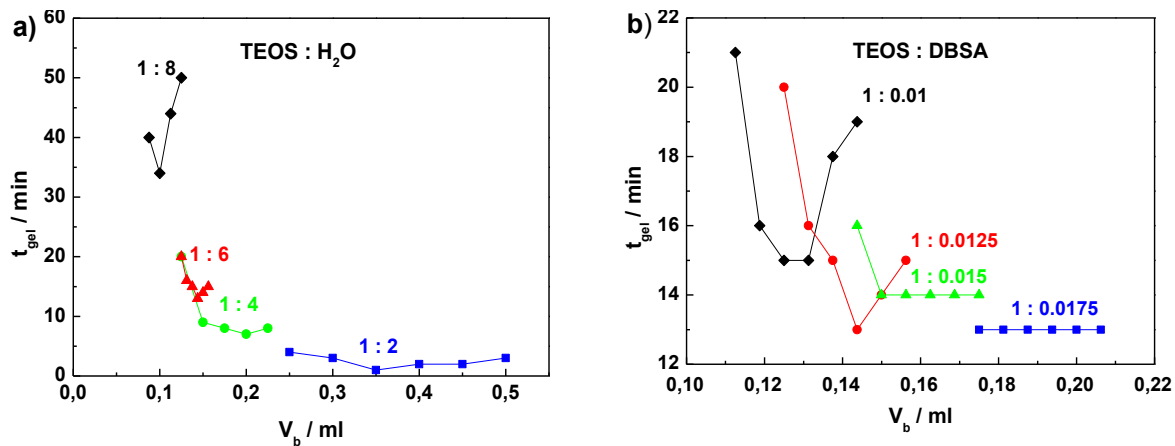


Fig. 1: Gelation time of hydrosols as a function of base addition V_b .

Depending on base and H_2O content, the gelation time was found to vary from few minutes to 1 hour. At constant amount of DBSA, the time of gelation decreases with decreasing H_2O content (Fig. 1a). The gelation time of the hydrosols (TEOS: H_2O =1:6) as a function of base addition and amount of DBSA is shown in Fig. 1b. At constant amount of H_2O , the time of gelation decreases with increasing DBSA content. The best performance showed the combination of TEOS: H_2O =1:4 with the gelation time about 5-10 minutes and TEOS:DBSA ratio of 1:0.015. Further experiments using silica particles as “building blocks” against the foam shrinkage were carried out with these parameters.

Tab. 1: Bulk density of silica foams at various TEOS : silica particles weight ratios.

Sample	TEOS : SiO_2	Bulk density ($\text{kg}\cdot\text{m}^{-3}$)
S2	1:2	122
S3	1:3	200
S4	1:4	363

If silica particles were used, the foam structure was stabilized and the volume shrinkage was reduced. It was also observed, that silica powder had only minor effect on the time of gelation. Figure 2 shows the microstructures of the foams prepared by direct foaming method with silica particles as structural barrier against the shrinkage. Foams were prepared with different quantity of SiO_2 particles and their bulk densities are shown in Table 1.

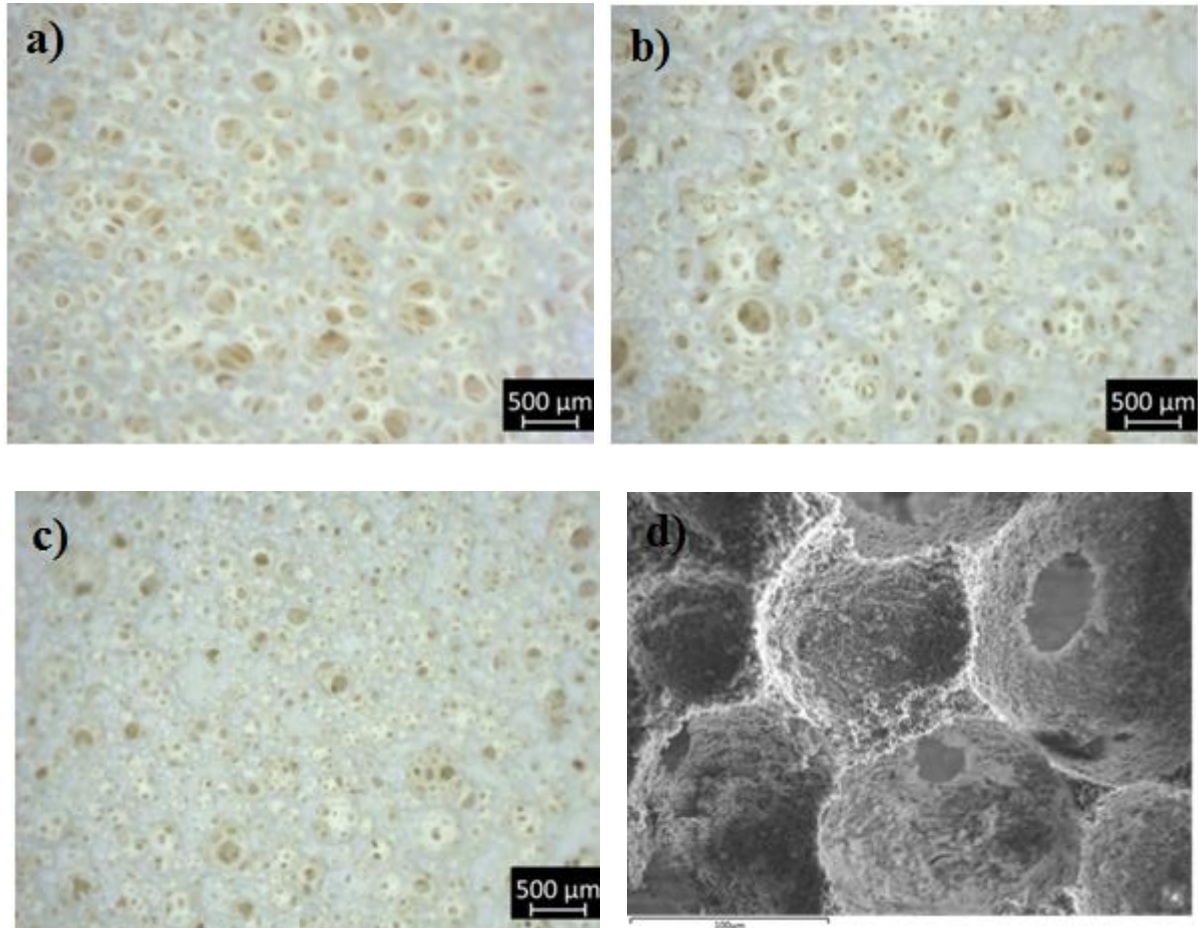


Fig. 2: Microstructures of the silica foams produced by direct foaming method: weight ratio TEOS : $\text{SiO}_2 = 1:2$ (a); TEOS : $\text{SiO}_2 = 1:3$ (b,d); TEOS : $\text{SiO}_2 = 1:4$ (c).

Bulk densities of as prepared silica foams increased with the decreasing TEOS:silica particles ratio. As can be seen in Figure 2 the pore size decreased with increasing fraction of silica particles, however this have to be proved by B.E.T. measurements or Mercury Intrusion Porosimetry.

CONCLUSION

Highly porous silica foam was prepared by direct foaming method with the bulk density as low as 120 kg.m^{-3} . Bulk densities of as prepared silica foams increased with decreasing TEOS:silica particles ratio. The volume shrinkage was partially eliminated by using silica particles, which stabilized the foam lamellae during the drying. Depending on base content and the amount of H_2O , the gelation time was found to vary from few minutes to 1 hour.

ACKNOWLEDGMENT

This work was financially supported by the Slovak Grant Agency VEGA Project No. 1/0696/15.

REFERENCES

- [1] Brinker, C.J., Scherer G.W. Sol–Gel Science - The Physics and Chemistry of Sol–Gel Processing. New York: Academic Press; 1990.
- [2] Studart, A.R., Gonzenbach, U.T., Tervoot E., Gauckler L.J. Processing Routes to Macroporous Ceramics: A Review, *J. Am. Ceram. Soc.*, 89 (2006) 1771-1789.
- [3] Buckley, A.M., Greenbkatt, M. Sol-Gel Preparation of Silica Gels, *J. Chem. Ed.*, 71 (1994) 599-602.
- [4] Jones, W.M., Fischbach, D.B. Novel processing of silica hydrosols and gels, *Journal of Non-Crystalline Solids*, 101 (1988) 123-126.

**Mn²⁺/Mn⁴⁺ dopované sklené a sklo-keramické materiály na báze hlinitanov
vzácných zemín: vplyv kompenzácie náboja na luminiscenčné vlastnosti**
**Mn²⁺/Mn⁴⁺ doped rare-earth aluminate glass and glass-ceramics materials: the
effect of charge compensation on luminescence properties**

K. Haladejová¹, R. Klement¹, A. Prnová¹, D. Galusek¹

¹ *Vitrum Laugaricio – Joint Glass Centre of the IIC SAS, TnU AD and FChPT STU, Trenčín*

ABSTRACT

The Mn²⁺ doped glasses in the systems Y₂O₃-Al₂O₃ and Y₂O₃-Al₂O₃-SiO₂ were prepared by flame-spraying synthesis in the form of glass microspheres from precursor powder synthesized by sol-gel method. The effect of charge compensation on luminescence was studied in details. The prepared glasses exhibit low thermal stability. The only phase crystallizing from glasses up to 1200°C is YAG (Y₃Al₅O₁₂). The glasses exhibit emission in green spectral region that is not affected by glass composition. The luminescence properties of polycrystalline Mn-doped phosphors are however significantly influenced by the presence of charge compensator (Si⁴⁺) in the host matrix. In charge non-compensated systems, the Mn⁴⁺ ions with red emission are preferred in the structure of the YAG host, while for the charge compensated systems Mn²⁺ ions with orange emission are favoured.

Keywords: luminescence, yttrium aluminium garnet, Mn-doped phosphors, charge compensation effect

INTRODUCTION

Phosphor-converted white light emitting diodes (pc-WLEDs) are regarded as new and perspective lighting sources for the next generation. The most of current pc-WLEDs utilise the yellow emitting Y₃Al₅O₁₂:Ce³⁺ (YAG:Ce³⁺) phosphor and blue InGaN LEDs [1]. However, YAG:Ce³⁺ phosphor has a deficient emission in red spectral region. To improve the red emission in current pc-WLED devices, a phosphor blend of YAG:Ce³⁺ and red emitting phosphor is generally applied [2]. The other way to increase the emission in the red spectral region rely on co-doped systems [3], containing except of Ce³⁺ also the element, transition metal or rare-earth, with efficient red light emission. In this case, the Ce³⁺ ion acts as a sensitizer, transferring a part of its energy to activator ion such as Mn²⁺ ion that in octahedral coordination emits orange-red light. To improve the emission of phosphors in the orange-red spectral region, the knowledge of manganese ions behaviour in a particular host matrix is inevitably required.

In the present work, we report on the preparation and characterization of Mn-doped glasses and polycrystalline phosphors in the system Y₂O₃-Al₂O₃ and Y₂O₃-Al₂O₃-SiO₂, respectively. The studied phosphors were prepared in the form of microspheres using the flame synthesis. The prepared glasses were characterized by optical microscopy (OM) scanning electron microscopy (SEM), X-ray diffraction (XRD), high temperature XRD (HT XRD) and differential scanning calorimetry (DSC) analysis. The polycrystalline phosphors were subsequently prepared by controlled crystallization of glasses. The effect of charge compensation (composition change) on luminescence was studied in details.

EXPERIMENTAL

The starting (precursor) powder was prepared by modified Pechini method [5] and glass microspheres by flame syntheses as described previously [6]. The dried powder of glass

microspheres was heat-treated in temperature calibrated tube furnace at 1200 °C for 5h (heating rate 10°C/min) in an air atmosphere. Thereafter, the glass and crystallized samples were reduced in N₂:H₂ (90:10 vol.%) atmosphere at 750 °C for 8h. The theoretical composition of the Mn²⁺ doped glasses is summarised in Tab. 1.

Table 1: The theoretical composition of the Mn²⁺ doped glasses (in mol. %).

SAMPLE	Al ₂ O ₃	Y ₂ O ₃	SiO ₂	MnO	Sum
A6Y4Mn2CNY	76,863	21,137	--	2,000	100,000
A6Y4Mn2CNAI	74,863	23,137	--	2,000	100,000
A6Y4Mn2CCYMnAlSi	74,863	21,137	2,000	2,000	100,000
A6Y4Mn2CC2AlMnSi	72,863	23,137	2,000	2,000	100,000
A6Y4Mn2ESA6Y4	75,326	22,674	--	2,000	100,000

The two types of charge compensated (CC) samples and 3 types of charge non-compensated (CN) samples have been prepared. The charge compensation was carried out by addition of SiO₂ into the A60Y40 system (76.86 mol. % (59.94 wt. %) Al₂O₃ and 23.13 mol. % (39.74 wt. %) Y₂O₃); e.g. substitution Y³⁺/Al³⁺ (+6) → Mn²⁺/Si⁴⁺ (+6). The prepared systems are denoted as follows: A6Y4Mn2CNY – substitution Y³⁺/Mn²⁺; A6Y4Mn2CNY – substitution Al³⁺/Mn²⁺; A6Y4Mn2CCYMnAlSi – substitution Y³⁺/Al³⁺ → Mn²⁺/Si⁴⁺; A6Y4Mn2CC2AlMnSi – substitution 2Al³⁺ → Mn²⁺/Si⁴⁺; A6Y4Mn2ESA6Y4 – substitution A6Y4 for MnO.

The morphology of the samples (the results not shown here) was examined by optical microscopy (NIKON LV 100 UDM, Japan), scanning electron microscopy (SEM, JEOL JSM-7600 F/EDS/WDS/EBSD, Japan). The DSC traces were recorded using Netzsch STA 449 F1 Jupiter (TG/DTA/DSC) at heating rate 10°C/min in the temperature range from room temperature to 1200 °C. The fluorescence spectra (excitation/emission) were recorded using Fluorolog FL3-21 spectrometer (Horiba). The 450 W xenon lamp was used as an excitation source. All spectra, except of excitation, presented herein were corrected for spectrometer response and lamp. The decay curves were measured using the phosphorescence module on the same spectrometer and Xe-flash lamp as the excitation source.

RESULTS

The prepared glass microspheres of all compositions (Tab. 1) were found to be XRD amorphous within detection limit.

The thermal properties of the Mn-doped samples were examined by DSC analysis. The DSC record of the glasses microbeads is shown in Fig. 1 and corresponding characteristic temperatures of two observed peaks are summarised in Tab. 2. As clearly seen in Fig. 1, whereas the first exothermic effect is almost not affected by change in the glass composition, the second exothermic peak is significantly affected.

The origin of the two crystallization peaks (exothermic effects) was examined by high temperature XRD (HT XRD) that revealed the crystallization of YAG phase (Y₃Al₅O₁₂) up to 1200 °C. The crystallization of α-Al₂O₃ phase was observed at temperatures above 1300 °C. According to this finding, both exothermic effects in DSC traces correspond to YAG phase crystallization; the first peak mainly to nucleation and partial crystallization of YAG phase (nanocrystals are formed), the second peak to crystal growth of YAG phase. This is also supported by the fact that position of the first crystallization peak is not significantly affected by the composition due to nucleation and nanocrystals formation that not markedly change the composition around formed nanocrystals. On the other hand, the growth of the larger crystals requires diffusion of the elements to already formed crystals. Diffusion of the elements is however closely related with the structure and composition of a glass around the YAG

crystals. Thus most likely diffusion plays the crucial role in the second exothermic effect and affects the peak position (peak temperature) and its half-width.

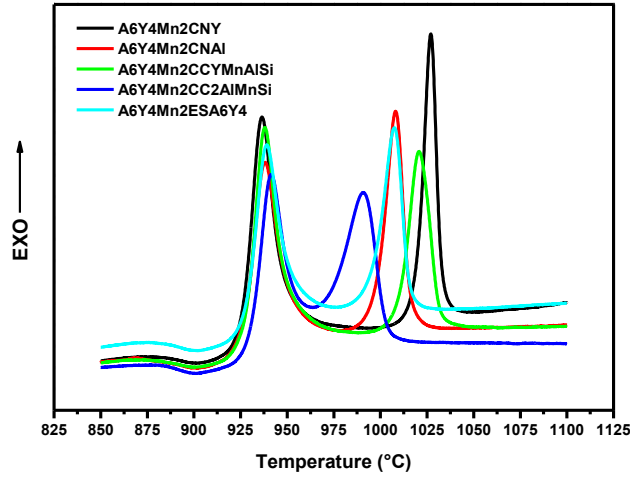


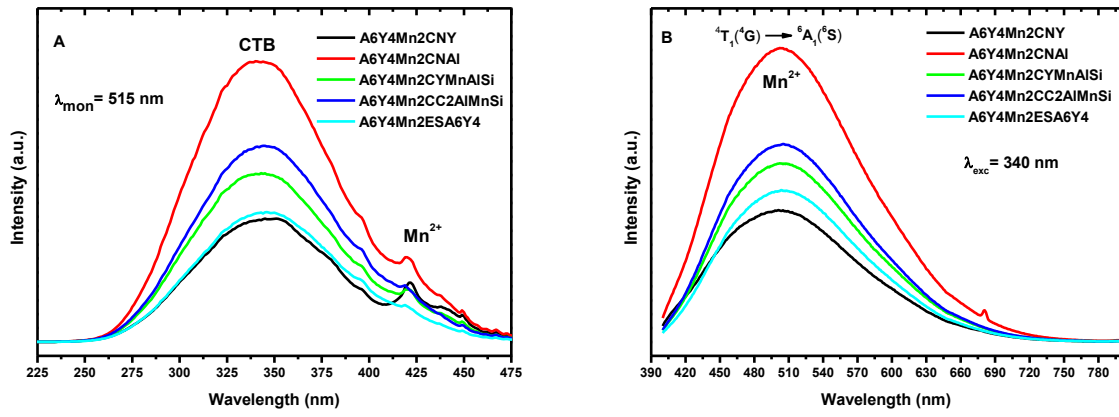
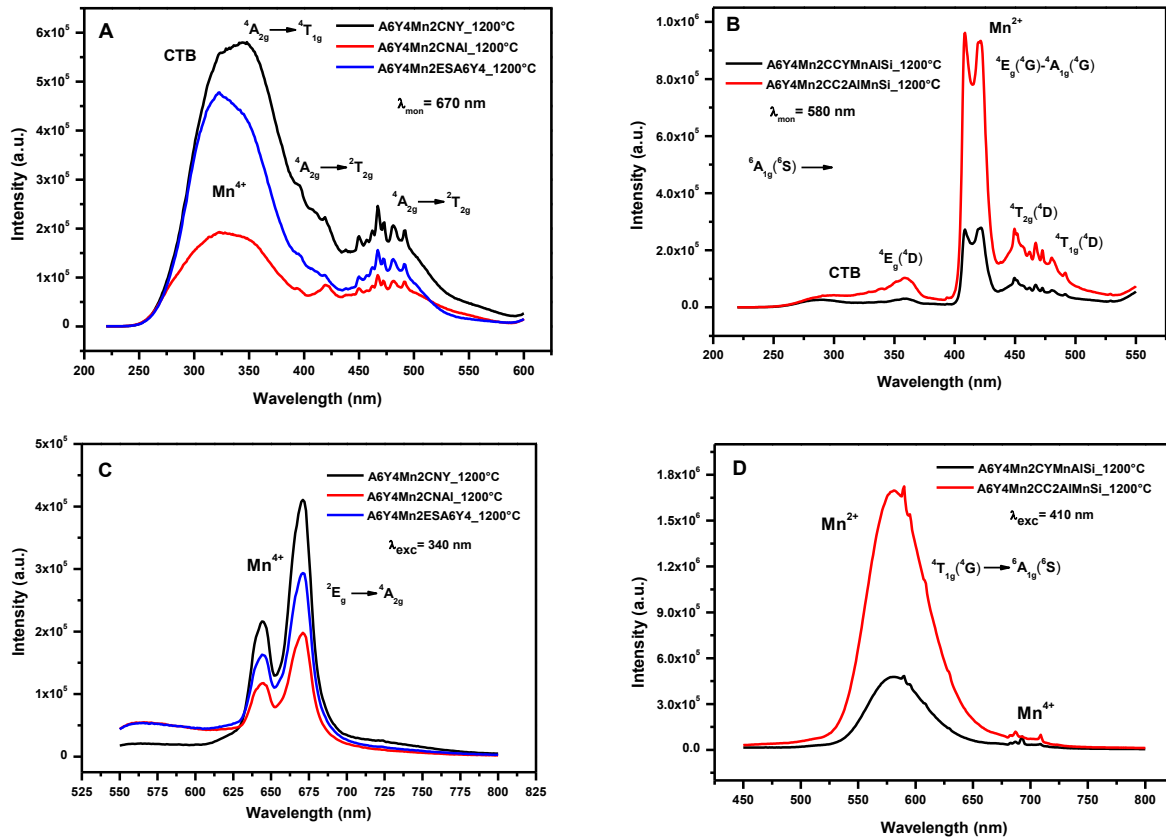
Fig. 1: DSC traces of as prepared Mn-doped glass microbeads.

Table 2: Characteristic temperatures of Mn-doped glasses estimated from DCS records.

SAMPLE	T_g (°C)	T_{x1} (°C)	T_{x2} (°C)	T_{p1} (°C)	T_{p2} (°C)
A6Y4Mn2CNY	885	926	1019	936	1027
A6Y4Mn2CNAI	869	926	998	938	1008
A6Y4Mn2CCYMnAlSi	877	927	1008	937	1021
A6Y4Mn2CC2AlMnSi	882	930	975	941	991
A6Y4Mn2ESA6Y4	875	927	996	939	1007

The excitation and emission spectra of Mn^{2+} doped glasses are shown in Fig. 2. The excitation spectra exhibit intensive broad absorption band that can be attributed to charge transfer (CT) transition within $Mn^{2+}-O^{2-}$. The much less intensive d-d transitions observed at 400-450 nm due to the Mn^{2+} ions are masked by strong CT absorption. The emission spectra of glasses exhibit broad featureless emission in the spectral range 400-650 nm with the maximum ~ 504 nm. This green emission is typical for the Mn^{2+} ions in tetrahedral coordination. Except of intensity, the emission (band maxima) is not significantly affected by the glass composition. In contrast to the glasses, the luminescence properties of polycrystalline Mn-doped phosphors (crystallized at 1200°C/5h) are significantly affected by the presence of charge compensator (Si^{4+} , in the structure as $[SiO_4]$ polyhedra) in the host matrix; Si^{4+} compensates the different charge between Y^{3+} and Mn^{2+} .

The photoluminescence (PL) spectra of charge compensated samples (A6Y4Mn2CCYMnAlSi and A6Y4Mn2CC2AlMnSi), shown in Fig. 3D, exhibit orange emission centred at ~ 580 nm, that is typical for octahedrally coordinated Mn^{2+} ions in the host matrix. The maximal orange emission intensity was observed for the sample A6Y4Mn2CC2AlMnSi.


 Fig. 2: The excitation (A) and emission (B) spectra of Mn^{2+} -doped glasses.

 Fig. 3: The excitation (A, B) and emission (C, D) spectra of crystallized glasses at $1200^{\circ}\text{C}/5\text{h}$.

Such remarkable difference in the emission intensities of both charge compensated samples is not clear yet. On the other hand, the PL spectra of charge non-compensated samples (A6Y4Mn2CNY, A6Y4Mn2CNAI and A6Y4Mn2ESA6Y4) are completely different. The spectral shape corresponds to typical absorptions and emissions of octahedrally coordinated Mn^{4+} ions in the host matrix. The emissions were observed in the red spectral region 620–700 nm with maxima at 645 and 670 nm. The decay times of for charge non-compensated samples were found to be ~ 0.2 and 0.9 ms, respectively, and this values are typical for the Mn^{4+} ions in octahedral coordination environment. The longer decay times with typical values for octahedrally coordinated Mn^{2+} ions were found for charge compensated samples ~ 1.7 and 7.3 ms. From the luminescence study of prepared polycrystalline phosphors results that in the case of charge non-compensated systems, the Mn^{4+} ions with red emission is preferred in the structure of the YAG host, while for the charge compensated systems Mn^{2+} ions with orange emission is favoured.

CONCLUSION

The manganese doped glasses were successfully prepared by flame-straying technique. The polycrystalline materials were prepared from glasses by controlled crystallization. The thermal analysis in combination with HT XRD revealed the crystallization of YAG phase in two distinct steps. The glasses exhibit emission in green spectral region, corresponding to tetrahedral coordinated of Mn^{2+} ions. In contrast to the glasses, the luminescence properties of polycrystalline Mn-doped phosphors (crystallized at 1200°C/5h) are significantly affected by the presence of charge compensator (Si^{4+} , in the structure as $[SiO_4]$ polyhedra) in the host matrix. In the case of charge non-compensated systems (A6Y4Mn2CNY, A6Y4Mn2CNAI and A6Y4Mn2ESA6Y4), the Mn^{4+} ions with red emission are preferred in the structure of the YAG host, while for the charge compensated systems (A6Y4Mn2CCYMnAlSi and A6Y4Mn2CC2AlMnSi) Mn^{2+} ions with orange emission are favoured.

ACKNOWLEDGMENT

The financial support of this work by the projects SAS-NSC JRP 2015/16 and VEGA 1/0631/14, is gratefully acknowledged. This publication was created in the frame of the project "Centre of excellence for ceramics, glass, and silicate materials" ITMS code 262 201 20056, based on the Operational Program Research and Development funded from the European Regional Development Fund.

REFERENCES

- [1] Yongfu L., Xia Z., Zhendong H., Xiaojun W. and Jiahua Z., ChemComm., 2011,47, 4753.
- [2] Zhang X. and Gong M., Mater. Lett., 2011, 65, 1756.
- [3] Lu W., Jia Y. C., Lv W. Z., Zhao Q. and You H. P., New J. Chem., 2013, 37, 3701.

Vplyv prídavku Eu a Ce na fotoluminiscenčné vlastnosti MgSiN₂

Influence of Eu and Ce additives on the luminescent properties of MgSiN₂

Z. Lenčoš¹, A. Czímerová¹, M. Vyležíková^{1,2}, P. Šajgalík¹, Z. Jonšta²

¹ *Institute of Inorganic Chemistry, Slovak Academy of Sciences, Dúbravská cesta 9, 84536 Bratislava, Slovakia*

² *Faculty of Metallurgy and Materials Engineering, VŠB - Technical University of Ostrava, 17. listopadu, 708 33 Ostrava, Czech Republic*

ABSTRAKT

Europium and cerium doped MgSiN₂ phosphors were synthesized by nitridation of Mg₂Si/Si/Si₃N₄/Eu₂O₃ and Mg₂Si/Si/Si₃N₄/CeO₂ mixtures at 1390°C and additional annealing at 1550°C for 1 and 4 hours. The MgSiN₂ phosphors doped with Eu and annealed for 1 h showed a broad emission in the range of 450-550 nm (blue – green light). Although the intensity of emission slightly increased with increasing Eu content (2, 4 and 6 mol.%), the total intensity of emitted light was rather weak. The intensity of emitted light remarkably increased after annealing the MgSiN₂:Eu phosphors at 1550°C for 4 hours. Moreover, a strong red shift was observed for these phosphors with a maximum photoluminescent intensity at 708 nm for (MgSiN₂ + 6 mol.% Eu) phosphor. Contrary to the MgSiN₂:Eu phosphors, the cerium doped MgSiN₂ phosphors showed two discrete emission peaks with a maxima at 430 nm and 565 nm.

Keywords: magnesium silicon nitride, nitridation, luminescence, phosphors

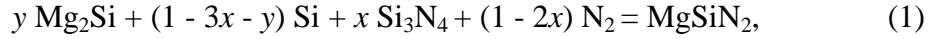
INTRODUCTION

Magnesium silicon nitride (MgSiN₂) was intensively studied as a promising light weight engineering ceramic material owing to its high hardness (20 GPa), reasonable strength and fracture toughness [1-3]. MgSiN₂ exhibits also high electrical resistance and good thermal conductivity, therefore, it was studied also as a candidate material for electronic substrates [4]. Moreover, in the last two decades the ternary nitrides and oxynitrides gained and increased attention as a host lattices for phosphors due to their high chemical and thermal stability, rigid crystal structure, availability of suitable crystal sites for activators, which enable their doping with lanthanide ions to provide luminescence [5]. MgSiN₂ crystallizes in an orthorhombic structure with a space group *Pna2₁*, which is formed as a result of intrinsic deformation of wurtzite structure. In the MgSiN₂ structure, normal to the *c*-axis there are a layers of tetrahedrons of [MgN₄]-[MgN₄] and [SiN₄]-[SiN₄]. The distance between tetrahedrons (2.5 Å) allows the introduction of lanthanide ions into MgSiN₂ lattice and the substitution of Mg ions under certain conditions [6]. Therefore, the following MgSiN₂-based phosphors have been already studied: MgSiN₂:Eu²⁺ [7], MgSiN₂:Sm³⁺ and MgSiN₂:Yb³⁺ [8], Mg_{1-x}Mn_xSiN₂ [9], Mg_{1-x}Zn_xSiN₂:Tb [10], MgSiN₂:Ce³⁺ and mixed MgSiN₂:Ce³⁺Mn²⁺ [11] phosphors. Duan et al. showed that these phosphors can be used for the construction of white-LEDs [12]. Therefore, a low cost and environmentally friendly production of MgSiN₂ would be very useful. All the above mentioned MgSiN₂-based phosphors were prepared by traditional solid-state reaction including Mg₃N₂ or metallic Mg, but both are very sensitive to moisture, thus, leading to difficulties during processing of powder mixtures and to low yields. In this work we have used the Mg₂Si/Si/Si₃N₄ starting mixture for the preparation of MgSiN₂ host lattice. This is a more efficient, high-yield route for the preparation of MgSiN₂ based phosphors. In the frame of this work we have studied the influence of Eu and Ce dopants

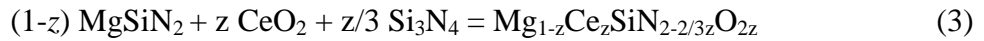
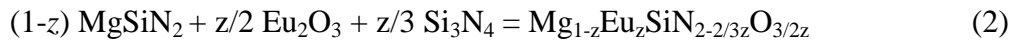
addition, and the annealing time on the photoluminescent properties of MgSiN₂-based phosphors.

EXPERIMENTAL

The starting powder composition for the preparation of MgSiN₂ was determined according to the following equation:



where $x = 0.06$ and $y = 0.50$, respectively [13]. The following starting powders were used: Mg₂Si (99%, $d_{\text{max}} \leq 150 \mu\text{m}$, Kojundo Chem. Lab., Japan), Si (grade 2C, SicoMill, Vesta Ceramics, Sweden) and α -Si₃N₄ (grade SN-E10, Ube Industries, Ltd., Japan). The lanthanide dopants were added in a form of Eu₂O₃ and CeO₂ (both powders 99.99%, Treibacher Industrie AG, Austria) and their content was calculated according to the following hypothetical reactions:



The lanthanide dopants were added to the powder mixtures from the beginning of synthesis, i.e. the mixtures were composed of Mg₂Si/Si/Si₃N₄/Eu₂O₃ or Mg₂Si/Si/Si₃N₄/CeO₂ and their composition was determined by the combination of Eqs. (1) and (2) for Eu or Eqs. (1) and (3) for Ce, respectively. The content of europium was $z = 0.02$; 0.04 and 0.06, while for cerium only one concentration $z = 0.04$ was tested.

The powders were mixed in a dry state using an agate mortar and pressed into pellets with a diameter of 10 mm. The pellets were placed into BN crucible on thin BN powder layer and nitrided in a graphite resistance furnace (Centorr, USA) under the conditions described elsewhere [13]. After nitridation the samples were additionally annealed in a gas pressure furnace (FCT, Germany) at 1550°C for 1 and 4 hours under a nitrogen pressure of 1.5 MPa. The overpressure of nitrogen was necessary to avoid the decomposition of MgSiN₂ [14]. The phase composition of nitrided and annealed samples was determined by XRD analysis (D8-Discover, Bruker, CuK α radiation). The photoluminescence spectra of the powders were measured using a fluorescence spectrophotometer (Fluorolog 3-11, ISA/Jobin Yvon-SPEX, France).

RESULTS

All the MgSiN₂ samples doped with europium had a yellow colour after annealing at 1550°C. The brightest yellowish colour had the powder containing 1 mol.% Eu. On the other hand, sample MgSiN₂:Ce³⁺ had a grey-yellow colour. The particle size of synthesized MgSiN₂:Eu phosphor was in the range 1-3 μm . The XRD phase analysis of MgSiN₂:Eu phosphors showed that the major phase is MgSiN₂ and in samples with 6 mol.% Eu also a minor diffractions of Eu₂Si₅N₈ were detected.

The measured photoluminescence spectra showed that all MgSiN₂:Eu phosphors annealed at 1550°C for 1 h exhibited a blue and green emission band in the wavelength range of 450-550 nm (Fig. 1). A remarkable red shift was observed in the emission spectra, when the samples were annealed at 1550°C for 4 hrs in 1 MPa nitrogen atmosphere [Fig. 2]. Most probably we have succeeded to reduce Eu³⁺ to Eu²⁺ in nitrogen atmosphere, as it was reported by de Graaf et al. [15] according the following equation:



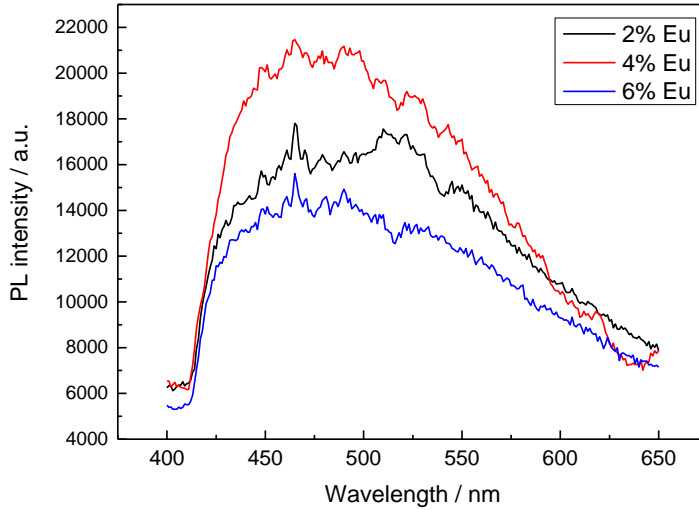


Fig. 1: Emission spectra of MgSiN₂:Eu phosphors ($\lambda_{\text{ex}} = 420 \text{ nm}$) annealed at 1550 °C for 1 h.

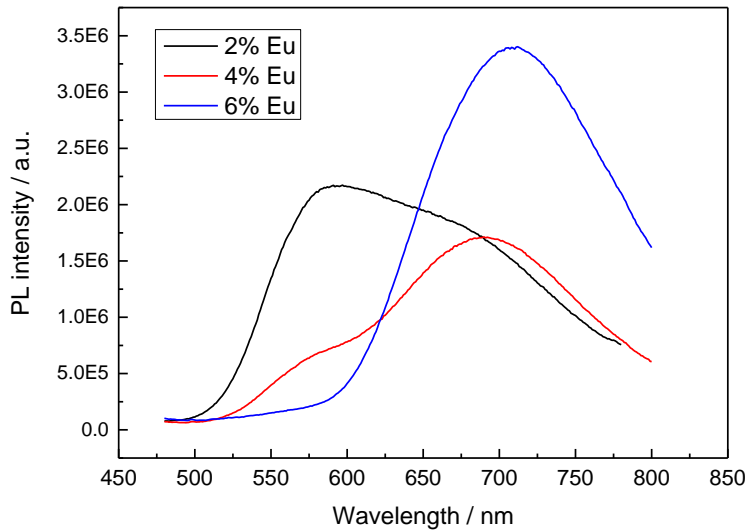


Fig. 2: Emission spectra of MgSiN₂:Eu phosphors ($\lambda_{\text{ex}} = 420 \text{ nm}$) annealed at 1550 °C for 4 hrs.

The maximum photoluminescent intensity at 708 nm was observed for MgSiN₂ sample with 6 mol.% Eu using an excitation wavelength of 420 nm. The other MgSiN₂:Eu samples with lower Eu content had a lower photoluminescent intensity, but all the phosphors had a broad emission band in the red light region.

MgSiN₂ samples doped with 4 mol.% Ce had two emission maxima located at 430 nm and 565 nm (Fig. 3), i.e. in the blue and green-yellowish region.

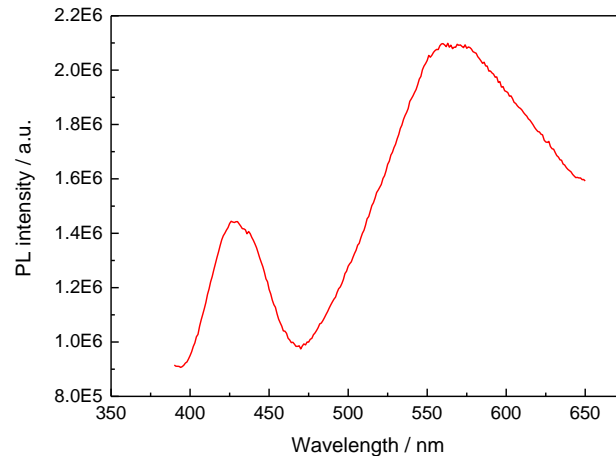


Fig. 3: Emission spectrum of MgSiN₂:4%Ce phosphor annealed at 1550 °C for 4 hrs.

CONCLUSION

Europium and cerium doped MgSiN₂ phosphor was synthesized from Mg₂Si/Si/Si₃N₄/Eu₂O₃ and Mg₂Si/Si/Si₃N₄/CeO₂ mixture by direct nitridation at 1390°C and additional annealing at 1550°C for 1 h and 4 h. The phosphors doped with europium and annealed for 1 h shows emission in the blue and green region. MgSiN₂:Eu phosphors annealed for 4 hrs show broad emission band from 550 nm to 800 nm with a maximum at 708 nm. MgSiN₂ phosphor doped with cerium shows emission in the green-yellowish light region with the maximum intensity at 565 nm. The XRD analysis of all phosphors showed that the major phase is MgSiN₂. In sample with 6 mol.% Eu also a weak diffractions of Eu₂Si₅N₈ were detected.

ACKNOWLEDGMENT

This work was supported by the Slovak grant agencies APVV-14-0385 and VEGA-2/0112/14 and the financial support through ERANET (GRACE). This publication is the result of the project implementation: „High-current plasma generator based on composite materials“, ITMS code 26240220054, supported by the Research & Development Operational Programme funded by the ERDF.

REFERENCES

- [1] Groen, W.A., Kraan, M.J., de With, G., Preparation, microstructure and properties of MgSiN₂ ceramics. *J. Eur. Ceram. Soc.*, **12** (1993) 413-420.
- [2] Hintzen, H.T., Swaanen, P., Metselaar, R., Groen, W.A., Kraan, M.J., Hot-pressing of MgSiN₂ ceramics. *J. Mater. Sci. Lett.*, **13** (1994) 1314-1316.
- [3] Davies, I.J., Uchida, H., Aizawa, M., Itatani, K., Physical and mechanical properties of hot-pressed magnesium silicon nitride compacts with yttrium oxide addition. *Inorg. Mater. Jpn.*, **6** (1999) 40-48.
- [4] Tanaka, S., Itatani, K., Uchida, H., Aizawa M., Davies, I.I., Suemasu, H., Nozue, A., Okada I., The effect of rare-earth oxide addition on the hot-pressing of magnesium silicon nitride. *J. Eur. Ceram. Soc.*, **22** (2002) 777-783.
- [5] Xie, R.-J., Hirosaki, N., Silicon-based oxynitride and nitride phosphors for white LEDs – A review. *Sci. Technol. Adv. Mater.*, **8** (2007) 588-600.

- [6] Bondar, V., Axelrud, L., Davydov, V., Felner, T., Synthesis, structure and luminescence of $A^2B^4C^5$ nitrides. *Mat. Res. Soc. Symp. Proc.*, **639** (2001) G11.36.1-6.
- [7] Gaido, G.K., Dubrovskii, G.P., Zykov, A.M., Photoluminescence of $MgSiN_2$ activated by europium. *Izv. Akad. Nauk SSSR, Neorg. Mater.*, **10** [3], (1974) 564-566.
- [8] Dubrovskii, G.P., Zykov, A.M., Chernovets, B.V., Luminescence of rare-earth activated $MgSiN_2$. *Izv. Akad. Nauk SSSR, Neorg. Mater.*, **17** [8], (1981) 1421-1425.
- [9] Duan, C.J., Delsing, A.C.A., Hintzen, H.T., Red emission from Mn^{2+} on a tetrahedral site $MgSiN_2$. *J. Lumin.*, **129** (2009) 645-649.
- [10] Lim, S., Lee, S.S., Chang, G.K., Photoluminescence characterization of $Mg_{1-x}Zn_xSiN_2:Tb$ for thin film electroluminescent devices application. *Inorganic and Organic Electroluminescence*, Eds. R.H. Mauch and H.-E. Gumlich, Wissenschaft und Technik Verlag, Berlin, (1996) p. 363-366.
- [11] Kulshreshtha, Ch., Kwak, J.H., Park, Y.J., Sohn, K.S., Photoluminescent and decay behaviors of Mn^{2+} and Ce^{3+} coactivated $MgSiN_2$ phosphors for use in light-emitting-diode applications. *Opt. Lett.*, **34** [6], (2009) 794-796.
- [12] Duan, C.J., Rösler, S., Starick, D., H.T. Hintzen, Rösler, S., Ce^{3+} , Eu^{2+} and Mn^{2+} activated alkaline earth silicon nitride phosphors and white-light emitting LED. European patent WO2009003988.
- [13] Lenčėš Z., Hirao, K., Yamauchi, Y., Kanzaki, S., Reaction synthesis of magnesium silicon nitride powder. *J. Am. Ceram. Soc.*, **86** [7], (2003) 1088-93.
- [14] Lenčėš, Z., Pentráková, L., Hrabalová, M., Hirao, K., Šajgalík, P., Decomposition of $MgSiN_2$ in nitrogen atmosphere. *J. Eur. Ceram. Soc.*, **31** (2011) 1473-80.
- [15] D. de Graaf, H.T. Hintzen, S. Hampshire, G. de With, "Long Wavelength Eu^{2+} Emission in Eu-doped Y-Si-Al-O-N Glasses," *J. Eur. Ceram. Soc.*, **23**, 1093-97 (2003).

INDEX AUTOROV

B			
Bača E.	18, 89	Barroso G.	23
Balážová P.	83, 86	Bystrický R.	32
<hr/>			
C			
Chovanec J.	64	Čaplovičová M.	47, 76
Cigán A.	57	Černá A.	64
Czímerová A.	98	Čierniková M.	83, 86
<hr/>			
D			
Dvurečenskij A.	57		
<hr/>			
E			
Emmerich K.	76	Exnar P.	83, 86
<hr/>			
F			
Fides M.	32		
<hr/>			
G			
Galusek D.	23, 27, 38, 43, 52, 57, 64, 72, 93	Gregor M.	69
Galusková D.	72		
<hr/>			
H			
Hajdúchová Z.	89	Hanzel O.	4
Haladejová K.	27, 52, 64, 93	Hronský V.	76
<hr/>			
J			
Janek M.	76	Jonšta Z.	98
<hr/>			
K			
Kitzmantel M.	18	Kraxner J.	57, 64
Klement R.	27, 38, 52, 93	Kúš P.	47
Kováčová Z.	18		
<hr/>			
L			
Lencěš Z.	98		
<hr/>			
M			
Maca K.	10	Mikula M.	47
Majerová M.	57	Mikušínc S.	72
Maňka J.	57	Motz G.	23
<hr/>			
N			
Naftaly M.	76	Nowicka A.	72
Neubauer E.	18		
<hr/>			
P			
Pagáčová J.	83, 86	Plecenik T.	69
Papučová I.	83, 86	Plesch G.	69
Parchovianský M.	23, 57	Plško A.	83, 86
Petriková I.	23, 64	Prajzler V.	10
Plašienka D.	47	Prnová A.	27, 43, 52, 57, 93
Plecenik A.	69		
<hr/>			
R			
Roch T.	47		

S			
Salamon D.	10	Šajgalík P.	4, 32, 98
Sedláček J.	4, 32	Škrátek M.	57
Sedlák R.	4	Švančárek P.	23, 38

T			
Tofail S.A.M.	69	Truchlý M.	47, 69

V			
Veteška P.	43	Vyležiková M.	98

Z			
Zahoran M.	69	Zacher T.	76

Book of extended abstracts

Workshop „PROCESSING AND PROPERTIES OF ADVANCED CERAMICS”

23.11. – 25.11. 2016, Košická Belá-Ružín, Slovensko

Published by: Institute of Inorganic Chemistry, SAS
Dúbravská cesta 9
845 36 Bratislava
Slovak Republic

Novembre 2016

Book reviewers: prof. Ing. Dušan Galusek, DrSc.
prof. RNDr. Karel Maca, Dr.
doc. Ing. Zoltán Lenčoš, PhD.
doc. Ing. Miroslav Hnatko, PhD.
Ing. Jaroslav Sedláček, PhD.
Ing. Marián Mikula, PhD
Ing. Alexandra Kovalčíkova, PhD.

Edited by: Jana Valúchová

ISBN 978-80-971648-5-0

ISBN 978-80-971648-5-0